Volumetric Measurements of the Transitional Backward Facing Step Flow

Von der Fakultät für Maschinenbau, Verfahrens- und Energietechnik

der Technischen Universität Bergakademie Freiberg

genehmigte

DISSERTATION

zur Erlangung des akademischen Grades

Doktor Ingenieur

(Dr.-Ing.)

vorgelegt

von Dipl.-Ing. Jens Kitzhofer

geboren am 22.03.1981 in Moers

Gutachter: Prof. Dr.-Ing. habil. Christoph Brücker, Freiberg

Prof. Dr.-Ing. habil. Hans-Gerd Maas, Dresden

Tag der Verleihung: 8.8.2011

. . .für mein großes Glück:

Mats, Jana & Cor *

Versicherung

Hiermit versichere ich, dass ich die vorliegende Arbeit ohne unzulässige Hilfe Dritter und ohne Benutzung anderer als der angegebenen Hilfsmittel angefertigt habe; die aus fremden Quellen direkt oder indirekt übernommenen Gedanken sind als solche kenntlich gemacht. Bei der Auswahl und Auswertung des Materials sowie bei der Herstellung des Manuskripts habe ich Unterstützung von folgenden Personen erhalten:

Prof. Dr.- Ing. habil. Christoph Brücker

Weitere Personen waren an der Abfassung der vorliegenden Arbeit nicht beteiligt. Die Hilfe eines Promotionsberaters habe ich nicht in Anspruch genommen. Weitere Personen haben von mir keine geldwerten Leistungen für Arbeiten erhalten, die nicht als solche kenntlich gemacht worden sind.

Die Arbeit wurde bisher weder im Inland noch im Ausland in gleicher oder ähnlicher Form einer anderen Prüfungsbehörde vorgelegt.

Contents

Nomenclature

A	filled profile [mm²], intern transformation matrix, universal boundary layer constant, amplitude
AR	aspect ratio (B/h)=57
B	step span, solution matrix 3x3 (3D point)
BFSF	backward facing step flow
CC	cross correlation
CCD	charge coupled device
Cr_{shear}	shear layer criterion
D	extern transformation matrix
DCT-PLS	discrete cosines transform - penalized least squares
DNS	direct numerical simulation
E	solution matrix 4x3 (3D point)
ER	expansion ratio (h_2/h_1=1.25)
F	fundamental matrix
FFT	fast fourier transformation
FR	flow reattachment
FS	flow separation
J	jacobian
L_E	entry length
L_y	image height
LS	light sheet
LSM	least squares matching
M	magnification
NN	nearest neighbour
P'	perspective transformation matrix
P	projection matrix
PDF	probability density function
PIV	particle image velocimetry
POD	proper orthogonal decomposition
PTV	particle tracking velocimetry

II

Q	solution matrix (calibration P), vortex detection criterion
R	rotational matrix
Re_h	Reynolds number based on step height
ROI	region of interest
P,Q,R	invariants
S	rate of strain tensor
S'	deviatoric rate of strain
Tu_x	turbulence intensity in streamwise direction (= $(u'^2)^{1/2}$)
U	velocity $(u,v,w)^T$
U	instantaneous velocity $(u,v,w)^T$ [mm/s] ,wetted circumference [mm]
U*	normalized velocity: $U^*=U/U_\infty$
U_{bulk}	free-stream/bulk velocity
W	object point
X	image coordinates [pix]
X_C	camera coordinates [mm]
X_S	sensor coordinates [mm]
X_W	object coordinates [mm]

c	solution vector 1x3 (3D point), camera center
d_{max}	particle displacement
e	difficulty in tracking single particles
f	focal length
fps	frames per second
h	step height [mm]
h_1	channel height upstream of expansion
h_2	channel height downstream of expansion
k	scaling factor [pix/mm]
$l_{d,eq}$	equivalent diameter: 4A/U [mm]
n	refractive index
ppp	particles per pixel
s	median particle distance
t	translational vector, normalized time $t^*=t \cdot U_\infty/h$
t_L	temporal length of a trajectory
u^+	sublayer scaled velocity $u^+ =u/u_\tau$ [-]

u_τ	wall shear velocity [mm/s]
x_{r1}	primary point of reattachment
x_{r2}	secondary point of reattachment
y^+	sublayer scaled distance from the wall $y^+ = y \cdot u_\tau / \upsilon$ [-]
Φ	quality criteria
Ω	rate of rotation
α	inclination angle of vortex roll up
δ	total shear layer thickness ($\boldsymbol{\delta = \delta_+ + \delta_-}$) [mm]
$\boldsymbol{\delta_+}$	upper shear layer thickness [mm]
$\boldsymbol{\delta_-}$	lower shear layer thickness [mm]
$\partial\delta/\partial x$	growth rate
Δt	separation time
θ	momentum thickness $\theta^* = \theta/h$
κ	universal boundary layer constant
Δ	vortex detection criterion
λ	eigenvalue, wave length
λ_2	vortex detection criterion
ρ_P	density of seeding particles [kg/m³]
υ	kinematic viscosity [m²/s]
ω	vorticity

IV

List of Figures

Tables

1 Introduction

1.1 Overview

Flow Separation (FS) and Flow Reattachment (FR) have been in focus of investigation for more than hundred years since the famous studies of Ludwig Prandtl at the beginning of the 19th century in Göttingen. Understanding the way flow separates and reattaches on a surface is critical in engineering applications. Today, one of the major tasks is designing in a drag reducing manner for efficiently reducing fuel consumption in transportation. Here, drag is highly influenced by separation and reattachment of the flow. It is obvious that some kind of boundary layer separation occurs on vehicles, airplanes or in combustors. The most hazardous consequence of FS is stall in aerodynamics. The boundary layer separates on the surface and the airfoil looses lift.

First studies about separated flows are dated back to 1868 (Helmholtz) and 1869 (Kirchhoff) in case of bluff bodies. From theoretical, experimental and numerical point of view much effort has been made in understanding the physical background of the flow phenomena. No matter if laminar FS or turbulent FS occurs, the FR is characterized by turbulent flow behaviour. The basic for the analysis of such highly fluctuating flows is the need "to separate the random processes from the non-random processes" as stated by Dryden (1948) [29]. This statement implies the existence of ordered structures (non-random processes) in turbulence. Via qualitative flow visualization some of the "orderly elements" began "to be recognized and described" as discussed by Roshko (1976) [111]. Nevertheless, three-dimensional coherent structures were hidden for quantitative measurements due to insufficient measurement techniques. Here, recent developments in volumetric measurement techniques allow the analysis of the "orderly elements". In fact, recent results concerning three-dimensional coherent structures in a turbulent boundary layer show the importance for investigation, because these structures seem to form the skeleton of turbulent flow [126].

The investigation of FS and FR is connected with some difficulties since both are linked together. Figure 1.1 on top shows a schematic representation of FS-FR on an airfoil. The boundary layer separates at x_s, develops into a shear layer and reattaches at x_r. In between, the separated boundary layer rolls up into vortices with the main axis of rotation in spanwise direction (Kelvin Helmholtz instability). The size of the rollers is amplified in

downstream direction. Underneath the shear layer a separation bubble (recirculation region) is formed. The recirculation region is characterized by a low speed, but highly fluctuating flow state. Furthermore, these fluctuations result in fluctuations of x_s and x_r. This is a complex feedback system, as the fluctuation of the separation bubble results in a variable point of reattachment.

A more controlled situation is in the Backward Facing Step Flow (BFSF) as shown in figure 1.1 on the bottom. Herein, the point of separation is spatially fixed. The boundary layer separates at the step edge due to the sudden geometrical expansion resulting in a positive pressure gradient in flow direction. Due to the forced separation, the flow configuration is also called forced shear layer. The separated shear layer is characterized by high, positive velocities on the free stream side and low positive or negative velocities on the other side. Behind the separation edge, the shear layer rolls up into discrete vortices due to Kelvin-Helmholtz instabilities. The shear layer further develops in streamwise direction including complex vortex interactions such as vortex pairing and vortex merging. The separated boundary layer finally reattaches at a certain distance downstream of the step on the bottom wall at x_r and forms a recirculation region. The point of reattachment is highly unsteady as the flow in vicinity of reattachment is characterized by turbulent shear layer impinging.
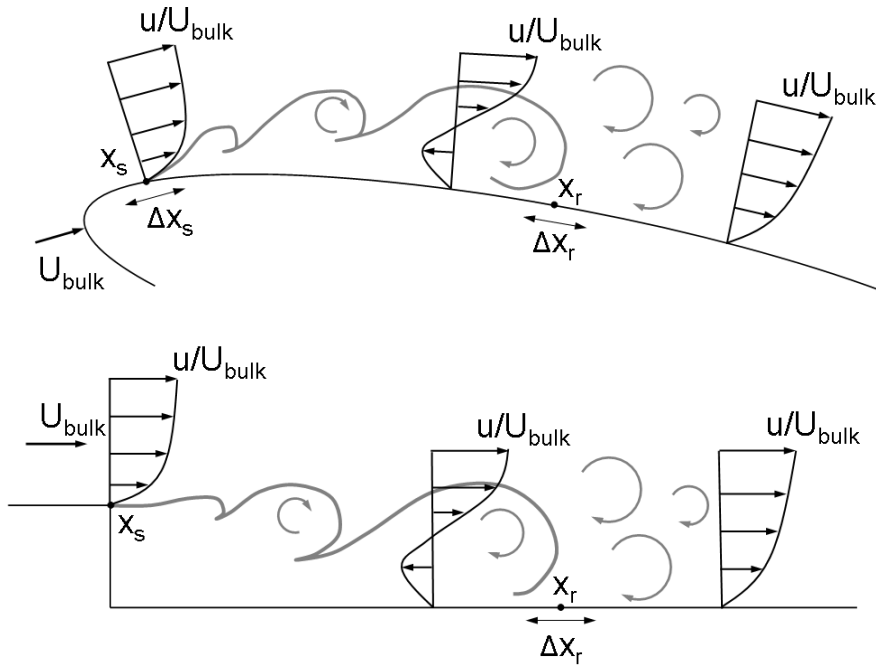
Fig 1.1 Sketch of Flow Separation (FS) and Flow Reattachment (FR) on an airfoil (**top**) and at a Backward Facing Step Flow (**bottom**)

Although FS and FR have been the subject of many investigations, both are not fully understood at high Reynolds-numbers, where transitional or turbulent effects start to dominate. Due to the spatially fixed point of separation, the BFSF is a frequently applied flow configuration for the analysis of reattachment. The motivation is in a deeper understanding of fundamental events concerning this type of flow for possibilities of active control. Especially, the influence of three-dimensional coherent flow structures is not fully disclosed.

Former quantitative studies on the BFSF can be divided into the use of pointwise measurement techniques such as hot-wire anemometer or Laser Doppler anemometer and into the use of planar measurement techniques like Particle Image Velocimetry (PIV). The pointwise techniques were primarily applied for statistical analysis delivering deep inside into overall flow behaviour like characteristic regions, flow reattachment or mean velocity profiles. Planar measurement techniques like PIV supported the evaluation of coherent flow structures. Limits are reached with these classical techniques beyond a Reynolds number, where three-dimensionality occurs. Thus, three-dimensional datasets or investigations at high Reynolds numbers are rare in literature, limited to three-dimensional Direct Numerical Simulations (DNS) up to low transitional Re-numbers [119]. Volumetric measurements on the BFSF were performed by Kasagi and Matsunaga (1995) [61] via 3D Particle Tracking Velocimetry and more recently by Schröder et al. (2011) [127] via Tomographic PIV. The authors show the necessity for consideration of three-dimensionality in the analysis of the BFSF as three-dimensional vortical structures are omni-present in the BFSF.

Due to the availability of newest, high quality hardware at rather low cost, a rush is recognized in further development of existing techniques and development of new techniques for the measurement of volumetric velocity fields. Differences of the techniques can be found in applied hardware and software, in temporal and spatial resolution, in complexity, in optical registration and in flow description (Lagrangian or Eulerian). However, all up to date techniques for measuring velocities use tracer particles for marking the flow. The particles are illuminated by a light source and recorded on a sensor or an arrangement of sensors. By proper algorithmic reconstruction techniques the velocity field is calculated. Once the velocity field is generated, it is described by velocity vectors at random or structured positions in a defined volume.

The availability of all three velocity components in a time resolved manner gives rise to the analysis of the velocity gradient tensor. The tensor consists of the spatial derivatives of

the velocity field and has become the most famous mathematical description for the extraction of coherent flow structures.

For that purpose, this thesis applies a state of the art volumetric measurement technique, time resolved 3D Scanning Particle Tracking Velocimetry, for the investigation of the natural BFSF in the transitional to turbulent regime. Here, 'natural' means that the flow structure is generated by self-organization contrary to the 'manipulated' BFSF, where the flow dynamics is somehow forced into a regular pattern by certain excitation.
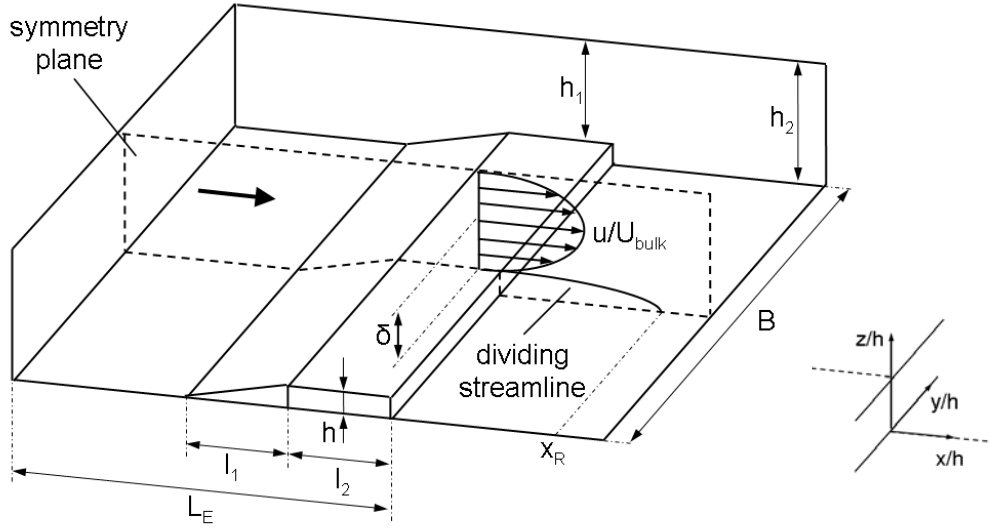
Fig 1.2 Definition of geometry, major parameters and coordinate system: B = 570 mm, L_E = 1600 mm, U_{bulk} = 0.52 m/s, $l_{d,eq}$ = 92 mm, l_1=60 mm, l_2=60 mm, h_1 = 40 mm, h_2 = 50 mm, h = 10 mm, δ = momentum thickness, x_R = reattachment length

The BFSF is studied herein in a rectangular (50mm x 570mm) closed circuit water channel (υ=10^{-6} m²/s) with canonical channel geometry as sketched in figure 1.2 and the flow facility is shown in figure 1.3. The distance between the duct entrance and the volume of interest, called entry length L_E is about 17 time the equivalent diameter $l_{d,eq}$. The channel flow is driven by gravity and the mean flow is regulated via the hydrostatic head. All experiments were carried out for a defined height of the hydrostatic head generating a bulk velocity upstream of the step of U_∞=0.47m/s. The backward facing step is positioned on the bottom of the channel with respect to Beaudoin et al. (2004) [11]. The step height h is chosen to 10mm, resulting in a Reynolds-number Re_h = 4440 based on the step height. The length of the ramp as well as the length of the plateau is 60 mm. The aspect ratio AR (B/h) results in 57 and the expansion ratio ER (h_2/h_1) results in 1.25.

Fig 1.3 Experimental flow facility

All calculations regarding development and testing are performed via Matlab R2008b on an Intel Core2 Quad CPU9450 @ 2.66 GHz, 3 GB RAM. The final analysis of in total 80 GB raw image data is performed on a machine with 2 Six-Core AMD Opteron (tm) processors 2435 @ 2.6 GHz, 32 GB RAM.

1.2 Aim of the Thesis

The thesis aims to extend the knowledge of separated and reattaching shear layers in the transitional/turbulent regime. The final goal is a better physical understanding of complex dynamical interactions of coherent flow structures. Furthermore, the thesis tries to fill up the lack of missing three-dimensional and time resolved data regarding the BFSF. For that purpose, the thesis is structured into three partial goals.

Goal one is the development and implementation of a three-dimensional measurement technique (3D Scanning Particle Tracking Velocimetry) operating at high spatial and temporal resolution. The technique is developed and adapted in a manner to be optimally suited for the analysis of the present, natural BFSF in the transitional regime.

Goal two is the analysis of the time resolved and three-dimensional datasets of the BFSF. Here, the thesis focuses on the extraction of shape and influence of three-dimensional coherent structures like vortices or shear layers.

Goal three is the fluid mechanical interpretation of the achieved results. For that purpose, the present test case is categorized with respect to the already existing large amount of pointwise, planar and joint measurements and numerical simulations available in literature. Proposals for mechanisms are presented trying to explain the observed unsteady characteristics of the BFSF.

As shown in figure 1.1 on the bottom, unsteady phenomena in the BFSF take place in the vicinity of the step corner. Thus, the region of interest (ROI) is positioned about the symmetry plane immediately downstream of the step. The ROI is sized to about 90 x 90 x 15 mm³ allowing the observation of the unsteady flow phenomena. The region contains the shear layer and the turbulent reattachment.

All characteristic events disclosed herein will be described in context with earlier findings published in literature, via qualitative flow visualization and via results obtained by quantitative visualization (3D Scanning PTV). Parts of the thesis are funded by the German Research Foundation (DFG) in the SPP 1147: Bildgebende Messverfahren (1494/11-1), which are greatly acknowledged here, and supported by Dantec Dynamics A/S.

1.3 Structure of the Thesis

The thesis is organized in two main parts. Part one describes the applied measurement techniques (chapter 2). Part two focuses on the categorization (chapter 3) and analysis (chapter 4) of the BFSF.

Chapter 2 describes the applied measurement techniques. Beside the volumetric technique, planar time resolved PIV is used in multiple planes for the characterization of the inlet flow conditions and for the validation of the results obtained by the volumetric technique. The boundary conditions of the measurement and the estimated accuracy is pointed out. The volumetric measurement technique is discussed in detail in the second part. Available volumetric measurement techniques like tomographic PIV, digital holographic PIV or defocusing PIV to study three-dimensional unsteady flow in complex flow fields are presented. Advantages and drawbacks will be pointed out and discussed. The third part of the chapter explains the measurement technique of choice, 3D Scanning Particle Tracking Velocimetry. The principle of the technique is pointed out in detail. Further developments for increasing the capability, especially the temporal and spatial resolution, are discussed. The necessary hardware devices will be presented and the integration of the hardware to the experimental set-up is explained. Parts of the chapter have already been published in archived journal papers [64][65][66].

Chapter 3 focuses on the categorization of the BFSF in terms of existing literature. For that purpose, characteristic geometrical properties are pointed out. Mean kinematic properties are calculated via the results obtained by the PIV measurements. The obtained properties are compared in a detailed literature review including qualitative flow visualizations,

quantitative pointwise measurements and planar optical or pressure based measurements. Review of CFD results focuses on recently published papers. Furthermore, unsteady phenomena concerning the BFSF are presented.

Chapter 4 provides detailed interpretation of the measured velocity field. The velocity field is separated into characteristic regions. Unsteady events inside the single regions are detected and discussed. The focus is in the extraction of large scale coherent structures influencing the reattachment position.

Chapter 5 summarizes the obtained results and draws a conclusion. The outlook provides recommendations for future research regarding the backward facing step flow and volumetric measurement techniques.

2 Measurement Techniques

The fundamental theorem of Helmholtz says that every infinitesimal motion of a fluid element can be decomposed into translation, rotation and deformation. In the last decades several investigations have been performed to experimentally describe these fluid motions. The importance of measurement is stated by Kähler (2004) [60]. The mathematical description of fluid motion assumes pointwise description. This is valid by detailed knowledge of local properties of all neighbouring fluid elements in a three-dimensional space. Thus, the kinematic state of a fluid element is described by twelve parameters: three translational velocities and nine spatial derivatives of the velocity field in that point.

Standard pointwise measurement techniques like Hot Wire anemometry are limited to the measurement of one velocity component. More sophisticated sensor configurations allow measuring all three velocity components at approximately a single measurement location. Nevertheless, evaluation of spatial derivatives or simultaneous measurements of multiple points in a sufficient spatial resolution is not possible. In the last decades, PIV and Stereoscopic PIV have become standard techniques for measuring two or three velocity components in a planar field providing the 3 translational and 6 spatial derivatives in a certain plane. Recently developed fully volumetric measurement techniques with (under distinct restrictions) sufficient temporal and spatial resolution are able to measure the whole set of fluid motion. Thus, the new rush in volumetric measurement techniques allows a deeper insight into the three-dimensional nature of unsteady flow phenomena.

For that purpose, this chapter describes the applied techniques for measuring the velocity field of the BFSF shown in figure 1.2. The focus of the first part of the chapter is in planar measurement techniques, namely two-dimensional, two-component Particle Image Velocimetry (2D2C PIV) and Laser Induced Fluorescence (LIF). The techniques are nowadays standard [108]. Thus, the implementation and an estimation of the achieved quality will be briefly discussed. The second part contains a detailed literature review of existing volumetric measurement techniques based on particle imaging for measuring three-dimensional (3D) and three-component (3C) velocity vector fields of a fluid flow. Principles and hard- and software requirements are described for each technique highlighting the differences in hardware and software, temporal and spatial resolution, complexity, optical description and flow description. Techniques will be preferably described, whose results are directly 3D3C, (without applying e.g. continuity equation

[110] or out of plane correlations [106]) and are based on illuminated particle images. The chapter finishes with a detailed description of the measurement technique of choice, 3D Scanning Particle Tracking Velocimetry.

2.1 Planar Measurement Techniques

LIF is used herein for qualitative flow visualization and PIV is used for quantitative description. Flow visualization via LIF provides a first impression of the structure and dynamic of coherent flow structures. This is a kind of visual extraction of dominant events being further analyzed in the quantitative measurements via PIV and 3D Scanning Particle Tracking Velocimetry.

Figure 2.1 shows the investigated planes. PIV is performed in each of the streamwise symmetry planes (P1-P4: overlap 20 mm; P6) and in a plane parallel to the bottom wall at $y/h = 0.1$ (P5). The LIF measurements were exclusively performed in P3. A digital high speed camera (Photron APX RS, 1024 x 1024 Pixel², 3000 fps) is used for both types of recording. The camera is adjusted perpendicular to the light sheet and variable in streamwise direction. For the measurements of the flow filed in P1-P5, the camera is equipped with a telecentric lens system resulting in a magnification of 0.2, which means an object format of 90 x 90 mm² in physical space. The physical size of the single recorded images is then defined by the image width and the channels height resulting in 90 x 50 mm² for P1-P4 and 90 x 90 mm² for P5. P6 is recorded with a long distance microscope (LDM) to achieve a high spatial resolution in the region near the wall for the calculation of accurate inlet flow conditions. The size in physical space is 3 x 3 mm².
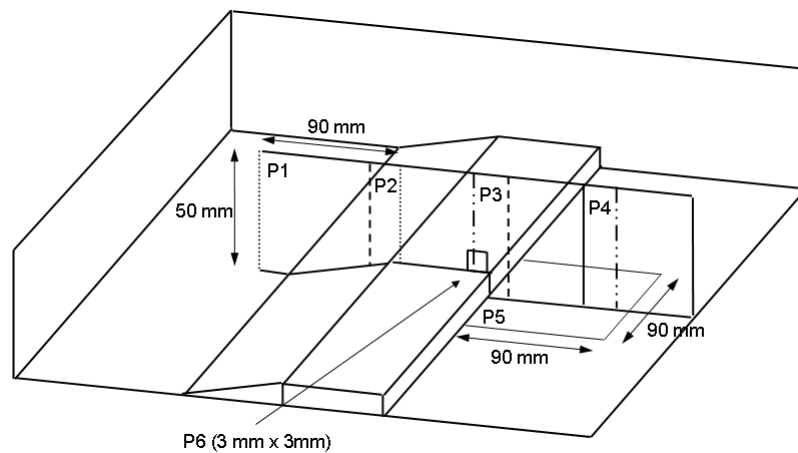
Fig 2.1 Definition of symmetry planes recorded via PIV and LIF: plane P1-P6 PIV, plane P3 LIF

2.1.1 Laser Induced Fluorescence

In principal, it is possible to analyze LIF measurements in a qualitative and in a quantitative manner. Herein, the technique will be exclusively used for time resolved qualitative flow visualization as shown in figure 2.2 in an instantaneous snapshot of the flow region in P3. For that purpose, fluid with fluorescent properties (Rhodamin B) is injected upstream of the step. The fluid is excited with a high speed laser (Coherent Innova, 532 nm) and the emitted light is recorded by the high speed cameras at 1000 fps.
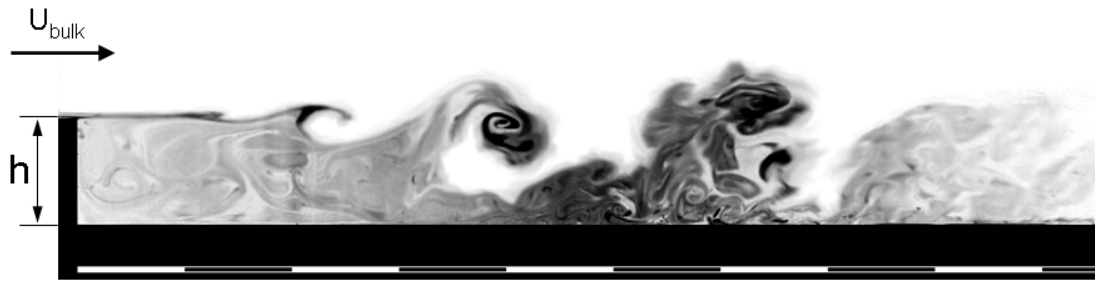
Fig 2.2 Snapshot of the BFSF visualized via Laser Induced Fluorescence. The size of recording region is approximately W x H = 90 mm x 12 mm (W: horizontal width, H: vertical height).

2.1.2 Particle Image Velocimetry

Planar PIV is a non-intrusive, optical measurement technique. Seeding particles are injected into the flow field. A light source is expanded to a light sheet via proper lens system for slicing the flow volume. The illuminated particles inside the plane are recorded by a proper sensor, usually a CCD camera. The particles are registered as gray values on the image plane. Thus, the analysis of double frames, which are separated by a distinct time, allows the estimation of the planar velocity field. For that purpose, cross correlation on the gray value images is frequently applied estimating the particle displacement inside a small interrogation area. The assumption is that the flow field is smooth and not significantly influenced by rotational or shear displacements, thus yielding the zero-order translational displacement field with an additional uncertainty in measurement due to neglecting the higher-order terms. The mean translational velocity of an interrogation area is calculated by knowledge of the exact separation time. The result is a planar velocity field on a regular structured grid (Eulerian). An overview of the method is given by Raffel et al. (2007) [108].

Drawbacks of classical, planar PIV appear in three-dimensional or shear flows. Three-dimensionality results in particles moving with an angle relative to the light sheet plane resulting in the "out of plane" problem and consequently erroneous velocity vectors. High shear flows are sensitive to cross correlation approaches as particles inside the interrogation region represent different velocities. This type of measurement uncertainty can be reduced by window deformation techniques as presented by Scarano (2002) [115], but for larger computational cost.

The present quantitative PIV measurements are performed with homogenous sized (70 μm) Vestosint particles ($\rho_P \approx$ 1kg/m³) of approximately spherical shape. The neutrally buoyant seeding particles are injected directly upstream of the duct of the water channel. The particles are illuminated by a 10 mJ high speed laser with a maximum repetition rate of 10 kHz. The outlet of the laser light sheet is installed on top of the observed volume. The particle images are recorded by the mentioned high speed camera (8 GB) equipped with a telecentric lens or a long distance microscope. The side of the volume opposite to the entrance side of the laser is coloured black and the face opposite to the cameras is covered with a light absorbing mat that reduces stray reflections, thus giving a perfectly black background. The camera and the laser light sheet equipment are installed on a positioning device allowing the simultaneous shifting of laser and camera.

The system is run by Dynamic Studio 3.0. The software enables the control of the recording mode (time resolved or double pulsed) and assures the synchronization of camera and laser. The estimation of mean velocity profiles of the instantaneous flow field is performed in the double pulse mode at a repetition rate of 25 Hz resulting in 160 s recording time to assume a statistical independence in the time domain. The time resolved measurements are made at 1000 frames/s. The memory of 8GB allows measuring a sequence of about 8s.

The planar PIV images are post processed by standard software (Dynamic Studio 3.0) for calculating the velocity vector fields. The recordings are analyzed with an adaptive cross correlation meaning a window refinement of three iterations for P1-P5 (128 x128 Pix; 64 x 64 Pix; 32 x 32 Pix) with an overlap of 50% and a refinement of two iterations for P6 (128 x 128 Pix; 64 x 64 Pix) with an overlap of 50%. Outliers of velocity vectors are identified by a correlation peak validation and a velocity range validation. The invalid data yield for the symmetry planes (P1-P4) is about 1 %, the invalid data yield for P5 is 9 % and the invalid data yield for P6 is 4%. The higher invalid data of P5 results from the difficulty to seed the plane directly above the bottom floor. Rejected erroneous velocity vectors are

replaced by an averaging interpolation. The grid spacing of the velocity vectors results in a resolution of 1.4 x 1.4 mm² for P1-P5 and 0.09 x 0.09 mm² for P6.

The calculated vector fields of the time resolved measurements (1000 fps) are post processed by a temporal ensemble averaging of three vector fields ($\Delta t^*=0.14$). The number of three vector fields has been carefully chosen for two aspects: on the one hand to smooth the vector field and on the other hand for not averaging the dynamical behaviour of flow structures of interest. This has been decided by qualitative inspection. Small fluctuations corresponding to random processes are removed by the smoothing and large scale fluctuations are highlighted.

2.2 Volumetric Measurement Techniques

The measurement of a volumetric velocity field is similar to that of a planar velocity field. Differences are found in the three-dimensional representation of particle fields. Similarities are found in algorithms for the calculation of velocity fields out of recorded particle displacements. The algorithms are expanded by the third dimension allowing the volumetric description of fluid motion.

An important difference in volumetric measurement techniques is the description of particles in object space. The representation of reconstructed particles is pointwise or volumetric as shown in figure 2.3 [125]. In pointwise representation the position of a particle is described by the center of mass coordinates determined with subpixel accuracy. Hence, the information of the intensity distribution of a particle is lost. This is not the case in a volumetric representation of particles, the so called *voxel-model*. A voxel is the three-dimensional expansion of a pixel. The 3D measurement volume is discretized by voxel-elements in all three directions. The voxel space has a certain intensity distribution (lightfield) and particles are identified as clusters of coherent intensity distributions, e.g. Gaussian intensity distributions. The displacement of particles in a defined time interval (separation time) yields the velocity vector field similar to classical, planar PIV.
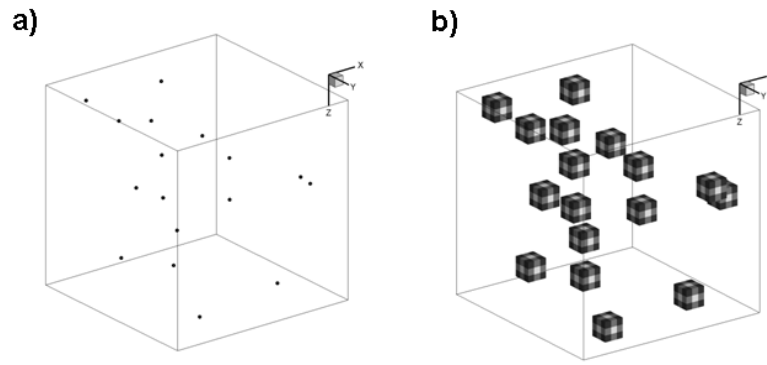
Fig 2.3 a) Pointwise representation of particles in a volumetric space **b)** Voxelwise representation of particles in a volumetric space

2.2.1 Optical Registration

A major classification of volumetric measurement techniques is the optical registration of the projection of 3D object space onto a 2D image plane. One class of techniques is based on wave optics and the other class is based on the approximation of wave optics by geometrical optics.

Wave optics is used in holography based approaches. In contrast to geometrical optics, the recorded 2D image contains information about the phase and the intensity of light (object wave). For that purpose, the sensor is illuminated by light scattered from an object (light scattering particles) and a reference wave as shown in figure 2.4 on the right. The light scattered by particles is a spherical wave. The reference wave is a plane wave. The spatial superposition of a spherical with a plane wave results in an interference pattern on the sensor, if the conditions for interference are fulfilled (coherence, monochromatic light, same polarization and spatial superposition). The advantage of holography is the nearly infinite depth of field, which is limited in techniques based on geometrical optics. Furthermore, the recorded intensity distribution contains depth information.

In geometrical optics, the intensity of the incoming light is integrated on the sensor chip. In case of PIV, the intensity distribution results from a lens projection of the illuminated particles onto the 2D sensor chip as shown in figure 2.4 on the left. A basic mathematical model for the calculation of geometrical optics is the pinhole model [125]. The pinhole model is a frequently applied model in image processing, which has been investigated and applied in hundreds of publications. Most important principles will be briefly discussed for

understanding the projection of objects space onto the image plane. For a detailed description the reader is referred to Schreer (2005) [125].
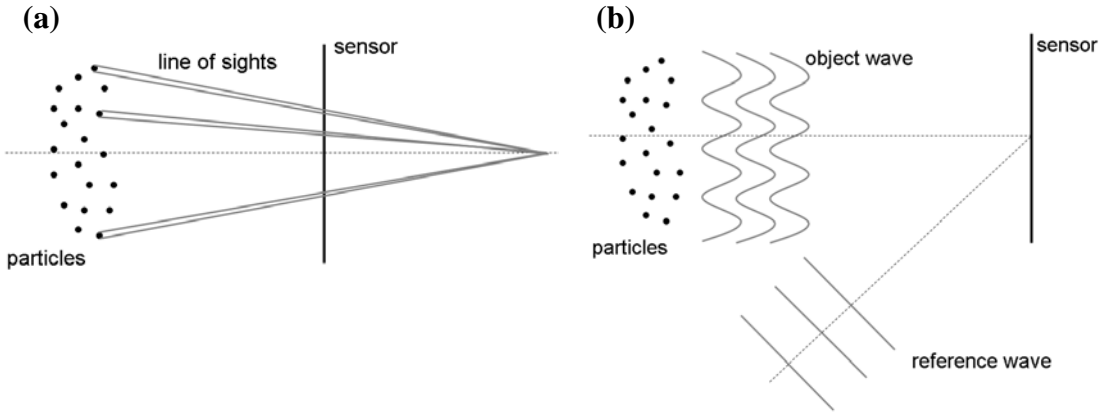
Fig 2.4 Schematically sketch of **(a)** geometrical optics **(b)** wave optics

The mapping of three-dimensional object space onto a two-dimensional image plane is called a projection. Mathematically, the projection of an object point X_w onto an image point X in pixel coordinates is described by an extern D, a perspective P' and an internal transformation A as shown in figure 2.5. The superposition of the single transformations results in the projection matrix P. The projection matrix is built in homogeneous coordinates. Thus, inhomogeneous systems of equations become homogeneous allowing simple and efficient solutions.
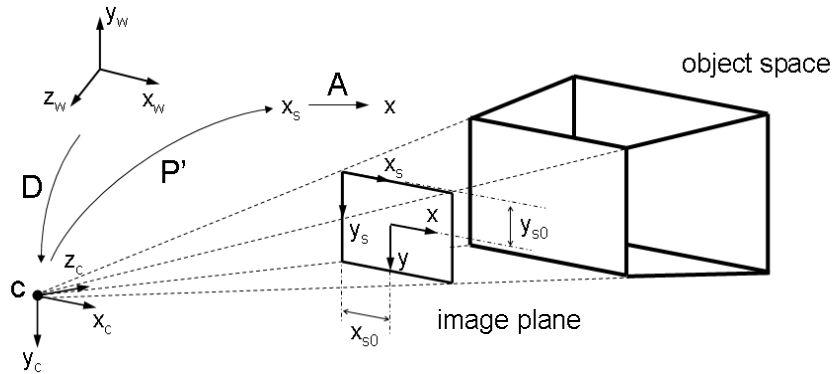
Fig 2.5 Schematic of perspective projection; D: extern transformation; P': perspective transformation, A: internal transformation, c: camera center

The extern transformation D describes the conversion of the object space coordinate system into the camera coordinate system. For that purpose, rotation and transformation is applied. The scaling factor s describes a camera specific parameter.

$$s \begin{bmatrix} x_c \\ y_c \\ z_c \\ 1 \end{bmatrix} = D \cdot \begin{bmatrix} x_w \\ y_w \\ z_w \\ 1 \end{bmatrix}, \qquad \text{with } D = \begin{bmatrix} R & t \\ 0_3^T & 1 \end{bmatrix} \qquad (2.1)$$

The 3x3 rotational matrix R is defined as the multiplications of rotation matrixs about the single directions and the translational vector t is defined as translations in the single directions.

$$R = R_x \cdot R_y \cdot R_z, \qquad t = \begin{bmatrix} t_x, t_y, t_z \end{bmatrix}^T \qquad (2.2)$$

The perspective transformation P' describes the conversion of the camera coordinate system into the sensor coordinate system. The perspective transformation with a defined focal length f is defined by the intercept theorem in pinhole optics:

$$\frac{x_s}{x_c} = \frac{y_s}{y_c} = \frac{f}{z_c} \qquad (2.3)$$

Thus, the projection from camera coordinates into sensor coordinates is defined by:

$$s \cdot \begin{bmatrix} x_s \\ y_s \\ 1 \end{bmatrix} = P' \cdot \begin{bmatrix} x_c \\ y_c \\ z_c \\ 1 \end{bmatrix}, \qquad \text{with } P' = \begin{bmatrix} f & 0 & 0 & 0 \\ 0 & f & 0 & 0 \\ 0 & 0 & 1 & 0 \end{bmatrix} \qquad (2.4)$$

The internal transformation describes the conversion via a scaling factor k of the metric sensor coordinates, e.g. [mm], into discrete sensor coordinates [pix]. Furthermore, a translation $(x_{s0}, y_{s0})^T$ on the sensor ship is considered.

$$\begin{bmatrix} x \\ y \\ 1 \end{bmatrix} = A \cdot \begin{bmatrix} x_c \\ y_c \\ z_c \\ 1 \end{bmatrix}, \qquad \text{with } A = \begin{bmatrix} k_{xs} & 0 & x_{s0} \\ 0 & k_{ys} & y_{s0} \\ 0 & 0 & 1 \end{bmatrix} \qquad (2.5)$$

The superposition of the single transformations results in the projection matrix P, which completely describes the projection of object space onto the image plane.

$$s \cdot \begin{bmatrix} x \\ y \\ 1 \end{bmatrix} = P \cdot \begin{bmatrix} x_w \\ y_w \\ z_w \\ 1 \end{bmatrix}, \qquad \text{with } P = A \cdot P' \cdot D \qquad (2.6)$$

The focus of this study is in geometrical optics, as the applied measurement technique in this thesis is referred to geometrical optics. A recent overview of holographic techniques can be found in Arroyo et al. (2008) [5].

2.2.2 Hardware

The current state of the art in hardware for acquisition is described in this chapter for measuring image based data, which means a large amount of image based data. The processing of the data results in an even larger amount of 3D velocity field data. Thus not mandatory but preferable are advanced processing and storage units. As this part is under rapid development, the current status of development in hardware requirements for advanced data processing will be pointed out.

Hardware Requirements for Acquisition

The state of the art recording device in geometrical optics is a CCD or CMOS digital camera [41]. The development of cameras with higher resolutions (4872x3248 pix², 3 fps, Prosillica GE4900) and with higher frame rates (1280x800 pix², 6242 fps, Phantom V12.1) offers the possibility to analyze unsteady flow fields in a time resolved manner at high spatial resolutions. Nevertheless, a compromise has to be made between high spatial resolution and high frame rates. Furthermore, appropriate lenses are necessary for a large depth of field. Once the measurement volume has been appropriately mapped onto the image plane, the volume has to be illuminated. Volume illumination is a crucial part in geometrical optics, it should be homogenous and of high intensity. Very large volumes, see Illmenauer barrel, are usually illuminated by high energetic continuous sources or strobe sources, where strobe sources deliver best results for illuminating large particles (1mm)

[74]. In smaller volumes the preferred illumination is a pulsed (up to several kHz) and largely expanded laser beam due to its high pulse energy (up to several mJ). Due to the expansion of the beam, the intensity distribution and homogeneity decrease. Thus, the volume, which can be recorded with high-quality particle images, is limited in its spatial extension. This problem is partially overcome in scanning or multi layer illumination devices that deliver high quality particle images at the cost of lower temporal resolution [17], [107]. A new trend for illumination is the use of pulsed LEDs as presented by Willert et al. (2010) [144]. Recent developments in LED technology result in high power LEDs with continuous radiant flux levels and even higher intensities in pulsed operation at much lower cost, making LEDs suitable for PIV applications.

In traditional holography the recording medium is e.g. silver halide holographic film. This medium offers high resolution (3000 lines/mm) and large formats (100 x 125mm³), but is not suitable for time resolved measurements. A promising material for non-digital holography is Bacteriorhodopsin, which allows superior resolution (5000 lines/mm) [10]. Nevertheless, a drawback is the erasure of the hologram at room temperature during readout. Furthermore, drawback of non-digital holography is the wet-process (chemical processing), which makes the technique unpractible for a widespread use. This is overcome in digital holography at the cost of lower resolution (100 lines/mm). Here, the film is replaced by a digital camera allowing a fast digital recording with the possibilities of image processing and numerical reconstruction [5]. In the present paper, the description of holographic techniques will be limited to digital imaging, as this technique is promising in a wide field of applications.

Hardware Requirements for Data Processing

Whilst the development of hardware paces reasonably well with the acquisition demand placed by current experiments, the ability of computers and current algorithms to transfer, process and further reduce the data within a reasonable period has fallen dramatically behind. As pointed out in 2.2.3, multi camera approaches are preferable in volumetric measurements. A typical three-camera set-up results in 6GB raw data for a recording period of 2s by assumption of the recording system applied in this thesis. Already the transfer process of the images to the computer last tens of minutes. Processing this data on high performance computers will often take many hours or even days to complete.

Originally designed for games and visualization applications, graphical processing units (GPU's) are recognized today as necessary tools for the processing of large amounts of

data in parallel. Computation is carried out in kernels, small fragment programs that operate independently of one another on separate cores. A single GPU is made up of multiprocessors, where each multiprocessor contains a number of cores. Nevertheless, up to now the coding of GPU is rather difficult and is only optimally performed by specialists. The striking point is memory read out. The flow of data is determined ultimately by the programmer, who must design the code to minimise memory conflicts. Examples of GPU implementations for PIV data processing can be found in Champagnat et al. (2009) [21] or in Schiewitz et al. [121].

2.2.3 3D Particle Reconstruction Methods

The three-dimensional reconstruction of particle positions within a measurement volume can be divided into single camera approaches and multi camera approaches. The general task of all reconstruction techniques is the extraction of three-dimensional information (object space) from two-dimensional information (camera sensor).

Single Camera Approaches

The advantage of single camera approaches is the simple experimental setup compared to multi camera approaches, where a precise multi camera calibration is mandatory. Furthermore, the costs for such a set-up are much lower. A drawback is the lower permissible number particle density, which strongly limits the spatial resolution.

To the authors knowledge there are two approaches in fluid mechanics using a single camera based on geometrical optics. The first approach is presented by Willert and Gharib (1992) [145], the defocusing technique. The technique is based on a single camera equipped with a three-hole aperture. A single particle is imaged on the sensor chip as three particles forming an equilateral triangle as shown in figure 2.6. By analyzing the positions and the lengths of the triangles, the information of depth position can be extracted. Originally, the result is a pointwise reconstructed particle field. Pereira et al. (2002) blow up the infinitesimal small point to a voluminous particle with a Gaussian intensity distribution to have voxel based description of the measurement volume [99]. A drawback in this defocusing technique is the need for a high intensity illumination source due to the small aperture of the holes reducing largely the light amount integrated on the sensor. Furthermore, the spatial resolution is rather coarse. An increasing number particle density results in overlapping triangles and consequently in problems of detection.
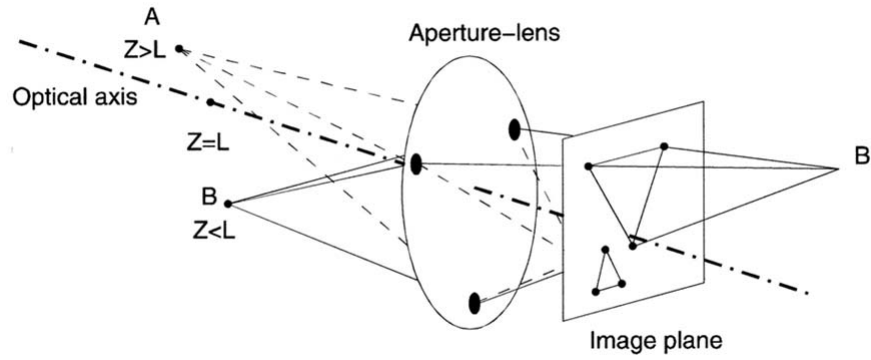
Fig 2.6 Three Aperture defocusing arrangement; triangle on image plane contains relative position to a reference plane at Z=L [36]

The second approach is presented by Hain et al. (2009) [40]. The authors propose the analysis of defined optical aberrations, namely astigmatism, to include depth information beside the 2D sensor information (wave front deformation). The particle images are deformed in an elliptical manner depending on the depth position, thus delivering the possibility to analyze the shapes of the particle images and to extract depth information. Up to now the technique has been limited to the reconstruction of very small measurement volumes. The result is a pointwise reconstructed particle field.

A wave optics based single camera approach is digital holography [123]. In contrast to afore mentioned single camera techniques the result is a 3D intensity distribution of the particle field. Here, different kind of optical set-ups have been investigated in the last decade, especially in photographic holography. Nevertheless, the advantages and drawbacks are adaptable to digital holography. Typical methods applied to PIV are in-line holography [136], [85], off-axis holography [103], [85] and phase shifting holography [8]. In in-line holography illumination beam and reference beam are identical. A schematic of a typical set-up is shown in figure 2.7. A coherent light source is arranged in-line with the sensor chip. A lens system generates a collimated beam, which is used to illuminate tracer particles. The scattered light is used as object wave and the undisturbed illumination beam, passing through the particles, represents the reference beam resulting in a simple and stable set-up. However, if particle density is increased, there won't be enough undisturbed light for the reference beam. This is overcome in off-axis holography, where illumination beam and reference beam are decoupled. This is obtained with the loss of inherent interference conditions resulting in a more complicated optical set-up. Up to now, commonly used in digital holographic PIV applications is the in-line holography, probably due to its robust and simple set-up compared to other holographic set-ups [75], [97].
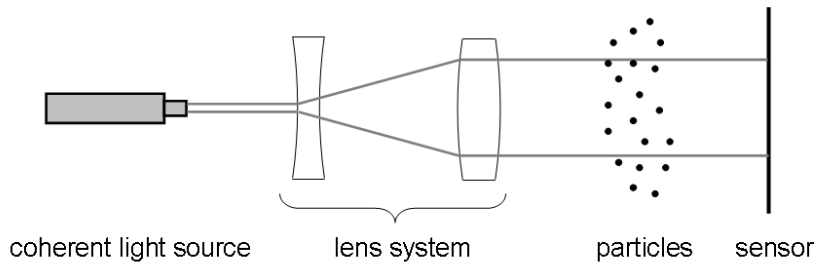
Fig 2.7 Experimental set-up of in-line holography

Once the interference patterns are recorded on the CCD-Chip, the digital hologram can be numerically reconstructed in object space resulting in an intensity distribution in discretized object space. All algorithms for numerical reconstruction of the voluminous intensity field are based on the Rayleigh-Sommerfeld diffraction theory [5]. An overview of numerical reconstructions (Fresnel-Kirchoff integral, Fresnel approximation, convolution approach) is described in [122]. Other reconstruction techniques are the wavelet transformation [19] and fractional-order Fourier transformation [25]. As mentioned, the result is a light intensity field. Thus, when looking at the 3D image of a particle, the original shape of a spherical particle is not reconstructed. The particles are stretched in depth direction, while maintaining the circular shape in the cross section plane [85]. The problem is referred to as depth-of-field problem [98]. As a consequence, the 3D position of a particle has lower accuracy in depth than in the in-plane [75]. Up to now, the measurement volumes in digital holographic PIV are limited to small volumes. In [83] a measurement volume of 15x15x64 mm³ with a seeding density of roughly 4 particles/mm³ is reconstructed. The advantages of digital holographic PIV are found in three-dimensional information stored on the 2D camera sensor and in the large depth of field. Drawbacks are the small achievable volumes (dependent on the size of the chip), the resolution of digital sensors and the poor accuracy in depth position [75].

Multi-Camera Approaches

Multi-camera approaches are manifold in literature. The idea of multi-camera approaches is the combination of multiple 2D information to obtain 3D information. For that purpose, the cameras record the measurement volume from different angular directions. Voxelwise as well as pointwise reconstruction techniques take advantage of intersecting lines of sight. Visually speaking, lines of sight are shot out of the image planes and intersect in a 3D point/voxel in object space. In principle, the 3D reconstruction of a point or voxel needs at

least two cameras recording the object scene from different angular directions. However, due to a large number of particle images, a multi camera set-up is preferable to avoid ambiguities or ghost particles [78]. Typically, a three or four camera set-up is used, see figure 2.8 for a typical volumetric three-camera set-up. A precise calibration procedure is mandatory for all multi-camera techniques to obtain the orientations of the cameras. For that purpose, a three-dimensional calibration target with known control points is necessary. The control points are recorded from each camera. After the extraction of the two-dimensional centroid position of the control markers in the image planes, the known 3D positions are compared with the calculated 2D sensor positions. For a finite number of control points, the observations result in an over-determined system of equations, which can be solved by e.g. iterative least squares procedures.
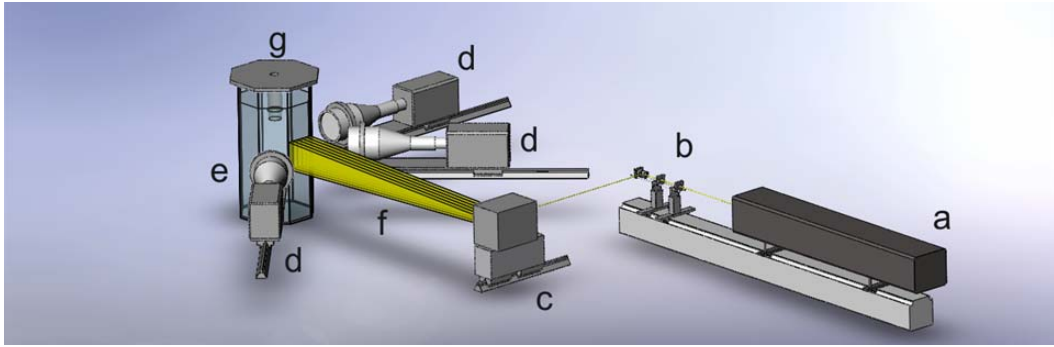
Fig 2.8 Experimental set-up: a) Ar-Ion-laser, b) lens system, c) rotating mirror drum, d) high speed camera, e) octagon, f) light sheets, g) vortex generator [64]

The *pointwise reconstruction*, so-called stereo-triangulation, is primarily performed in classical 3D PTV [78]. By knowledge of the 2D centroid positions of a homologous particle in the single image planes and by knowledge of the single projection matrixs, the 3D point position is reconstructed by proper reconstruction techniques (homogeneous or inhomogeneous method [125]). In detail, lines of sight are shot out of the image planes and the intersection point of these lines defines the volumetric position. Due to improper calibration, improper estimation of 2D centroid positions and optical errors, the lines of sight are usually skewed. Thus, the center between the shortest distances of the lines is chosen. In the following, the inhomogeneous method for pointwise reconstruction is described. In a stereoscopic set-up, where subscript 1 indicates the first camera and subscript 2 the second camera, equation 2.6 is written as:

$$s_1 \cdot \begin{bmatrix} x_1 \\ y_1 \\ 1 \end{bmatrix} = P_1 \cdot \begin{bmatrix} x_w \\ y_w \\ z_w \\ 1 \end{bmatrix} \qquad s_2 \cdot \begin{bmatrix} x_2 \\ y_2 \\ 1 \end{bmatrix} = P_2 \cdot \begin{bmatrix} x_w \\ y_w \\ z_w \\ 1 \end{bmatrix} \qquad (2.7)$$

By assumption of identical cameras ($s_1=s_2$), the vector product results in an over-determined system of equation in the form EX=0:

$$EX_W = \begin{bmatrix} p_1^{11} - x_1 p_1^{31} & p_1^{12} - x_1 p_1^{32} & p_1^{13} - x_1 p_1^{33} & p_1^{14} - x_1 p_1^{34} \\ p_1^{21} - y_1 p_1^{31} & p_1^{22} - y_1 p_1^{32} & p_1^{23} - y_1 p_1^{33} & p_1^{24} - y_1 p_1^{34} \\ p_2^{11} - x_2 p_2^{31} & p_2^{12} - x_2 p_2^{32} & p_2^{13} - x_2 p_2^{33} & p_2^{14} - x_2 p_2^{34} \\ p_2^{21} - y_2 p_2^{31} & p_2^{22} - y_2 p_2^{32} & p_2^{23} - y_2 p_2^{33} & p_2^{24} - y_2 p_2^{34} \end{bmatrix} \begin{bmatrix} X_w \\ Y_w \\ Z_w \\ 1 \end{bmatrix} = 0 \qquad (2.8)$$

The decomposition of E into:

$$B = \begin{bmatrix} e_{11} & e_{12} & e_{13} \\ e_{21} & e_{22} & e_{23} \\ e_{31} & e_{32} & e_{33} \\ e_{41} & e_{42} & e_{43} \end{bmatrix} \quad \text{and} \quad c = \begin{bmatrix} e_{14} \\ e_{24} \\ e_{34} \\ e_{44} \end{bmatrix} \qquad (2.9)$$

results in:

$$B \cdot (x_w, y_w, z_w)^T = c \qquad (2.10)$$

If B^TB is invertible, the solution for the three-dimensional position X_w is:

$$X_W = B^T B^{-1} B^T c \qquad (2.11)$$

For the identification of homologous particles in different camera views a rather strong tool is described in literature, the epipolar line [125]. It describes, that a point, which is found in one camera, lies along a line in the second camera as shown in figure 2.9. The two-dimensional search area is reduced to one dimension, namely along the epipolar line. Mathematically, the relation between both cameras is described by the fundamental matrix F. The relation of both 2D point positions (x_1, y_1), (x_2, y_2) of the same 3D point is called epipolar equation and the line l_2 is called epipolar line:

$$\begin{pmatrix} x_2 & y_2 & 1 \end{pmatrix} \cdot F \cdot \begin{pmatrix} x_1 \\ y_1 \\ 1 \end{pmatrix} = 0 \qquad , l_2 = F \cdot \begin{pmatrix} x_1 \\ y_1 \\ 1 \end{pmatrix} \tag{2.12}$$

The evaluation of F is made within the calibration of the projection matrixs. The fundamental matrix for each camera combination is determined by comparing homologous centroid positions in the images. If the 2D positions of the target markers in the camera images have been localized, F is evaluated e.g. with the 8-point algorithm expanded by the Frobenius-norm [125], which needs 8 homologous 2D positions. In practice, it is common to use more than several hundred positions to determine F.

The difficulty in identification of homologous particles in the image planes increases with increasing number particle density. A particle image usually contains $>10^3$ particles, which do not strongly vary in shape, size or intensity. Thus, a reduction of spatial ambiguities due to imaging characteristics is not sufficient. Here, the geometrical condition *epipolar line intersection* is more appropriate to identify homologous particles [78]. The method needs at least three cameras, whereas further viewing direction will reduce ambiguities. By proper arrangement of the cameras, the epipolar lines between all camera combinations will intersect near the homologous 2D point positions. Nevertheless, as particle density is increased, a new problem arises due to overlapping particle images, which cannot be identified as separate particle images on the sensor plane. Thus, the number of particles is limited to the order of 10^3 for a four camera set-up in pointwise reconstruction techniques for a typical sensor size of 1000x1000 pix [48]. The size of the measurement volume or size of the reconstructed volume can range up to several cubic meters depending on the mapping system [14]. However, the larger the measurement volume, the lower becomes the spatial resolution.
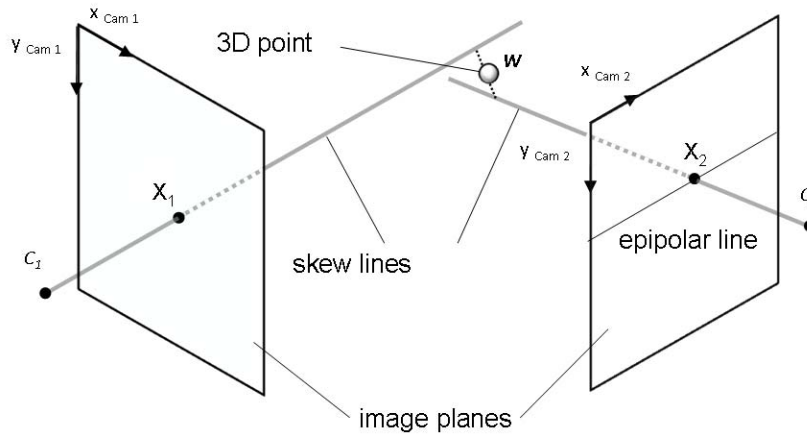
Fig 2.9 Schematic of stereoscopic camera set-up: stereo-triangulation and reconstructed epipolar line

Another, rather elegant, system for pointwise reconstruction is the patented V3V-system [101]. The single body system takes advantage of multi-sensors in combination with the defocusing concept described above [99]. Three sensors are arranged in a coplanar triangle pattern each illuminated by a one-hole aperture. Thus, homologous particle identification on the three sensor chips is performed, to the author's point of view, by intersecting epipolar lines, although not mentioned by [101]. Due to the arrangement of the chips and apertures, the identified homologous particles build a triangle as in [145]. The center of the triangle identifies the in-plane coordinate and the size of the triangle the depth position. The multi sensors allow higher number particle densities compared with the single camera three-hole aperture system, because the sensor configuration is extended from one sensor to three sensors.
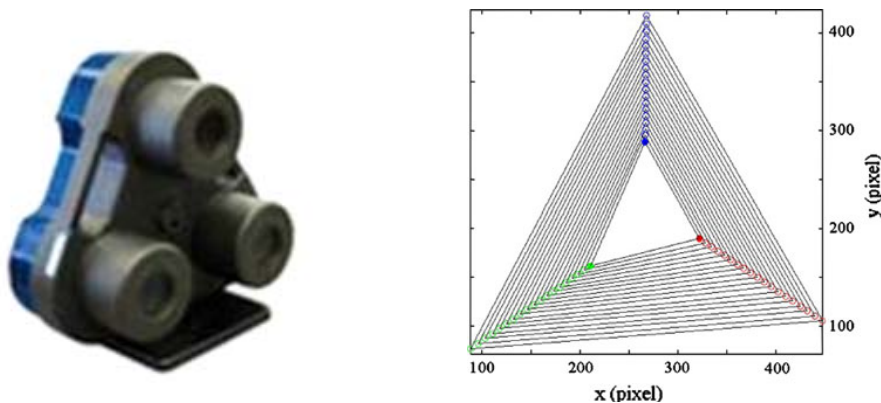
Fig 2.10 Patented V3V system; three-camera system in a single body **(left)**; Calibration triplets at multiple planes through the measurement volume [148] **(right)**

Volumetric reconstruction - in contrast to pointwise reconstruction - doesn't need the identification of homologous particles in different camera views, thus allowing higher

seeding densities for the cost of ghost particles. Ghost particles are reconstructed ambiguities decreasing the reconstruction quality. All volumetric reconstruction techniques are based on the shape from silhouette method [70]. Each pixel of a particle image, defined by a finite number of pixels, is projected into 3D space via the line of sight. If this is done for each camera, the lines of sights intersect in object space and generate a visual hull of the 3D particle. It is obvious that the more cameras are used, the more precise the description of the particle will be. For that purpose, all volumetric reconstruction techniques use the *voxel-model*. The characteristics of volumetric reconstruction of intensity distributions within the measurement volume in PIV are on the one hand the discretized particle distributions from a limited number of viewing directions and, on the other hand, high spatial frequencies. Thus, algebraic reconstruction methods are more appropriate than Fourier or back projection methods [33]. A schematic of the algebraic reconstruction techniques is shown in figure 2.11. The figure shows the top view of the pre-defined voxel space. Filled voxel elements represent intensity values greater than a certain threshold.
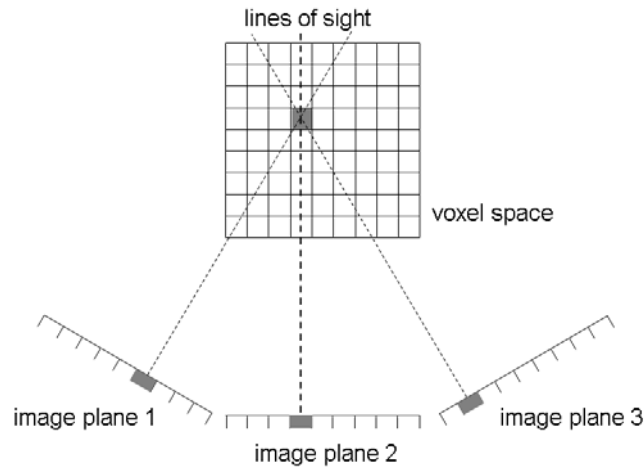
Fig 2.11 Schematic of multi-camera algebraic reconstruction technique.

Since Elsinga et al. (2006) [34], a number of algorithms and algorithmic refinements for the application in PIV are proposed in literature. The conventional line of sight reconstruction is found in multiplicative algebraic reconstruction technique (MART) [45], in adaptive algebraic reconstruction technique (AART) [76], in improved iterative algorithm for sparse object reconstruction (IIASOR) [72] and in simultaneous iterative reconstruction technique (SIRT) [45]. The basic principle is that the recorded intensity on each pixel of the camera is the result of an integration of intensity along the line of sight. The integral description of pixel intensity can be discretized due to the voxel-model and

expressed as the sum of a weighting matrix multiplied (MART) by the voxel intensity along the line of sight. The weighting matrix includes the camera parameters that connect a voxel in object space and a pixel in the image plane. This results in an under-determined system of linear equations. An iterative correction of the voxel intensity is performed until the intensity distribution of the pixels in each projection is satisfied within defined error limits.

The reconstruction algorithms mentioned afore have been tested with respect to PIV by [7]. The results show that MART and AART deliver the highest quality of reconstruction. The main problems of MART and AART are the large computational processing overhead due to the iterations and the fine voxel grid as well as the intensive cost for memory in order to store the weighting matrix for each voxel. Improvements in accelerating the iterative reconstruction are published by Atkinson and Soria (2009) [6]. Possible particle locations in the voxel volume are determined by intersecting lines-of-sight. This method circumvents the use of memory intensive weighting matrixs in regions without particles.

Furthermore, non-iterative methods for 3D particle reconstruction have been presented. In Putze (2008) [105] a method is described, which is based on a multiple projective transformation of each camera image into depth layers of the object space using transformation parameters derived from the camera orientation and calibration parameters. For that purpose, the contents of each camera are transformed depth-layer wise into the predefined voxel intensity field. A schematic sketch of multiple projective transformations is shown in figure 2.12 for one exemplary camera.
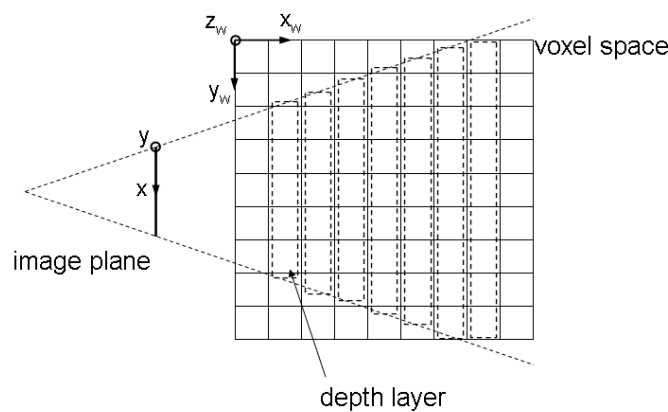
Fig 2.12 Schematic of depth layer reconstruction

In the course of this thesis, an alternative reconstruction technique is developed, which is described in detail in Kitzhofer and Brücker (2010) [64]. A simplified reconstruction method is proposed, which is based on telecentric imaging. The reconstruction is

performed as a multiple combination of pair-wise reconstructed voxel spaces using the epipolar geometry pixelwise in a set-up with three or more cameras. The principal processing steps are indicated in figure 2.13. A multi camera set-up is given (in this case a 3 camera set-up) recording particles in the object space. The camera set-up is virtually separated into all possible camera pairs. Gray value weighted voxel spaces are then reconstructed for each camera pair. The pair wise tomographic reconstruction of the single voxel spaces is realized by using the epipolar geometry. For that purpose, the epipolar geometry is applied pixel wise. Thereafter, the voxel spaces are transformed into one common voxel space. An up to now basic condition of the described method is the parallel projection resulting from telecentric imaging. Advantages can be seen in the non-iterative process and a simplified understanding due to the underlying parallel projection.
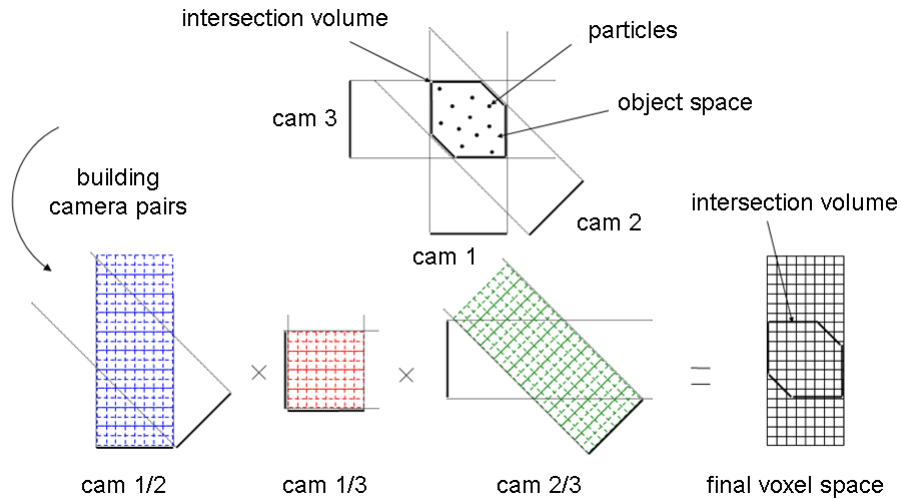
Fig 2.13 Principal sketch of multiple pair wise tomographic reconstruction; blue rectangle: reconstructed voxel space cam1/2, red rectangle: reconstructed voxel space cam 1/3, green rectangle: reconstructed voxel space cam 2/3, black rectangle: final combined voxel space

A multi-camera approach belonging to holographic recording technique is presented by Soria and Atkinson (2008) [132]. The motivation is the elimination of the depth-of-field problem in holographic reconstruction of particles. The principle is the multiplicative combination of several reconstructed intensity fields, which are recorded from different directions. The single intensity fields are reconstructed via wave optics and the final intensity field is combined by multiplication of the single volumes.

A detailed literature review of existing techniques for three-dimensional reconstruction of a particle space has been presented. One and multi-camera approaches, pointwise and volumetric reconstruction techniques as well as optical and wave optics approaches are presented. The review shows that holographic techniques are, up to now, not practicable for analysis of large datasets. Furthermore, possible sizes of measurement volumes are far away from the volume measured in this thesis (90x60x15 mm³). Nevertheless, digital holography will be of further value for PIV due to recording all necessary information for three-dimensional reconstruction in a single record.

Volumetric reconstruction has become a key issue in three-dimensional reconstruction of particle fields. Striking is the achievable number particle density for the cost of ghost particles. Nevertheless, processing times are much larger than that of pointwise reconstruction. Beside the iterative process performed in volumetric reconstructions, the number of operations is larger. Take one single particle of finite size 3x3pix. The reconstruction results in 27 voxel elements in object space. Thus, 27 operations are performed in volumetric reconstruction. In pointwise description, the 3x3 particle is reduced to a single point resulting in one operation for three-dimensional reconstruction.

2.2.4 3D Velocity Field Generation

Once the measurement volume is reconstructed at consecutive time steps (volumetric or pointwise) the volume can be analyzed for fluid motion. The description of fluid motion is performed in the Eulerian or in the Lagrangian frame. Both differ in necessary algorithms, particle densities, spatial structure and information. The spatial data representation in the Eulerian frame is characterized by a fixed structured grid. In case of PIV, the calculated velocity vector represents time varying median particle displacements within the interrogation areas. The velocity field in the Lagrangian frame is described on scattered, spatially and temporally varying positions as shown in figure 2.14.
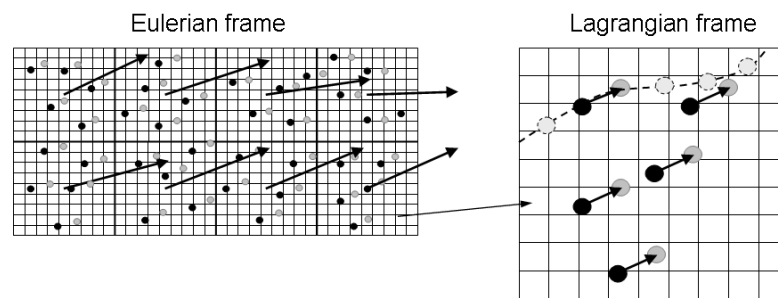
Fig 2.14 Comparison of Eulerian frame and Lagrangian frame

Lagrangian Description

The velocity field in the Lagrangian frame determined from PTV-methods results from individual particle detection schemes and analysis of single particle displacements and paths. For that purpose, accurate particle detection algorithms and suitable particle tracking algorithms are mandatory.

First step in the evaluation of particle trajectories is the detection of single particles. This is performed via segmentation. Segmentation is the grouping of connected pixels to an individual particle. Methods frequently applied are region growing and thresholding. In region growing the particle is detected by successively increasing the structure, started with an elementary pixel. The boundary is defined by proper thresholding. Here, a global or local threshold is applicable, which is rather dependent on the quality of particle images. A local threshold is preferable in lower quality particle images, e.g. if a strong background noise is apparent.

Once clusters of pixels are identified to belong to an individual particle, the centroid position is determined with sub-pixel accuracy. A comparison of several algorithms is numerically performed by Ponitz (2010) [100]. The influence of noise, size and subpixel position is analyzed. Table 2.1 summarizes median deviation and processing time of the

analyzed methods. The 2D Gauß-fit delivers highest quality for the cost of long processing time. The calculation is performed with Matlab R2008b on a single core at 2.66 GHz. Of slightly less accuracy, but with shorter processing times is the gray-value weighted center of area.

Method	Deviation [pix]	Processing time [ms]
Pixel maximum intensity	0.36	0.001
Bounding box	0.24	0.009
Center of area	0.09	0.015
Gray-value weighted center of area	0.02	0.006
Gauß-fit	0.01	1.934

Table 2.1 Comparison in median accuracy and processing time of methods for evaluation of centroid positions of particles

Next step in PTV is the tracking of single particle positions. Here, tracking is performed in 2D, in 3D or as a combination of both, depending on the flow problem. Since [82], several proposals for tracking particles in a spatial-time domain are considered in literature. The proposals are based on kinematic analysis [95], analysis of probabilities [9], conservation of energy [93], on binary image cross correlations [151], or on the analysis of the velocity gradient tensor [56], to mention only a few. Willneff (2003) presents a spatio-temporal algorithm, which combines image based and object space based information of particles at consecutive time steps [147].

A generally accepted criterion for the difficulty in tracking single particles is given by Malik et al. (1993) [82]. The criterion compares mean particle-to-particle distances with mean flow displacements.

$$e = \frac{\Delta s}{u \cdot \Delta t} \qquad (2.13)$$

The value e can be interpreted as the difficulty to track particles correctly. If the mean particle-to-particle distance Δs in one single frame in image plane or voxel space is much higher than the mean particle displacement from one frame to the next frame, meaning $e \gg 1$, the tracking is easy. If $e < 1$ the tracking is getting nearly impossible.

The principal limit of PTV for an idealized, homogenously distributed 2D particle image resulting from the difficulty in tracking is shown in figure 2.15. The figure shows the

particle density ppp as a function of the maximum particle displacement $d_{max} = v \cdot \Delta t$ for different difficulties e of tracking in a 2D image. The figure has been constructed in the following manner: A given particle density ppp results in a mean particle-to-particle distance in the 2D image for homogenous distributed particles. The maximum particle displacement results from a given value e for difficulty in tracking. Although the graph shows the limit in 2D tracking, which is more difficult than 3D tracking, the principal tendencies are the same in 2D and 3D.
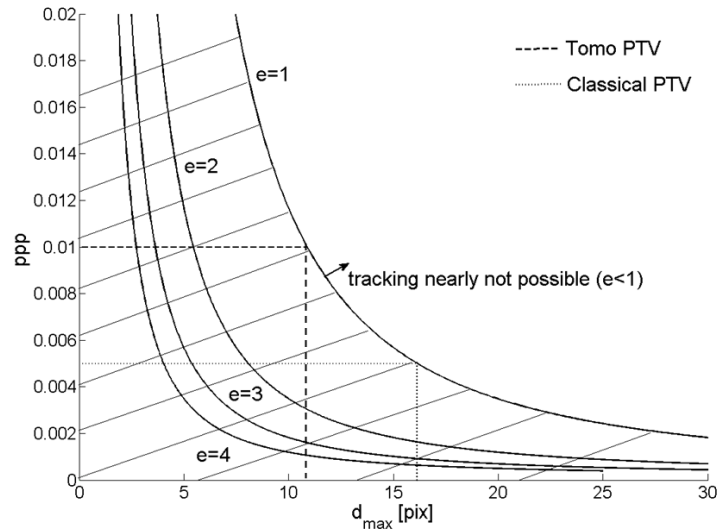
Fig 2.15 Theoretical limits in PTV (tomographic and classical), limit of number particle density in classical PTV resulting from a 3 camera set-up (dotted line), estimated limit of number particle density in Tomo PTV resulting from a 3 camera set-up (slashed dotted line); shaded area: tracking of particles is possible [64]

The proposed criterion identifies difficulties with the assumption that all necessary particle positions are reconstructed correctly. However, in practical applications the tracking is made more difficult due to insufficient reconstructed particle positions resulting from ambiguities and overlapping particle images. In pointwise reconstruction techniques the number particle density in 3D PTV is limited to about 0.005 ppp due to afore mentioned ambiguities and overlapping particle images [78]. The problem is overcome in volumetric reconstruction techniques (Tomo PTV) shifting the number particle densities to about 0.01 ppp [64]. Here, centroid positions of the particles are determined in voxel space due to the intensity distribution, similar to Holographic PTV. The higher number particle density is achieved at the cost of generating ghost particles. The influence of ghost particles in the yield, which is defined as the estimated links divided by the real number of links, is clearly visible in figure 2.16. The figure shows the yield as a function of number particle density.

The figure is generated with respect to a simulation of a 3D velocity field with an aspect ratio of 1 (100x100x100 voxel). The instantaneous turbulent flow field is generated with Open FOAM V1.5 (Tool: BoxTurb). For that purpose, the flow field is filled with homogenous sized particles (7 voxel) at random positions with a Gaussian 3D intensity distribution and parallel projected onto three 100 x 100 pixel² image planes as shown in figure 2.13. The separation time between the frames has been chosen to have a median particle displacement of 3 pix resulting in e ≈ 6 for 0.005 ppp and e ≈ 4 for 0.01 ppp. For both densities, e is much bigger than 1 making the tracking itself easy. The results show the main influence of particle density on the quality of pointwise and of volumetric reconstruction techniques.
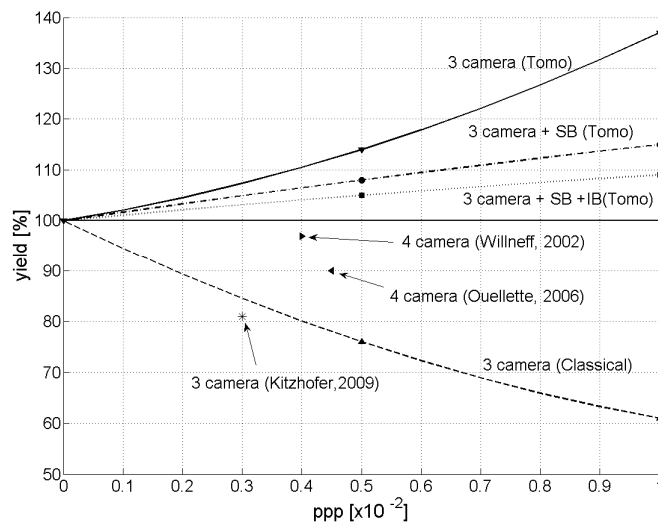
Fig 2.16 Particle matching yield for different PTV methods, classical approach: yield < 100% because of problems in stereo matching and overlapping particle images, tomographic approach: yield > 100% because yield includes ghost particles [64]

A characteristic difference between classical 3D PTV and Tomo PTV is expressed in the calculated value of the yield. In classical 3D PTV methods, the yield is smaller than 100% and decreases with an increasing number of particles. The reason is an increase of overlapping particle images and growing difficulties in stereo matching with increasing seeding density. In Tomo PTV the yield is higher than 100% due to the reconstructed ghost particles forming ghost trajectories. In contrast to classical 3D PTV the necessary optimization of Tomo PTV is reducing the yield to a value of 100 %, whereas the optimization in classical PTV is increasing the yield to a value of 100 %.

In classical PTV with a 4 camera setup the practical limit of particle density is 0.005 ppp. With a further increase of the particle density up to 0.01 ppp, the 3 camera setup is able to

link only 60 % of the particles in a correct way. In Tomo PTV, the yield of the 3 camera set-up is 137 % at 0.01 ppp. This value can be reduced down to 109 % using further criteria to remove ghost particles from the voxel space. A size based criterion (particles are represented by connected voxels of certain intensity) for detecting ghost particles reduces the yield about 15 % leading to an absolute yield of 115 %. Furthermore, an intensity based detection criterion reduces the yield to 109 %, meaning that 9 % of the links are ghost links. The remaining 9 % can be further reduced within the tracking procedure using the information of temporal behaviour within the voxel space. For that purpose, the detection of ghost particles changes to the detection of ghost trajectories.

Figure 2.17 exemplarily shows a typical experimental result for a volumetric reconstructed single particle trajectory and its local neighbours. The true particle path is visible as a long spiral track surrounded by some fragments of ghost trajectories.

The criteria to remove erroneous ghost trajectories can be interpreted as a kind of safe threshold. Most of the ghost trajectories are of small lengths less than 3 - 4 frames. In general, the length of the short ghost trajectories depends on the size and the velocity of the particle images. At constant velocity, the length of a ghost trajectory produced by a small sized particle image will be shorter than that produced by a big sized particle image. In addition, particle paths containing only three frames don't contain much valuable information for a fluid mechanical interpretation. Thus a cut off is made, which has to be chosen carefully for not deleting true particle paths.
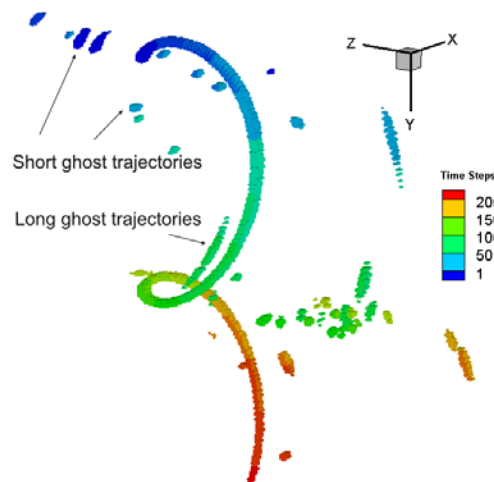
Fig 2.17 Reconstructed trajectory and environment in temporal development (short and long ghost trajectories); the trajectories are colour coded with time steps. The reconstructed path contains 205 frames.

For the detection of long ghost trajectory, a first guess proves similarities of trajectories in 3D space. This is a check for frame identity, speed, direction and change in direction.

Trajectories fitting these conditions are compared. Long parallel ghost trajectories have a characteristic blinking. The particle path has gaps. Furthermore, a characteristic of this kind of ghost trajectory is the particle size of the particle building a trajectory. The particle size in true trajectories is nearly constant. The particle size of ghost trajectories changes while moving along the particle path. If these criteria fit a selected trajectory of the first guess, the trajectory is detected to be a ghost trajectory and is deleted. Figure 2.18 shows the result of Tomo PTV of the benchmark experiment of a vortex ring.
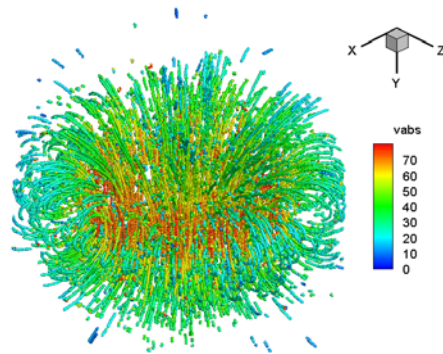
Fig 2.18 Direct 3D visualization of Lagrangian trajectories obtained by Tomographic Particle Tracking Velocimetry in case of the vortex ring experiment [64]. The measurement volume is approximately 90 x 90 x 90 mm³. The result contains 30 frames.

Regarding computing performance, particle tracking techniques in themselves do not apply well to large scale multiprocessor architectures due to the inherent nature of tracking particle histories. Typically, a large queue of detected particles over a time are recorded and then - in very much a serialised manner - tracks are determined for those particles whose positions most likely fulfil a set of criteria. A considerable amount of data sorting is necessary to reduce repetition. Some performance improvement is still possible through multithreading, though true parallel processing is not possible.

Eulerian Description

The velocity field in the Eulerian frame is represented by velocity vectors located on a structured grid in flow space. In case of PIV, the calculated velocity vector represents mean particle displacements within the interrogation areas, indicated in figure 2.14. Advantage of the representation of the flow by the Eulerian velocity field is the frequent application in fluid mechanical investigations in the last decades. Thus, several tools for further analysis of the Eulerian velocity field are already available in literature resulting in several detection schemes for coherent structures. Some examples are vortices,

separation/reattachment lines, shear layers, recirculation regions, stable/unstable manifolds or topology based structures.

Algorithms for the calculation of mean particle displacements are 3D Cross Correlation and 3D Least Squares Matching. Both methods need a light intensity field, thus volumetric reconstruction or blow up of the pointwise description is mandatory.

To the author's knowledge, 3D cross correlation was first applied in [99]. Here, pointwise particle positions were blown up by a Gaussian intensity distribution in voxel description. Meanwhile, 3D cross correlation in intensity filled voxel spaces is standard [34]. The three velocity vector components are obtained by cross correlation of two 3D intensity maps corresponding to subsequent exposures of the particle images. The accuracy in velocity vectors is increased by volume deformation techniques analogue to the 2D counterpart of window deformation [114].
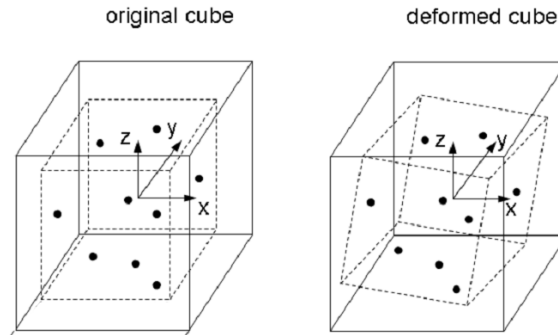
Fig 2.19 Schematic of cube transformation; dots: volumetric particles; solid line: measurement volume, dashed line: interrogation volume. The gray values of the voxel spaces are replaced by pointwise particles positions for visual clarity.

3-D Least Squares Matching (3D LSM) is a volumetric tracking technique, which is adaptive to deformation and rotation of the interrogation volume. It was first introduced in [79] for tracking structures in 3D Laser Induced Fluorescence data. It is an iterative least squares adjustment procedure, where the gray values of the interrogation volume at time step one are transformed into the gray values of the interrogation volume at time step two as indicated in figure 2.19. This results in estimations for translation and deformations of a fluid element. Up to now, the applied geometric transformation between the two volumes is a 3-D affine transformation, which might also be replaced by non-linear cubic transformations [80]:

$$
\left.
\begin{aligned}
x_2 &= a_0 + a_1 \cdot dx_1 + a_2 \cdot dy_1 + a_3 \cdot dz_1 \\
y_2 &= b_0 + b_1 \cdot dx_1 + b_2 \cdot dy_1 + b_3 \cdot dz_1 \\
z_2 &= c_0 + c_1 \cdot dx_1 + c_2 \cdot dy_1 + c_3 \cdot dz_1
\end{aligned}
\right|_E
\tag{2.14}
$$

The variables a_i, b_i, c_i (i = 0,1,2,3) are the parameters of the affine transformation and can be estimated within a Gauss-Markov Model. The parameters a_0, b_0 and c_0 are displacements valid for each point within the infinitesimal cuboid E. The remaining nine parameters describe shear, rotation and strain.

In addition to the *three translational velocity vectors,* the parameters of the 3-D affine transformation contain the information of *strength and direction of deformation.* Thus, the direct calculation of the velocity gradient tensor is possible [67], which is a basic element in the extraction of coherent structures. The velocity gradient tensor or Jacobian of the velocity field is defined as:

$$
J = \nabla \underline{u} =
\begin{bmatrix}
\dfrac{\partial u}{\partial x} & \dfrac{\partial u}{\partial y} & \dfrac{\partial u}{\partial z} \\[2ex]
\dfrac{\partial v}{\partial x} & \dfrac{\partial v}{\partial y} & \dfrac{\partial v}{\partial z} \\[2ex]
\dfrac{\partial w}{\partial x} & \dfrac{\partial w}{\partial y} & \dfrac{\partial w}{\partial z}
\end{bmatrix}
\tag{2.15}
$$

The Jacobian can be split into a symmetric and an anti-symmetric part, namely the rate-of-rotation tensor $\Omega = \frac{1}{2}(J - J^{T})$ and the rate-of-strain tensor $S = \frac{1}{2}(J + J^{T})$.

$$
J = \Omega + S
\tag{2.16}
$$

The deformation rate tensor describes strain $\varepsilon_{ij,\ i=j}$ and shear $\varepsilon_{ij,\ i \neq j}$ of the infinitesimal volume element resulting from velocity gradients in the inner of the volume.

$$
S =
\begin{pmatrix}
\dfrac{\partial u}{\partial x} & \dfrac{1}{2}\left(\dfrac{\partial v}{\partial x}+\dfrac{\partial u}{\partial y}\right) & \dfrac{1}{2}\left(\dfrac{\partial u}{\partial z}+\dfrac{\partial w}{\partial x}\right) \\[2ex]
\dfrac{1}{2}\left(\dfrac{\partial v}{\partial x}+\dfrac{\partial u}{\partial y}\right) & \dfrac{\partial v}{\partial y} & \dfrac{1}{2}\left(\dfrac{\partial w}{\partial y}+\dfrac{\partial v}{\partial z}\right) \\[2ex]
\dfrac{1}{2}\left(\dfrac{\partial u}{\partial z}+\dfrac{\partial w}{\partial x}\right) & \dfrac{1}{2}\left(\dfrac{\partial w}{\partial y}+\dfrac{\partial v}{\partial z}\right) & \dfrac{\partial w}{\partial z}
\end{pmatrix}
=
\begin{bmatrix}
\varepsilon_{xx} & \varepsilon_{xy} & \varepsilon_{xz} \\
\varepsilon_{yx} & \varepsilon_{yy} & \varepsilon_{yz} \\
\varepsilon_{zx} & \varepsilon_{zy} & \varepsilon_{zz}
\end{bmatrix}
\tag{2.17}
$$

The rotation rate tensor describes the vorticity ω in each spatial direction x, y, z.

$$\Omega = \begin{bmatrix} 0 & -\dfrac{1}{2}\left(\dfrac{\partial v}{\partial x}-\dfrac{\partial u}{\partial y}\right) & \dfrac{1}{2}\left(\dfrac{\partial u}{\partial z}-\dfrac{\partial w}{\partial x}\right) \\ \dfrac{1}{2}\left(\dfrac{\partial v}{\partial x}-\dfrac{\partial u}{\partial y}\right) & 0 & -\dfrac{1}{2}\left(\dfrac{\partial w}{\partial y}-\dfrac{\partial v}{\partial z}\right) \\ -\dfrac{1}{2}\left(\dfrac{\partial u}{\partial z}-\dfrac{\partial w}{\partial x}\right) & \dfrac{1}{2}\left(\dfrac{\partial w}{\partial y}-\dfrac{\partial v}{\partial z}\right) & 0 \end{bmatrix} = \begin{pmatrix} 0 & -\omega_z & \omega_y \\ \omega_z & 0 & -\omega_x \\ -\omega_y & \omega_x & 0 \end{pmatrix} \quad (2.18)$$

It is obvious that calculation of the deformation rate and rotation rate tensor for fully describing fluid motion needs the evaluation of the velocity gradient tensor. Kitzhofer et al. calculate the velocity gradient tensor via results obtained by LSM [67] without application of central difference schemes to calculate the velocity gradient tensor. A numerical as well as an experimental result for the extraction of coherent structures via results obtained by LSM is shown in figure 2.20. Figure 2.20 on top shows results of LSM applied to a simulated hill type vortex ring. The figure shows the velocity vectors in the symmetry plane x-z, 3D streamlines starting above the upstream stagnation point, and isosurfaces of the vorticity magnitude (gray) and positive (orange) and negative (blue) strain. Furthermore, some numerical results of the deformation rate and rotation rate tensor are included. The generated streamlines clearly follow the exact solution of the hill type vortex. The streamlines form a spherical shape. The velocity vectors in the symmetry plane identify the velocity distribution of a hill type vortex. No outliers are recognizable. The isosurfaces of vorticity and strain excluded from the transformation matrix derived by LSM identify the main features of the hill type vortex without any further post processing steps. The upper and lower stagnation points are highlighted. The volume elements in the upper stagnation point are compressed in z-direction and expanded in x- and y-direction ($\varepsilon_{zz}<0$, $\varepsilon_{xx}>0$, $\varepsilon_{yy}>0$). In the lower stagnation point the scene is inverted. The isosurface of the vorticity magnitude identifies the donut like vortex core. The numerical result for the rotation rate tensor in the symmetry plane x-z at the vortex core for x<0 and x>0 is given. The prefixes of the entries for vorticity ω_y agree with the physical interpretation. Figure 2.20 on bottom shows results of LSM applied to the benchmark experiment of a vortex ring. The volumetric reconstruction as well as LSM is performed by Dantec Dynamic Studio. The volumetric reconstruction bases on a multiple projective transformation of each camera view into the depth layer of the observed volume and a minstore algebraic reconstruction technique [143]. A regular grid of 278x1112x944 voxel with gray value

information is generated for each time step. LSM is applied on double frames yielding the results visualized in figure 2.20 on the bottom. The vortex ring is clearly recognizable. Beside the velocity vectors, the isosurface of vorticity magnitude is included. To point out, the vorticity magnitude is not calculated via central difference schemes, but via the parameters of the affine transformation.
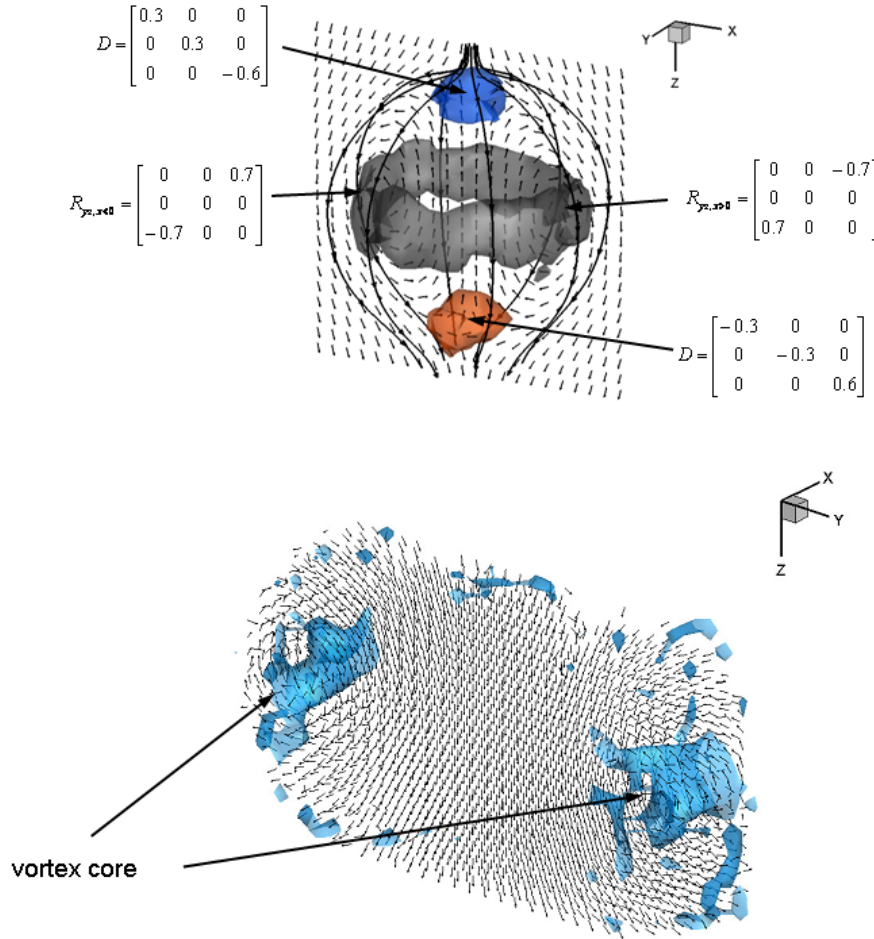
Fig 2.20 top Visualization of results obtained by LSM applied to the simulated hill type vortex ring; isosurface of vorticity magnitude (blue) identifies the donut like vortex core, isosurface of positive (red) and negative (blue) strain rates identify stagnation points; 3D streamlines show a spherical shape and the velocity vectors in the symmetry plane y-z characterize the velocity field of the hill type vortex **bottom** Experimental vortex ring: the velocity vectors have a uniform length; the blue isosurface represents the vorticity magnitude showing the vortex core

Beside the splitting into a symmetric and an anti-symmetric part, the characteristic equation of the Jacobian J can be analyzed for detection of coherent structures:

$$\lambda^3 + P \cdot \lambda^2 + Q\lambda + R = 0 \qquad (2.19)$$

The first invariant is $P = -\nabla \cdot \underline{u}$ (equivalent to zero in incompressible flows due to mass conservation). The second invariant for incompressible flow is $Q = \frac{1}{2} (\|\Omega\|^2 - \|S\|^2)$, where $\|\cdot\|$ denotes the Euclidean norm. The third invariant is $R = -\det (J)$.

Data Enhancement

Once the velocity field is generated, whether in Lagrangian or Eulerian description, it is prerequisite to enhance the derived data in a spatial as well as in a temporal manner. Experimental datasets, however, are characterized by Gaussian background noise, outliers and in worst case missing data. Before any analysis (e.g. calculation of spatial or temporal derivatives) is performed, it is crucial to detect outliers, to remove background noise and to fill up lacking regions, where erroneous vectors have been removed.

The resulting dataset in the Lagrangian frame is characterized by Lagrangian trajectories. The velocities and derivatives in the Lagrangian frame are prone to improper calculated particle positions. Lüthi et al.(2005) propose a low pass filter combined with a moving cubic spline interpolation on the position signal to smooth the dataset and to reduce uncertainties [77]. The velocities and accelerations are calculated by differentiating the cubic spline representation. Another enhancement of PTV based results is the connection of trajectories, which are separated by several time steps [150]. Here, segments of trajectories are tracked in a six-dimensional position-velocity space.

Furthermore, the Lagrangian description allows simple interpolation on the Eulerian frame [134], e.g. by adaptive Gaussian window averaging [3], polynomial interpolations [81] or inverse distance interpolation [128]. Algorithms, originally developed for 2D data enhancement in the Eulerian frame, can be adapted to 3D velocity vector fields.

In data validation or outlier detection, the important aspect is the balance between removal of spurious vectors and valid data [108]. Furthermore, an automated algorithm is required without pre-knowledge or visual inspection. Commonly applied criteria are global histogram operator [108], dynamic mean value operator [108] or normalized median test

[142]. Other methods, up to now time consuming, are cellular neural network [73] or bootstrapping [104].

The detected outliers are then replaced by median, bilinear or spline interpolations [108]. Noise reduction is achieved by ordinary smoothing using average kernels.

Another trend in data enhancement is the combination of experimental data with numerical data. More recently, Gunes and Rist (2007) [37] compare Kriging interpolation [38] with DNS-based Proper Orthogonal Decomposition (POD) mode interpolation. In case of low-resolution experimental data, DNS-based POD mode interpolation outperforms Kriging interpolation. Here, POD is applied to DNS data to extract the DNS-based POD modes. These modes are then projected onto the experimental data to obtain coefficients of the hybrid model. The experimental data is interpolated and smoothed with respect to the hybrid model. In case of high resolution PIV data, Kriging interpolation works well in eliminating noise and increasing the spatial resolution. The authors claim to use Kriging interpolation based on a Gaussian correlation function. However, afore mentioned detection criteria request a user specified input. Garcia (2010) presents an automated method without user specified input [35]. Here, outlier detection, replacement of missing data and smoothing is performed by a method called DCT-PLS. The method is based on penalized least squares approach combined with the use of the discrete cosines transform and the generalized cross-validation.

In comparison with spatial enhancement, temporal enhancement has achieved less attention. Durault et al. (2005) propose a POD-based method [30]. POD is applied on time resolved dataset to calculate temporal POD coefficients. The temporal POD coefficients are then cubic spline interpolated to enhance the temporal resolution. However, as pointed out by Bouhoubeiny and Druault (2009) the method is only valid for large scale flow structures [15]. Another approach deals with the application of the advection equation, invoking Taylor's hypothesis of frozen turbulence [117]. The authors successfully show the effectiveness of the approach increasing the temporal resolution of 3D data obtained by tomographic PIV.

2.3 3D Scanning Particle Tracking Velocimetry

The choice of a suitable volumetric measurement technique is mainly dependent on the specific experimental set-up, the flow configuration as well as on the available hardware. In case of this thesis, the flow phenomenon is tested in a rectangular water channel. Optical access is ensured from the top and from the side. The volume of interest is positioned about the symmetry plane and is sized to about B x L x H = 90 x 90 x 15 mm³ as shown in figure 2.21 The measurement volume is characterized by a high dynamic range of normalized velocity, yielding from u*≈-0.3 up to u*≈1. The free stream region has mostly constant direction, whereas the recirculation region is highly fluctuating with sudden changes of flow direction. For the volumetric flow measurement, three digital high speed cameras equipped with telecentric lenses are available. As the measurement volume is too large for holographic techniques, a technique based on geometrical optics is more appropriate. Here, classical 3D Particle Tracking Velocimetry is the most convenient technique. This is for the following reasons:

a) highly turbulent flow with large spatial and temporal gradients
b) Lagrangian and Eulerian information is desired
c) high particle seeding densities are critical to achieve in the set-up
d) comparative low processing cost

Large spatial and temporal velocity gradients are critical to PIV based algorithms like CC or LSM, because of significant changes in intensity distributions due to turbulent displacements of particles in the inner of interrogation areas. A solution to reduce these gradients is a decrease of the separation time to yield smaller displacements between the frames for the cost of reduced dynamic bandwidth.

A rather strong advantage of 3D PTV is the availability of the Lagrangian and of the Eulerian velocity field. The condition is a high spatial resolution in the Lagrangian frame, which is defined by the number of tracked particles. Furthermore, high-speed recording allows the evaluation of long Lagrangian trajectories, giving rise to the calculation of Lagrangian accelerations [88].

The direct calculation of the Eulerian velocity field via CC or LSM needs high particle densities. A defined number of gray-value voxel information is necessary for a good estimation of the local velocities. This is not possible in the present test case. The total volume of the channel is too large for constant seeding. Furthermore, the volume of

interest is surrounded by fluid. If the channel volume is homogeneously seeded, the multiple scatter along the path to the volume of interest results in a low contrast image of the volume of interest.
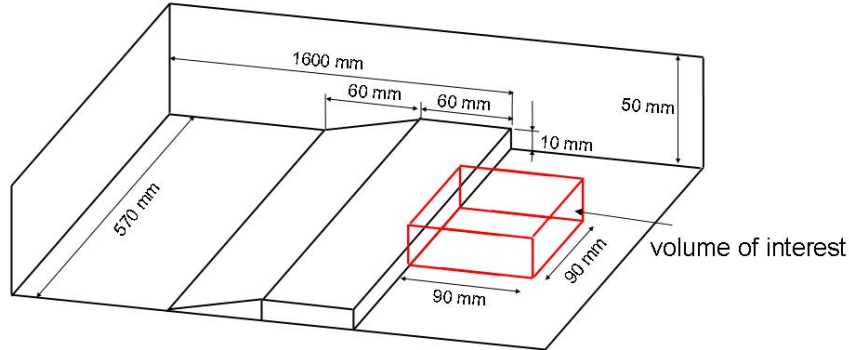
Fig 2.21 Volume of interest and physical dimensions of the experimental set-up

As mentioned above, the spatial resolution in classical 3D PTV is limited to about 0.005 ppp using pointwise reconstruction. The particle density can be increased, on the one hand by the chosen method (volumetric or pointwise) and on the other hand by a clever choice of illumination. Hoyer et al. (2005) choose a scanning illumination for classical Particle Tracking Velocimetry [48]. The authors show an increase of the number particle density compared to classical PTV. The implementation of a scanning illumination connected with high-speed recording is demonstrated by Kitzhofer et al. (2009) [66]. The number particle density is increased by a factor proportional to the number of generated light sheets. This is due to simplifications in identification of homologous particles and due to simplifications in tracking single particles.

In the following, the implementation of 3D Scanning Particle Tracking Velocimetry is described. The first part describes the experimental set-up and the boundary conditions of the set-up. The recording system consists of digital high speed cameras equipped with telecentric lenses. The illuminating system consists of a scanning device. Thus, assumptions and simplifications of both will be pointed out in detail. The second part describes algorithmic developments regarding the measurement technique to calculate the Lagrangian as well as the Eulerian velocity field. The developed algorithm is called hybrid PIV/PTV 4-frame method.

2.3.1 Experimental set-up

An iso-view of the experimental set-up is shown in figure 2.22. The laser beam of a continuous Argon-Ion laser (8) (Coherent Innova 70, 2 W) passes an optical lens system (9) to adjust the desired thickness of the light sheets. A rotating mirror drum (7) reflects the laser beam into the direction of the measurement volume and generates successively 4 parallel light sheet planes (4). The particle images are recorded with an imaging system consisting of three digital high-speed cameras (Photron APX RS) (3) and telecentric lenses (Sill Optics)(2). The three camera system is installed above the water channel with an angular displacement of about 0°, 45°, -45°. The f-number of the lenses is adjusted to f# = 16 to reach a sufficient depth of focus. A water filled prism reduces astigmatism in the image planes (3). The side of the water channel (10) opposite to the entrance side of the laser is covered with a light absorbing mat that reduces stray reflections, thus giving a black background. The neutrally buoyant seeding particles (6) of roughly 100 μm are injected upstream of the BFS with respect to [11].
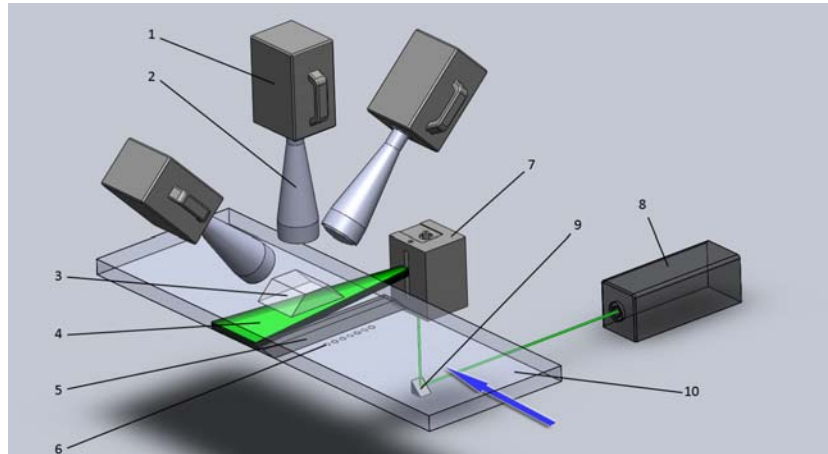
Fig 2.22 Experimental set-up of backward facing step flow: 1) high speed cameras (3000 fps) 2) telecentric lenses 3) water filled prism 4) voluminous illumination 5) backward facing step 6) seeding injection 7) mirror drum 8) Ar-Ion laser 9) tilted mirror 10) turbulent water channel at Re_h=4440, ER=1.25, AR=57

High speed cameras Photron APX RS (1024x1024 pix, 3000fps, 2GB storage) are installed above the channel in the arrangement shown in figure 2.22. The cameras record the scene with 1000 fps allowing time resolved measurement of the BFSF.

As the cameras are installed outside the channel, the optical rays pass through varying indices of refraction. By assumption of thin (2mm) glass walls of the water tunnel, the optical rays pass through water and air. For minimizing optical refraction in the outer cameras, a water filled prism is installed above the tunnel (wall thickness 1mm). Thus, all

optical rays enter perpendicular into the boundary surface between water and air. Furthermore, the water filled prism reduces optical aberrations resulting from the installation with an inclined angle. Figure 2.23 shows the influence of the water filled prism on the optical path and on the quality of the particle images.
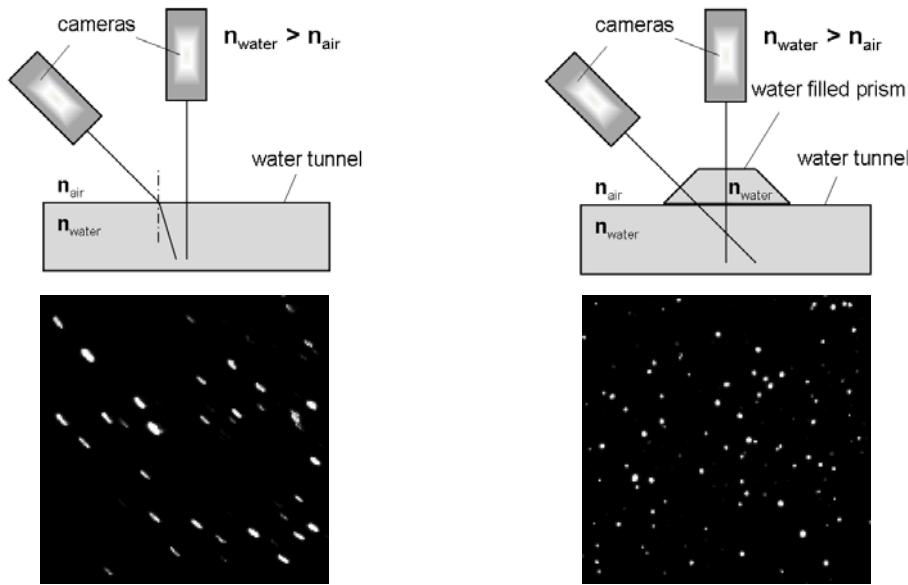
Fig 2.23 Influence of the water filled prism on the quality of particle images. Left image shows distorted particles. Right image shows regular shaped particles due to the installation of the water filled prism.

Imaging system

The characteristics of *telecentric lenses* and the resulting parallel projection are well known and discussed in detail in e.g. Schreer (2005) [125]. This section summarizes the main points for understanding the application of telecentric imaging in the course of three-dimensional reconstruction. The telecentric lenses used in this application are telecentric in object space. The advantages of using telecentric lenses are a constant magnification over the whole depth of field, high accuracy and negligible optical distortions.

In perspective transformations the focal point has a defined distance to the image plane. This results in a variable magnification in the object space. In case of telecentric imaging the distance between focal point and image plane is at infinity resulting in an approximately parallel projection in the object space within the range of telecentry and consequently in a constant magnification as sketched in figure 2.24. The constant magnification yields a defined measurement volume. It is defined by the width and the height of the image plane, the magnification of the lenses system and by the depth of focus. The measured distortions are less than 0.1 % of the image diagonal in the outer image

areas making nonlinear lens distortions negligible [66]. The telecentric range with deviations of less than 0.1% has been evaluated with the given lenses to be about 90 mm with a scaling factor of 11.4 ± 0.02 Pix/mm at an f# = 16. This is equivalent to a magnification M = 0.2.
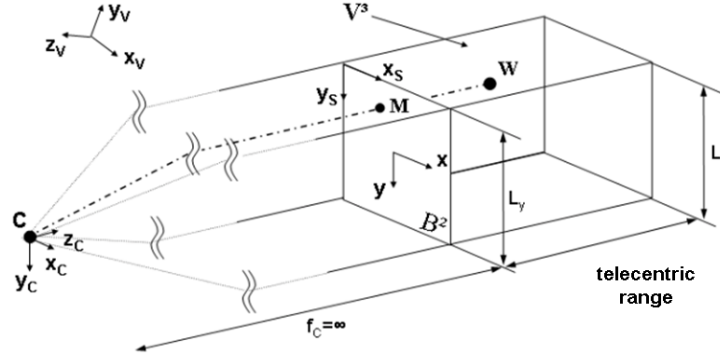
Fig 2.24 Parallel projection due to telecentric imaging

In parallel projection, the focal point is at infinity. This results in several simplifications in the mathematical description of the projection from object space to image plane. The simplification in the extern transformation is the loss of depth information, resulting in $t_z=0$ (equation 2.3). The extern transformation matrix results in:

$$D_{orth} = \begin{bmatrix} r_{11} & r_{12} & r_{13} & t_x \\ r_{21} & r_{22} & r_{23} & t_y \\ r_{31} & r_{32} & r_{33} & 0 \\ 0 & 0 & 0 & 1 \end{bmatrix} \qquad (2.20)$$

The perspective transformation is simplified due to the transition from intercept theorem to the orthographic equation of projection:

$$x_S = x_c, y_S = y_c. \qquad (2.21)$$

The perspective transformation matrix results in:

$$P'_{orth} = \begin{bmatrix} 1 & 0 & 0 & 0 \\ 0 & 1 & 0 & 0 \\ 0 & 0 & 0 & 1 \end{bmatrix} \qquad (2.22)$$

Finally, the scaling parameter in the internal transformation is identical in x- and y-direction for parallel projection. The internal transformation matrix for parallel projection reads:

$$A_{orth} = \begin{bmatrix} k_s & 0 & x_{s0} \\ 0 & k_s & y_{s0} \\ 0 & 0 & 1 \end{bmatrix} \tag{2.23}$$

Thus, the complete projection matrix for parallel projection results in:

$$P_{orth} = A_{orth} \cdot P'_{ortzh} \cdot D_{orth} = \begin{bmatrix} k_s \cdot r_{11} & k_s \cdot r_{12} & k_s \cdot r_{13} & k_s \cdot t_x + x_0 \\ k_s \cdot r_{21} & k_s \cdot r_{22} & k_s \cdot r_{23} & k_s \cdot t_y + y_0 \\ 0 & 0 & 0 & 1 \end{bmatrix} \tag{2.24}$$

The simplified projection matrix results in massive reduction of steps in the calculation of a three-dimensional position. By consideration of p_{31}=0, p_{32}=0 and p_{33}=0 due to the orthographic projection, equation 2.8 is simplified to:

$$E_{orth} X_W = \begin{bmatrix} p_1^{11} & p_1^{12} & p_1^{13} & p_1^{14} - x_1 \\ p_1^{21} & p_1^{22} & p_1^{23} & p_1^{24} - y_1 \\ p_2^{11} & p_2^{12} & p_2^{13} & p_2^{14} - x_2 \\ p_2^{21} & p_2^{22} & p_2^{23} & p_2^{24} - y_2 \end{bmatrix} \begin{bmatrix} X_w \\ Y_w \\ Z_w \\ 1 \end{bmatrix} = 0 \tag{2.25}$$

The decomposition of E_{orth} into constant B_{orth} and variable, but simplified c_{orth} results in:

$$B_{orth} = \begin{bmatrix} e_{11} & e_{12} & e_{13} \\ e_{21} & e_{22} & e_{23} \\ e_{31} & e_{32} & e_{33} \\ e_{41} & e_{42} & e_{43} \end{bmatrix} = const \text{ and } c_{orth} = \begin{bmatrix} e_{14} \\ e_{24} \\ e_{34} \\ e_{44} \end{bmatrix} \tag{2.26}$$

A comparison of equation 2.8 and 2.23 shows the reduction in the number of steps for calculation of a single three-dimensional point. In total, fifteen steps for calculation are saved due to telecentric imaging in comparison to divergent lensens.

The *calibration* of the imaging system, i.e. the estimation of the projection and fundamental matrix is done via a planar target at two positions in the volume of interest. The target consists of 1369 black dots and a white background guaranteeing high contrast, see figure 2.25. Visible by all cameras are 832 markers (overlapping area). Thus, a total amount of 1664 markers are available for calibration.

The two dimensional image coordinates of the markers are calculated and compared with the known tree-dimensional positions for the estimation of the projection matrix of the single cameras. The observations result in systems of equations in the following form:

$$s \cdot \begin{bmatrix} x \\ y \\ 1 \end{bmatrix} = Q \cdot \begin{bmatrix} x_w \\ y_w \\ z_w \\ 1 \end{bmatrix}, \qquad \text{with } Q = \begin{bmatrix} q_{11} & q_{12} & q_{13} & q_{14} \\ q_{21} & q_{22} & q_{23} & q_{24} \\ q_{31} & q_{32} & q_{33} & q_{34} \\ q_{41} & q_{42} & q_{43} & q_{44} \end{bmatrix} \qquad (2.27)$$

For a number of N observations, 2N homogeneous linear equations will result. A comparison between equation 2.22 and 2.25 directly yields $q_{41,42,43}=0$ and $q_{44}=1$. The remaining parameters are estimated by a classical non-linear Gauss-Newton method. The first guess of the parameters is calculated by singular value decomposition.

The influence of the number of control points on the absolute deviation of the projection is shown in figure 2.25. The absolute deviation is the mean value of the difference between the re-projected and the recorded two-dimensional positions of the markers. Above a number of about 20 control points, no more increase in accuracy is expected. Nevertheless, to yield a homogeneous and high quality solution in the total volume, 1000 homogeneously distributed calibration points are considered. The remaining points are considered for the estimation of the achieved accuracy. The median deviation for the estimated projection matrixs ranges from 0.21 pix up to 0.28 pix, which is summarized in table 2.2.

The fundamental matrix is calculated via the 8-point algorithm expanded by the Frobenius-norm [125], which needs 8 homologous 2D positions. The mean deviation, which is defined as the shortest distance between the two-dimensional marker position and the epipolar line, is calculated to be in between 0.15 and 0.2 pix.
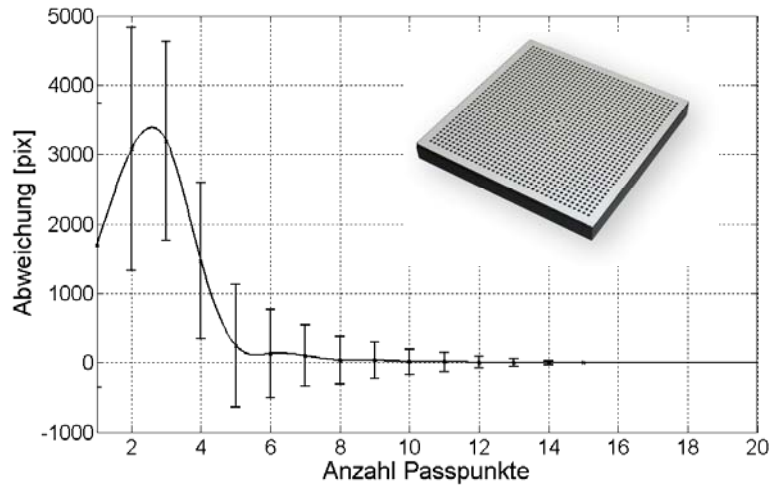
Fig 2.25 Influence of the number of calibration points on the median deviation in projection

Calibration	Deviation [pix]
Fundamental matrix camera 2-1	0.17
Fundamental matrix camera 2-3	0.20
Fundamental matrix camera 1-3	0.15
Projection matrix camera 1	0.23
Projection matrix camera 2	0.28
Projection matrix camera 3	0.21

Table 2.2 Mean accuracy of multi-camera calibration

The *accuracy* of the imaging system in the estimation of a three-dimensional position is validated two-fold. On the one hand, calculated three-dimensional marker positions are compared with known values. On the other hand, theoretically deviation in the three-dimensional positions due to erroneously calculated 2D positions of particles are considered.

The 3D reconstruction of the marker positions via equation 2.11 showed a systematical deviation of the reconstructed position. The deviation is calculated in the following manner: Homologous control point images used for the estimation of the projection matrixs are reconstructed via equation 2.11 in physical space. The reconstructed positions are compared with the known values, delivering a deviation in each spatial direction $\Delta_{3D,x}$ $\Delta_{3D,y}$ $\Delta_{3D,z}$ [mm] in a certain point (x,y,z) in physical space. Figure 2.26 shows the magnitude Δ_{3D} of all directional deviations averaged over the z-direction. The deviations range from 0.2 mm to 0.5 mm. The reasons for the deviation are manifold, but main

influences are seen in the separation planes between prism and water tunnel and in the not perfectly planar planes of the prism. The single deviations are then used as nodes to linearly interpolate onto a "deviation space". Figure 2.26 on the right shows a single vector slice through the deviation space at z/h=0.8. Vectors show the structured deviation in a plane at z/h=8 parallel to the bottom wall. The deviation space is used to remove the observed systematic deviation from the measurement results and to increase the accuracy. The accuracy is estimated by quality check of the marker positions, which are not used for the calibration procedure after post-processing via the deviation space. The $RMS_{mm,cal}$ value resulting from the calibration evaluates to $RMS_{mm,cal} = 0.014$ mm, which corresponds to $RMS_{pix,cal} \approx 0.16$ pix.
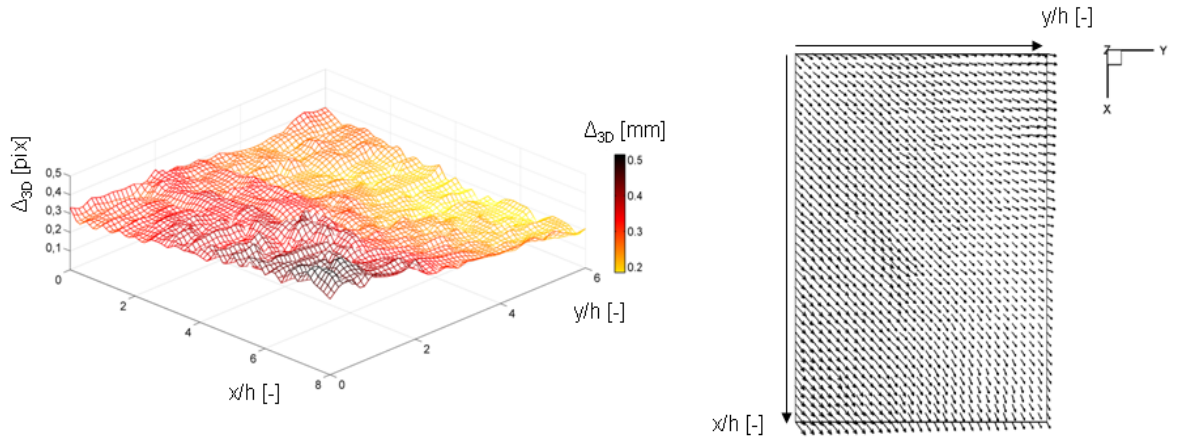
Fig 2.26 (left) Magnitude of deviation [mm] between reconstructed and known three-dimensional positions; **(right)** direction of deviation at z/h=8 parallel to the bottom wall

The influence of erroneous calculated positions of 2D particle images on the calculation of a 3D position shows figure 2.27. As basic for the estimation of deviation in three-dimensional positions due to erroneously calculated 2D positions of a particle image is the theoretically calculated deviation from table 2.1. All particle positions in this thesis are calculated by the gray-value weighted center of area, resulting in a theortical deviation of 0.02 pix. The worst case $RMS_{mm,2D}$ value resulting from the detection of single particle positions is calculated to $RMS_{mm,2D} = 0.007$ mm from a theoretical point of view. In total, the measurement uncertainty is estimated to $RMS_{mm} = RMS_{mm,cal} + RMS_{mm,2D} = 0.021$ mm, which corresponds to $RMS_{pix} \approx 0.2$ pix.
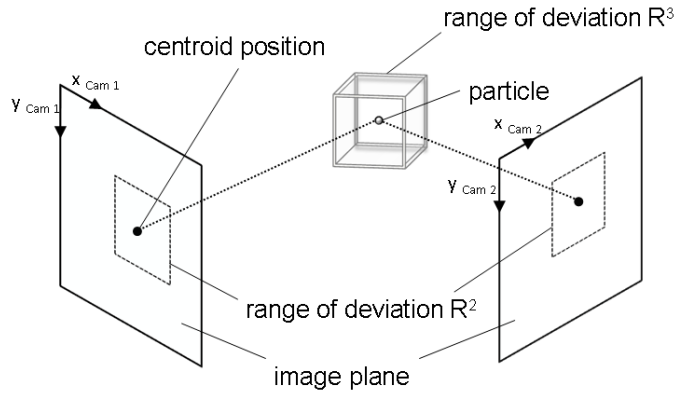
Fig 2.27 Influence of the deviation in estimated two-dimensional centroid position of a particle image on the three-dimensional deviation

Volumetric illumination

Volumetric illumination is mandatory in 3D Particle Tracking Velocimetry. Primarily, the illumination directly affects the quality of the particle images. In 3D PTV, a particle image with high-contrast is preferable, as single particle detection schemes are applied. For that purpose, a scanning illumination device is applied, i.e. the mirror drum presented by Brücker (1996) [17]. The principal of the technique is shown in figure 2.28. A continuous laser beam is reflected on a 45° tilted mirror, which is installed on a drum. Due to the rotation of the drum, the laser beam is deflected and sweeps through the volume, generating a kinematic light sheet. The cameras are synchronized to record the scene during the time interval of one complete sweep of the laser beam. In this manner, the camera integrates the scattered light of the beam during one scan and only records the illuminated plane. In total, a number of twenty mirrors are installed on the circumferential of the drum allowing a total amount of twenty light sheets.
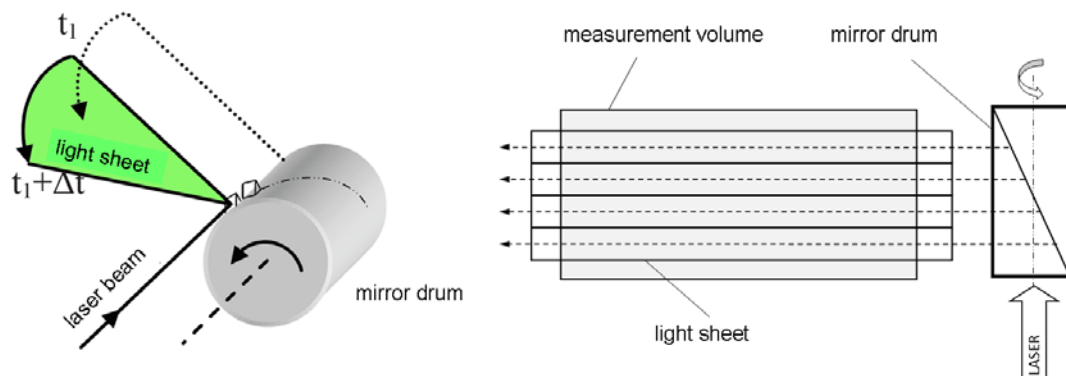
Fig 2.28 Principle of the rotating mirror drum **(left)** iso view **(right)** top view

The positions of the mirrors are variable allowing the adjustment of the number light sheets and of the position of the light sheets. The thickness is adjustable by changing the laser beam thickness. The arrangement of the mirrors on the drum defines the recording mode. Here, double imaging or time resolved imaging is possible. In this thesis, time resolved measurements are performed. Thus, the mirrors are installed in an arrangement to generate light sheets in a way that is sketched in figure 2.29. Four light sheets with a thickness of 5mm are generated. The mirrors are installed to yield an overlap of the light sheets of roughly 1.5mm. This results in a thickness of 15.5mm of the illuminated volume. Furthermore, the sketch shows the scanning direction, from the top to the bottom. The separation time between the single light sheets is 1ms, resulting in separation time of 4 ms for a homologous light sheet. The separation time is chosen with respect to particle displacement and intensity of the particle images. A compromise is chosen between short separation times for small particle displacements and long separation times for high intensity particle images. The camera is recording with the same frequency of 1000 Hz as the sweep frequency of the laser beam.
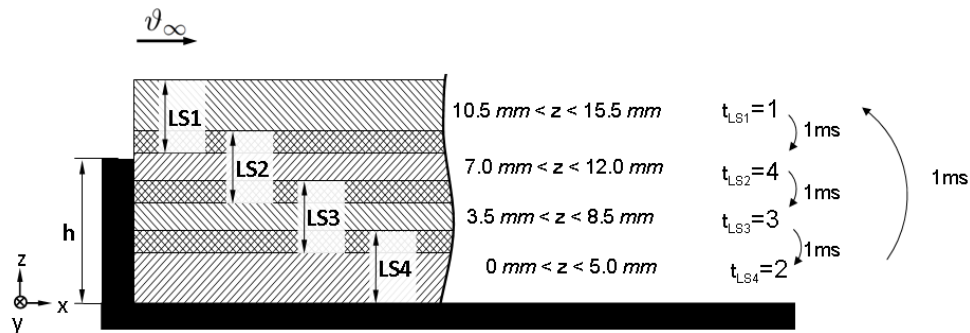
Fig 2.29 Positions of light sheets in the side view

The quality of the recorded particle images is shown in figure 2.30 by means of a representative particle image. One exemplary image section is shown in a three-dimensional plot. The image section shows two particles surrounded by background noise. The chosen image section is exemplary for all recorded images. The images are characterized by homogeneous gray-value distribution and a median background noise of roughly 2 out of 255. Thus, a global threshold of 5 is chosen for segmentation.
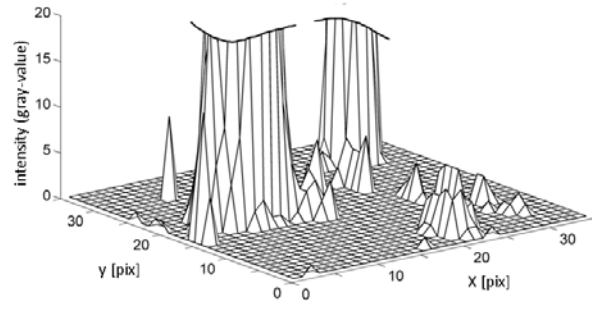
Fig 2.30 Intensity distribution of an exemplarily chosen image section. The image shows two particles surrounded by a low level background noise giving evidence to the quality of illumination.

Beside the high quality illumination, the scanning illumination results in a higher number particle density traceable with PTV. This is for two reasons: First, the slicing of the volume results in a smaller number of projected particles compared to a full volume illumination. This is shown in figure 2.31. The left figure shows a synthetically generated volume filled with particles. The volumetric particles with a Gaussian intensity distribution are represented by dots and fill up the whole volume. The corresponding parallel projection of the particles is shown in the sub-image. Here, no single particles can be detected due to a high number particle density, which results in an enormous overlap of particle images. The figure on the right shows the same particle distribution, but only a sub-volume is illuminated. In the corresponding parallel projection, single particles are detectable, allowing 3D PTV. Furthermore, the decrease of particles per pixel (ppp) in the image plane reduces the difficulty in tracking single particles, see figure 2.15. The scanning illumination results in simplifications of identifying single particles and in simplification of the tracking procedure, as the difficulty in tracking (equation 2.13) decreases.
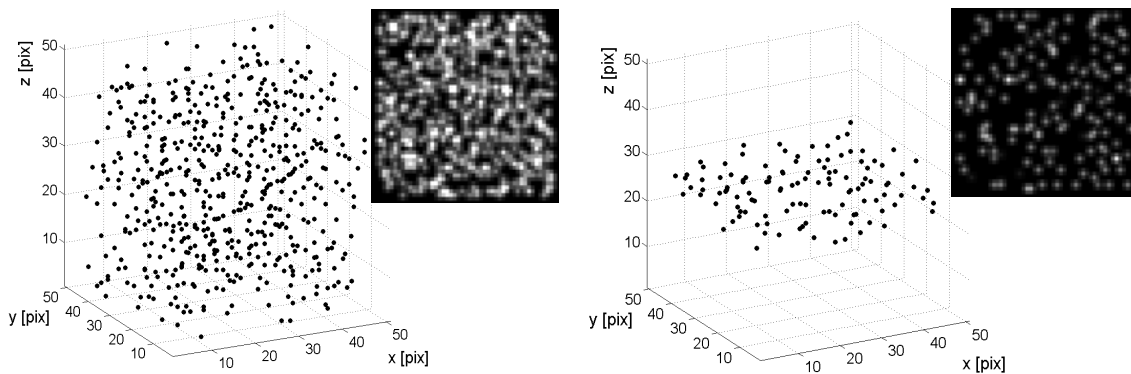
Fig 2.31 Synthetic generated volume filled with particles. The figure on the left represents a full volume illumination and the figure on the right a sub-volume illumination as evident in scanning illumination.

The second reason for a higher number particle density traceable with 3D Scanning PTV is the reduction of the search area along the epipolar line for finding homologous particles, see figure 2.32. A particle in the image plane of one camera is along the corresponding epipolar line in the second image plane. Here, the slicing of the volume results in a further reduction of the search area along the epipolar line. The length of the search area is dependent on the thickness of the sub-volume and on the angle between light sheet and image planes. The reduction of the epipolar line results in considerable reduction of ambiguities in finding homologous particles.
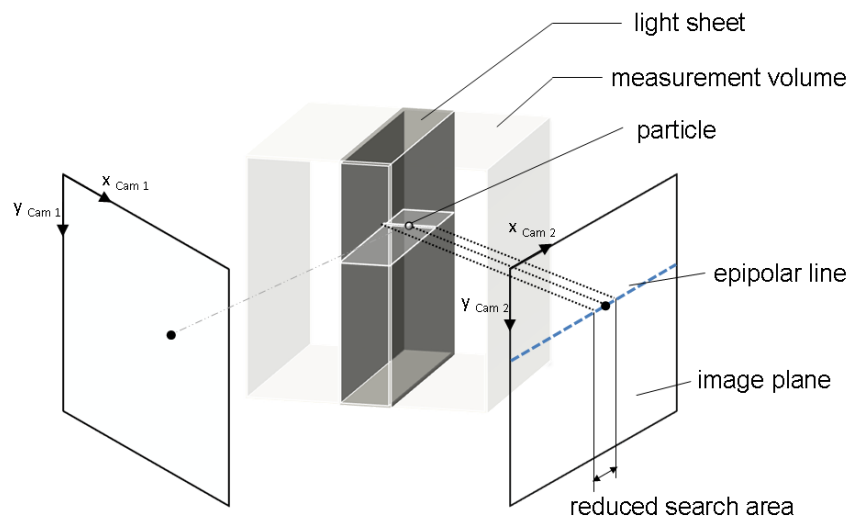
Fig 2.32 Reduction of the search area along the epipolar line due to slicing of the volume

To summarize, the scanning illumination is applied for the following reasons:
- the quality of the particle images is high, allowing efficient detection of particles
- the volume is sliced, resulting in a higher spatial resolution, which is limited by overlapping particle images
- the correspondence problem in finding homologous particles via the epipolar geometry is diminished
- the difficulty in tracking decreases.

2.3.2 Tracking Algorithm and Point Reconstruction

In the following, the implemented algorithm for 3D Scanning Particle Tracking Velocimetry is described. The algorithm is a hybrid PIV/PTV 4-frame method. *Hybrid PIV/PTV* means that the first guess in which direction a particle has moved is estimated via cross correlation in an interrogation area. *4-frame* means that if a particle has been tracked for several time steps, the next position is estimated via the kinematic history of the particle.

Basically, tracking algorithms are discriminated in three approaches [105]:

a) tracking in image plane (2D)

b) tracking in object space (3D)

c) combination of a) and b)

In this thesis, approach c) is chosen. The tracking of particles is first performed in one image plane and afterwards performed in object space for reduction of ambiguities. For that purpose, a large amount of methods are described in literature. The methods calculate quality criteria, which are defined manifold: gray value distribution, shape, position, size, probability or kinematic conditions, to mention only a few. Nevertheless, common in all methods is the definition of a search area, where a particle is expected in the next frame. The proper choice of a search area is crucial in PTV algorithms for the reduction of ambiguities.

Search area

The choice of the search area depends on the temporal length t_L of a trajectory. A trajectory with $t_L=1$ is a single particle (case 1) and a trajectory with $t_L=5$ is a particle, which is tracked for 5 time steps (case 2). It is obvious that the proper estimation of expected position in the next frame is more precise in the latter case.

Case 1 occurs at the beginning of processing or if a particle enters the measurement volume. If no pre-information of the velocity field is available, a proper choice of the search area is not possible. Thus, it is mandatory to estimate the center of the search area via the maximum particle displacement. If a pre-information is available, e.g. local mean flow direction, the choice of a search area is getting more precise. One possibility for the estimation is the application of correlation based methods. The local mean velocity is first estimated by PIV to define the location of the search area. A necessary condition is a high particle density, which is prerequisite for correlation. Then, single particle positions are tracked. The method is successful, if the depth extension of the volume is not too large. At

high spatial gradients, a large depth extension will result in erroneous estimated search areas and consequently erroneous trajectories. In this thesis, the depth direction is decreased by the scanning illumination, allowing the estimation of the search area via correlation. This is due to the reduction of the dynamical range of velocities in the single sub-volumes.

Case 2 occurs if a single particle could be tracked for several time steps, as shown in figure 2.33. If a particle is tracked for at least two time steps, the center of the search area is calculated by the length and the direction of the velocity vector. The diameter of the search area is chosen to be 6 pix.
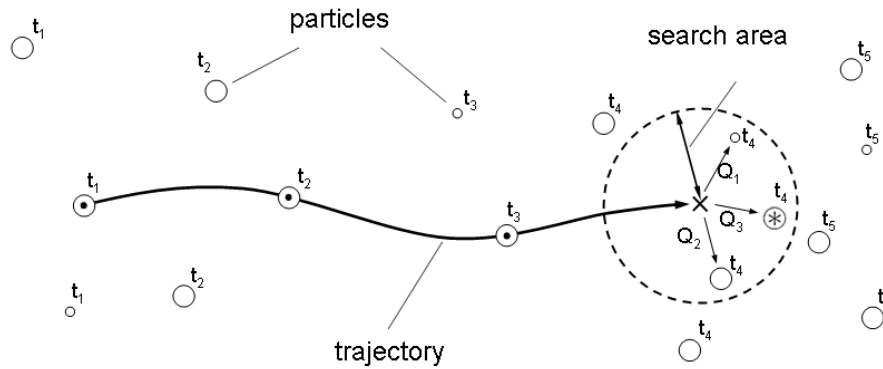
Fig 2.33 Schematic of two-dimensional tracking; definition of search area for case 2

Tracking

All particles inside the search area are possible candidates for the trajectory (ambiguities). A choice is made by consideration of the kinematic history of the trajectory, namely the 4-frame method [82]. The aim of the method is the evaluation of a quality criterion for each possible connection of a particle from one time step to the other. The results are quality values of evaluated trajectories. The one with the smallest quality value is chosen to be the correct path.

The algorithms used herein are classified into the temporal length of a particle path. If a particle path has no history, it is unavoidable to use the nearest neighbour criterion. The quality function for the nearest neighbour criterion $\Phi_{ij,\,NN}$ reads to:

$$\Phi_{ij,\mathrm{NN}}^{t} = \left\| x_{j}^{t+1} - x_{i}^{t} \right\| \tag{2.28}$$

If a trajectory is observed for two time steps, the three frame method is chosen. The prediction of the particle position in the next time step is estimated due to the velocity of

the particle resulting from the two defined positions. The quality function for minimum acceleration $\Phi_{ij,3}$ reads to:

$$\Phi_{ij,3}^{t} = \frac{\left\| x_j^{t+1} - 2x_i^t + x_i^{t-1} \right\|}{2\Delta t^2} \tag{2.29}$$

If a trajectory is observed for more than two time steps, the four frame method is chosen. The prediction of the particle position in the following time step is estimated due to the velocity of the particle resulting from the two last defined positions and due to the acceleration of the particle calculated from the four time steps. It is assumed that the particle moves locally with a minimum change in acceleration, thus one can define a quality factor $\Phi_{ij,4}$, which determines the probability of a correct particle path:

$$\Phi_{ij,4}^{t} = \frac{1}{2\Delta t^2} \left(\left\| x_j^{t+2} - 2x_i^{t+1} + x_i^t \right\| - \left\| x_j^{t+1} - 2x_i^t + x_i^{t-1} \right\| \right) \tag{2.30}$$

In the case of conflicts occurring from the quality criteria, other criteria have to be defined. A conflict occurs, if the quality function for two possible candidates is equal in the range of tolerance. Thus, a second criterion is used, which identifies corresponding particle images in the successive time steps because of the number of occupied pixel. The particle with the smallest change in image size is chosen as the most probable candidate. The quality function reads to:

$$\Phi_{ij,size}^{t} = \left\| N_{ij}^{t+1} - N_{ij}^t \right\| \tag{2.31}$$

If this criterion provides no solution, finally the intensity distribution of the possible candidates is compared with the intensity distribution of the particle already being part of the trajectory. The one with the best fit is chosen.

Exemplary results of the two-dimensional tracking procedure in each of the recorded planes are shown in figure 2.34 by means of calculated trajectories. In total, a sequence of 60 time steps is shown. Trajectories are plotted having at least a temporal length of 30 time steps. The different flow states (dependent on the distance from the bottom wall) are clearly recognizable: regular direction in the upper fat light sheet and increasing irregular directions with decreasing distance to the bottom wall.
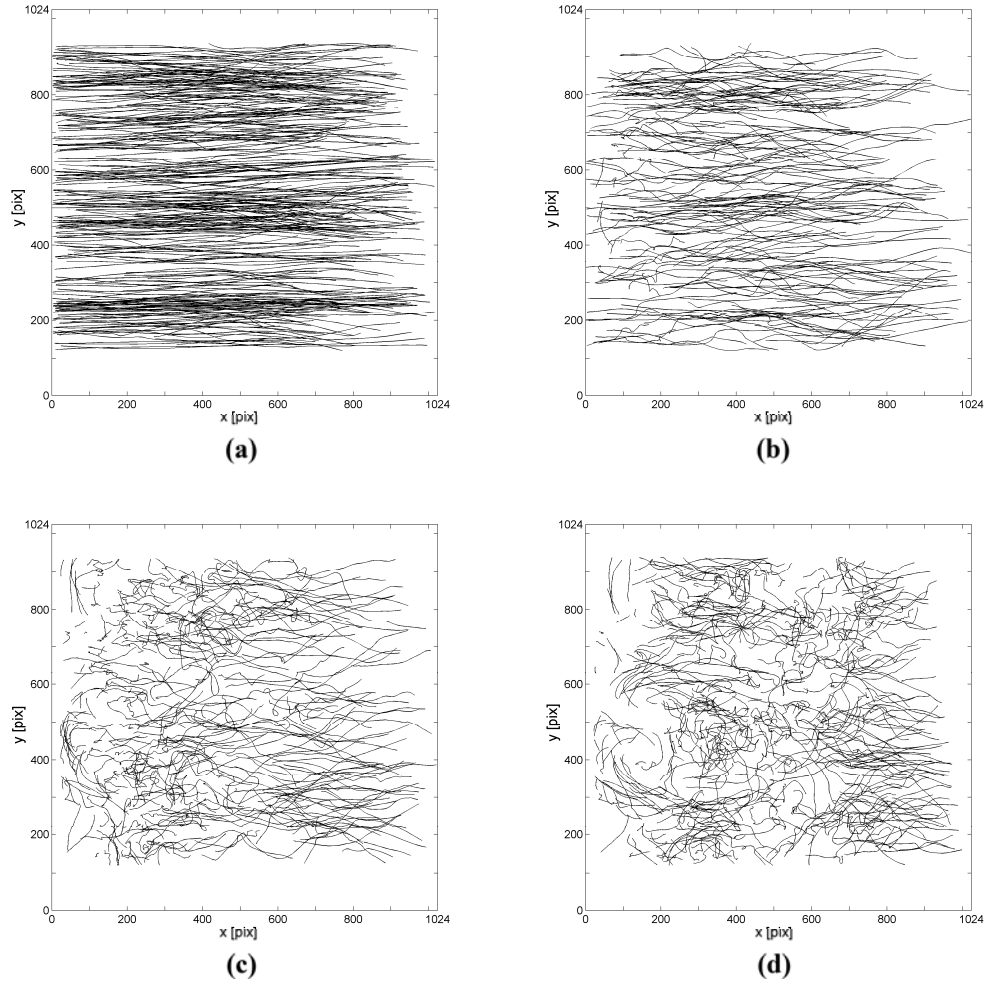
Fig 2.34 2D trajectories of light sheet 1 (a) to light sheet 4 (d) tracked for at least 30 time steps in a sequence of 60 time steps

3D Reconstruction

The 3D reconstruction is performed for each two-dimensional trajectory following equation 2.11. For a given two-dimensional trajectory, homologous particles are searched in the other image planes. For that purpose, the epipolar geometry is applied. The tolerance around the epipolar line is chosen to be 0.5 pix with respect to table 2.1. Possible candidates are then reconstructed in three-dimensional space and chosen to be part of the trajectory following the quality criteria similar to the pre-described two-dimensional case.

All particle positions along the trajectory, which can unambiguously be identified, are chosen to be part of the three-dimensional trajectory. The remaining points are studied in a spatio-temporal manner. Here, the temporal length of the pieces of the trajectory characterizes the quality function, nearest neighbour, 3-frame and 4-frame quality function. The three-dimensional position with the smallest deviation from the calculated position is chosen. If the deviation is higher than a certain threshold, the 3D position is not

reconstructed resulting in a gap in the trajectory. If a candidate is identified to be part of the trajectory, the three-dimensional point is reconstructed and the corresponding two-dimensional image points are deleted from the database. This is repeated for each two-dimensional trajectory resulting in a dataset consisting of three-dimensional trajectories for each light-sheet.

In total, 13 experimental recordings of the BFSF are processed, yielding 13 Lagrangian velocity fields, each 2s in physical time (2000 time steps). A mean number vector density is calculated to about 42 vectors/cm³. Nevertheless, it should be noted that there is a distinct decrease in number vector density from LS1 to LS4. This is due to difficulties in bringing particles to the wall, which manifests in a lower local seeding density in LS1 in comparison to LS4. The particle displacements vary largely in the single light sheets having displacements of 20 pix in the upper light sheets and 1-2 pix in the step corner of the lower light sheets. Thus, the difficulty in tracking varies largely. The planar number particle density is calculated to 0.005 particles/pix, resulting in a difficulty in tracking e=1.25 (see figure 2.15). The yield (number of 2D centroid positions/number of three-dimensional vectors) is estimated via the mean number of linked particles with respect to the center camera to 58%.

2.3.3 Post Processing

The post-processing includes the manipulation of the raw trajectories and the extraction of fluid-mechanical parameters thereafter. The manipulation of the raw data is the connecting and smoothing of trajectories and the calculation of velocities and accelerations from the smoothed particle path.

The *connection* of trajectories is for two reasons:

- gaps in the evaluated three-dimensional trajectories and
- use of the scanning illumination and therefore overlapping trajectories.

Gaps occur due to the "drop out" behaviour of particles and from ambiguities. The "drop out" behaviour of particles is the disappearance of single particles in one of the image planes resulting in lacks in the three-dimensional trajectory [150] as shown in figure 2.35. The disappearance results from inhomogeneous illumination, angle-dependent illumination or simply image noise, which is strongly reduced due to the scanning illumination, see figure 2.30. Nevertheless, gaps due to ambiguities still exist. Usually, segments of trajectories need to be identified to be part of the same trajectory. Xu (2008) [150]

proposed a "tracking in six dimensions" for the connection of segments of trajectories in object space. The main idea is the extension of tracking single particles to the tracking of segments of trajectories. Beside the information of position and time, the information of velocities and accelerations is used. In our case, segments of trajectories are already identified to be part of the same trajectory due to the calculated two-dimensional trajectory.
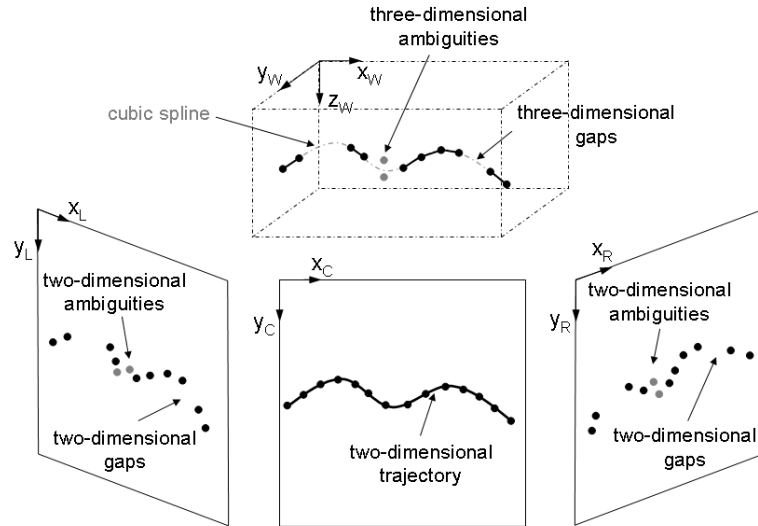
Fig 2.35 Schematic of gaps and ambiguities in the proposed PTV algorithm

The identification of homologous trajectories between the light sheets is possible due to the overlapping light sheets. This is done via a simple nearest neighbour criterion in object space as the separation time between the single light sheets is small (1ms) resulting in small particle displacements. Figure 2.36 shows an exemplarily chosen trajectory tracked over all light sheet volumes. Furthermore, one overlapping area within two successive light sheets is shown in the magnification. Due to the scanning illumination, the particle positions need to be corrected to represent the same instant in time with equal separation times [48].
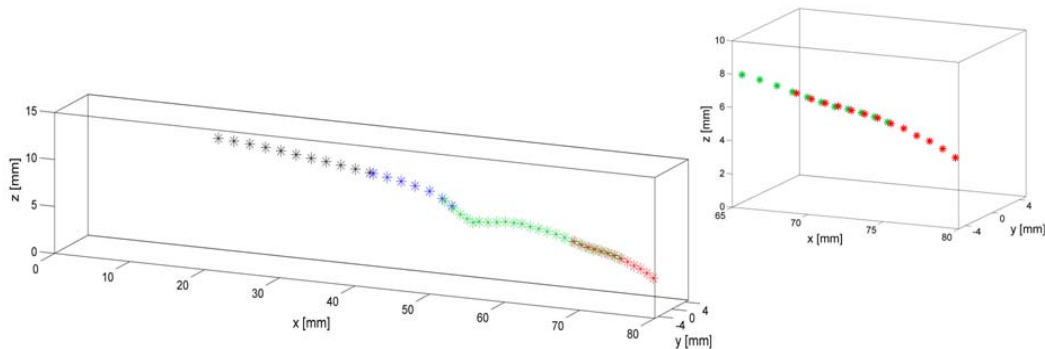
Fig 2.36 Three-dimensional trajectory tracked over all light sheets (black: LS1; blue: LS2, green: LS3; red: LS4). The magnification shows the overlapping area of LS3 and LS4.

The connection of the trajectories due to gaps, ambiguities or scanning illumination is performed via moving cubic spline interpolation with respect to Lüthi et al. (2005) [77]. The authors correct the three-dimensional positions of particles resulting from uncertainty in measurement. For that purpose, a moving cubic spline interpolation is applied.

$$x_i(t) = c_{i,0} + c_{i,1}t + c_{i,2}t^2 + c_{i,3}t^3 \qquad (2.32)$$

The coefficients $c_{i,j}$ are calculated piece-wise on the trajectory with a number of supporting points depending on the length of a trajectory. The minimum number is set to 6 supporting points and the maximum is set to 21. This results in an over estimated system of at least 6 equations or a maximum of 21 equations for 4 coefficients. In this manner, the new positions are evaluated for a separation time of 1ms. The enhancement is shown in figure 2.37 for the exemplarily calculated trajectory from figure 2.36. The first and second derivative of equation 2.30 results in the velocity and acceleration of the trajectory.
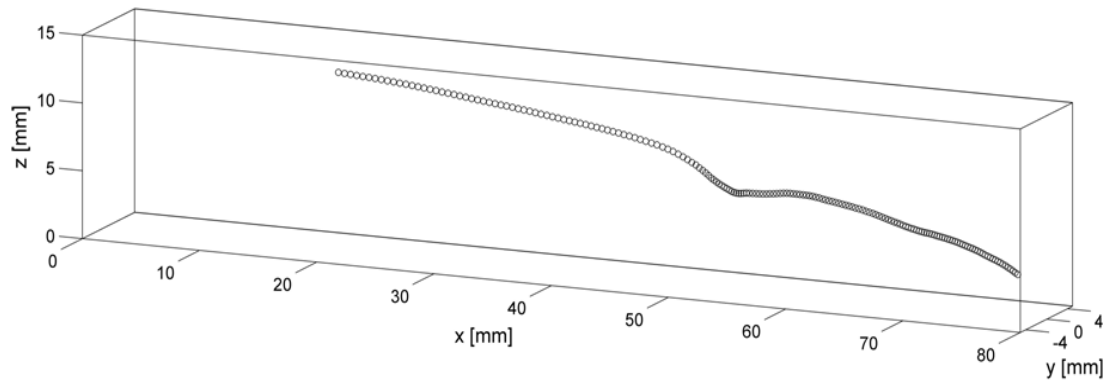
Fig 2.37 Enhanced trajectory: moving cubic spline interpolation with piece-wise 21 supporting points

A time sequence of 200 ms is shown in figure 2.38 with particles tracked for at least 150 time steps. The BFSF is clearly recognizable. The trajectories are colour-coded with normalized streamwise velocity. The region of shear layer roll up, development and impinging, as well as the recirculation region and the redeveloping boundary layer is recorded by the imaging system. A median number of 42 particles/cm³ are reconstructed.
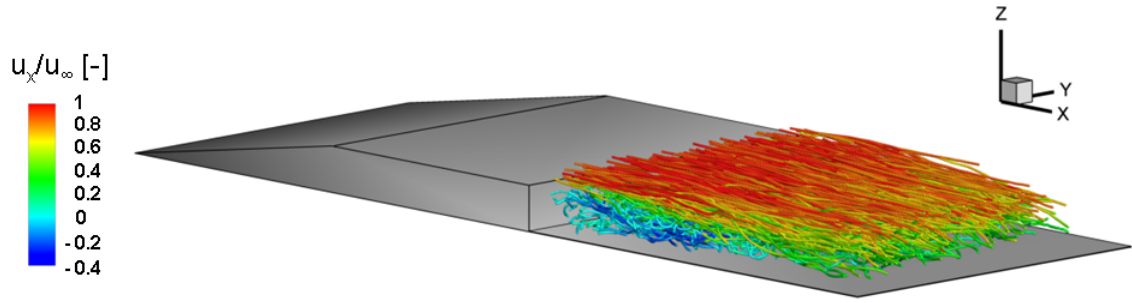
Fig 2.38 Direct 3D visualization of Lagrangian trajectories obtained by 3D Scanning PTV. The mean number particle density is 30 particles/cm³. The image shows a sequence of 200 ms and particles tracked for at least 150 ms.

The transformation of the Lagrangian velocity field into the Eulerian velocity field is evaluated by an inverse distance interpolation. Each single time step is interpolated on a grid of 16x90x60 mm³ with 1 mm spacing. In a next step, erroneous vectors are deleted by a simple threshold of magnitude in velocity (0.5 m/s). The resulting velocity field is mean averaged over a 3x3 kernel and further interpolated in a temporal manner by averaging three time steps. The interesting time scale in this thesis is far below 1 kHz, see section 3. The resulting Eulerian velocity field is shown in figure 2.39. The voluminous velocity field is represented by slices, colour-coded with normalized streamwise velocity.
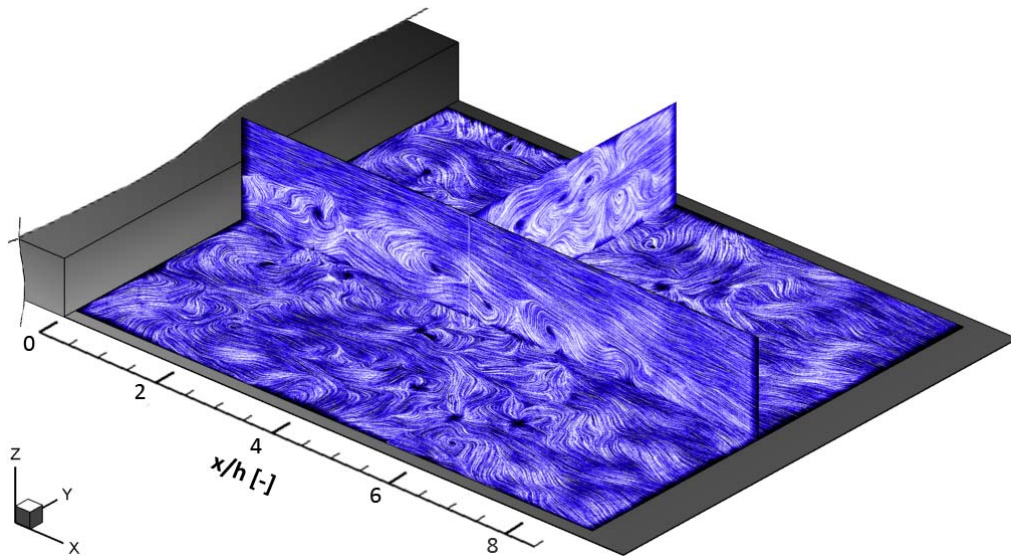
Fig 2.39 Instantaneous Eulerian velocity field calculated by inverse distance interpolation. vector field is visualized via slices through the volume. Slices are colour coded by Line Integral Convolution (integration length: 15 frames)

3 Backward Facing Step Flow

In the last decades, several extensive investigations (experimentally and theoretically) have been performed to analyse the characteristics of the backward facing step flow, even though most of the results deal with the statistical description of the flow phenomena. Major part of the experimental studies used pointwise measurement techniques such as Laser-Doppler Velocimetry (LDV) or Hot Wire Anemometry. The pointwise measurement techniques yield high temporal resolution and high accuracy at low spatial resolution. The techniques were primarily used to characterize integral flow behaviour of the BFSF and its sensitivity to changes of e.g. aspect ratio, expansion ration, Re-number and boundary layer thickness.

This chapter gives an overview of the state of the art regarding the BFSF and gives a detailed description of the implemented BFSF geometry. The literature is reviewed twofold. On the one hand influences on the mean behaviour of the BFSF are described. On the other hand unsteady phenomena regarding the BFSF are reviewed in detail. The integration of the present flow configuration into the large amount of available literature is documented by the integral results obtained by the planar measurement techniques.

3.1 Inlet Flow Conditions

The mean velocity field in the symmetry plane is shown in figure 3.1. The flow is colour coded with the normalized magnitude in velocity. Furthermore, streamlines are plotted for visualization of the flow structure in the recirculation region. Three independently performed planar measurement realizations are used for the calculation of the mean velocity field resulting in a total amount of 12000 vector fields in 480 s for each plane. The bulk velocity U_{bulk} is calculated at x/h = -0.5 to U_{bulk} = 0.47 m/s. The corresponding Reynolds number based on the equivalent diameter of the rectangular cross section of the flow tunnel is Re_d = 40000 (at 292.15 K). The Reynolds number Re_h based on the step height is 4440 (at 292.15 K).

The magnitude in velocity increases in streamwise direction between -12<x/h<-6, is constant in between -6<x/h<0 and decreases due to the sudden expansion between 0<h<12h. Two structures are visible by the streamlines in the low speed recirculation area (0<x/h<6), a primary recirculation vortex (clockwise) and a secondary corner vortex (counter-clockwise).
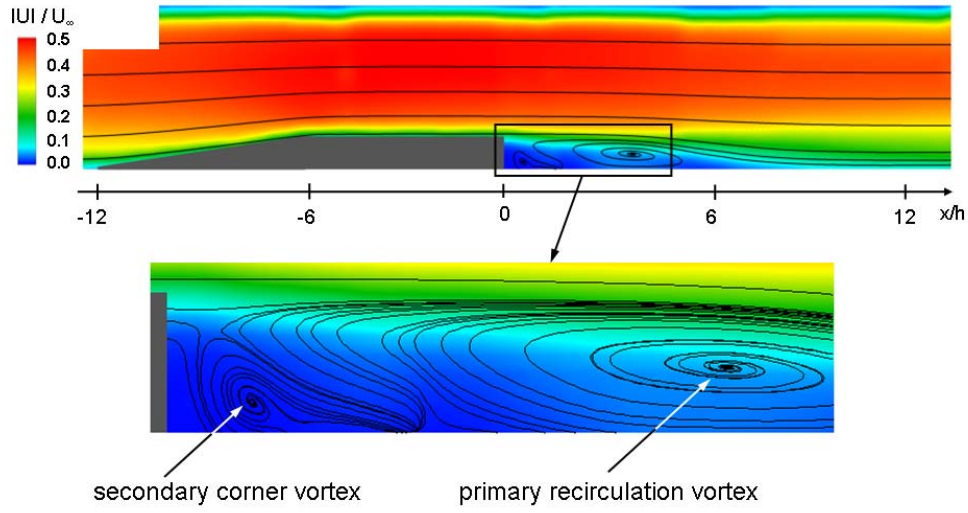
Fig 3.1 Mean BFSF between -12h<x<12h. The flow is colour-coded with the dimensionless magnitude in velocity. Streamlines are used for visualization of flow topology.

At x/h = -6 the flow exhibits a strong directional change. Here, the boundary layer separates and influences the tunnel flow. A shear layer develops, reattaches and recovers. The length of the recovery region is calculated via the deviation of several velocity profiles between -5<x/h<0.5 from the mean velocity profile at -0.5h. Figure 3.2 on the left shows the influence of the angled edge, which ranges up to -2h. In the range -2<x/h<0 the deviation is nearly constant. Thus, the flow is considered to have reached a fully developed state again at the BFS.

The normalized boundary layer thickness is defined by the momentum thickness with respect to the step height:

$$\theta^* = \theta / h = \frac{1}{h} \int \frac{u(z)}{u_\infty}\left(1 - \frac{u(z)}{u_\infty}\right) dz \tag{3.1}$$

Figure 3.2 on the right shows the boundary layer thickness (momentum thickness) as a function of distance from the step. The edge from inclination to plateau triggers the boundary layer thickness resulting in a thickening of the boundary layer up to x/h=-2. In the range -2<x/h<0 the boundary layer thickness is nearly constant (a kind of engaging) validating the fully developed flow regime. The mean turbulence intensity in streamwise direction Tu_x is calculated to 4,32%, whereas Tu_x has a maximum of roughly 8% near the wall.
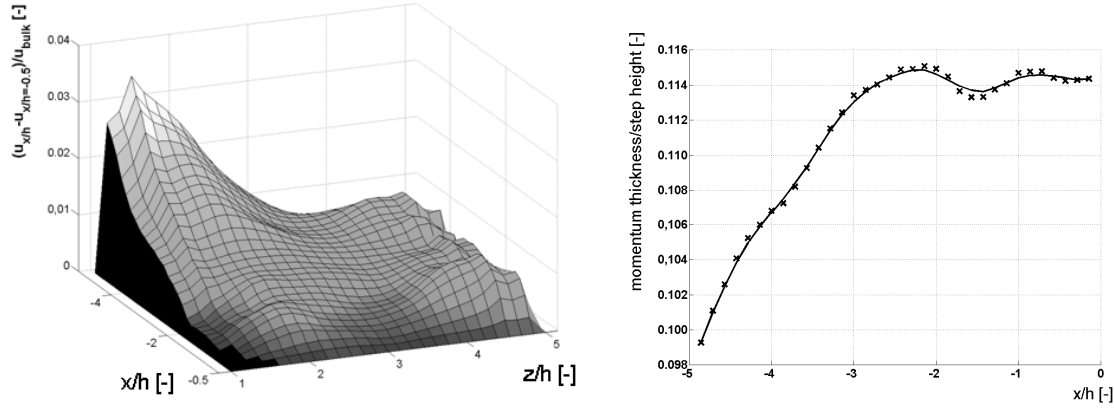
Fig 3.2 (left) Deviation of several velocity profiles between -5h<x/h<0.5 from the mean velocity profile at -0.5h; **(right)** boundary layer thickness in the range -5<x/h<0

The mean velocity profile scaled with the wall shear velocity at y/h = -0.5 is shown in figure 3.3. The outer region ($z^+ > 65$) is obtained by recordings of the telecentric lenses and the inner region ($z^+ <= 65$) by recordings with a larger magnification using the LDM. The velocity profiles are composed and cubic interpolated. The wall shear velocity u_τ is estimated by the conventional Clauser chart method [24]. The method assumes a universal boundary layer profile. The wall shear velocity u_τ is estimated by a least squares fitting for optimally suiting the universal turbulent velocity profile. The wall shear velocity results in $u_\tau = (\tau_W / \rho)^{1/2} = 25$ mm/s $\approx 1/20 U_{bulk}$. The universal constant values used for that purpose are $\kappa = 0.41$ and A = 5.3. The small lack between universal boundary layer profile and calculated velocity profile for $z^+ > 50$ is due to the positive pressure gradient [130]. The universal boundary law assumes a flow with zero pressure gradients. Despite high spatial resolution of the LDM (SR=3μm/pix), it is not possible to obtain correct data for $z^+ < 25$. Reasons are the difficulty of near wall PIV measurements. The near wall region is characterized by reflections, stray light of particles settled at the wall and insufficient seeding. Near the wall, particles tend to move away from the wall. Nevertheless, the scaled velocity profile at x/h = -0.5 clearly indicates a turbulent flow regime.
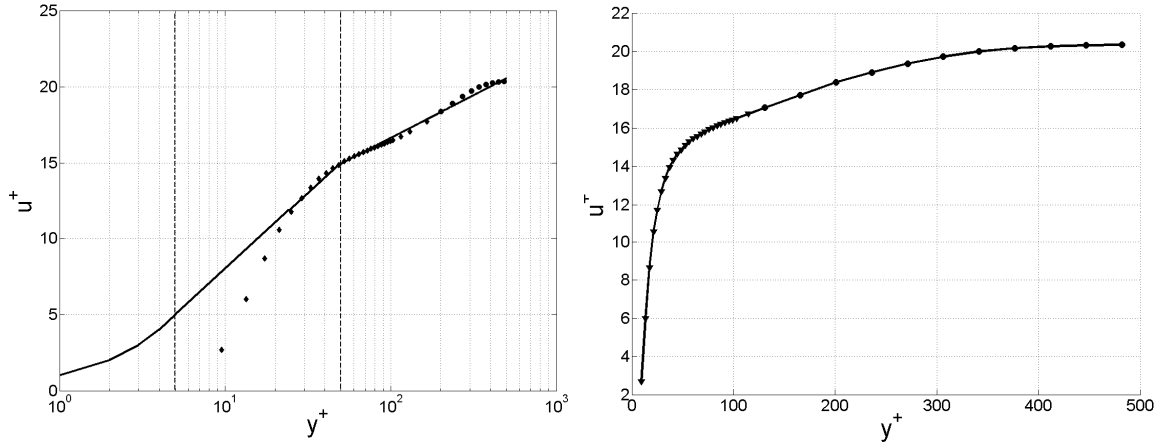
Fig 3.3 Sublayer scaled velocity profile in the symmetry plane at x/h = -0.5 **(left)** logarithmic **(right)** linear

3.2 Mean Flow Characteristics

A large amount of high quality datasets and publications exist describing the mean flow characteristics of the BFSF. This allows a general classification of the present BFSF geometry. Basic for the general classification is the integral parameter *"reattachment length"* x_R. It is defined by the streamwise distance between separation and the time averaged reattachment point and is determined in three different ways in literature: intersection of zero-velocity line with bottom wall, intersection of dividing streamline with bottom wall or point upon the bottom wall with 50% positive and negative streamwise velocity components in all measurement ensembles (especially in pointwise measurements). All methods deliver similar results with low deviation. In this study, the zero velocity line is chosen due to direct availability. For that purpose, the change of sign in streamwise velocity downstream of the step at a constant level of y/h=0.1 is calculated. Figure 3.4 on the left shows the mean streamwise velocity plotted along x/h downstream of the BFS at y/h=0.1. Two zero crossings are apparent. The first zero crossing at x_{r2} is the secondary reattachment point resulting from the corner eddy. The further downstream zero crossing at x_{r1} is the primary reattachment point. Figure 3.4 on the right shows the normalized instantaneous reattachment lengths x_{r1}/h and x_{r2}/h as a function of time for a period of 10s. The sampling frequency is 25 Hz. Furthermore, the mean values of $x_{ri\ mean}$ are plotted as dashed lines. The reattachment length of the recirculation area is 5.65h +/- 1.5h, that of the secondary recirculation length 1.24h +/- 1h. A clear frequency is not observed.
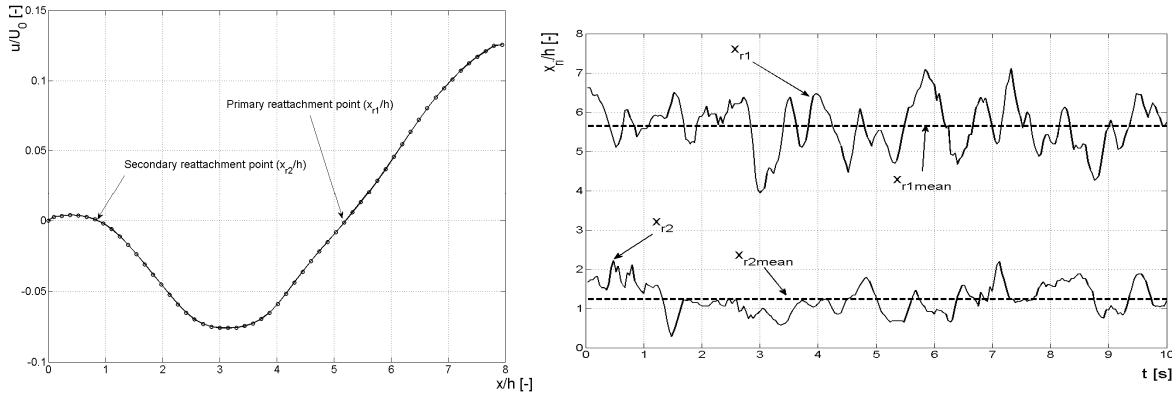
Fig 3.4 (left) Definition of reattachment (**right**) reattachment as function of time, sampling frequency is 25 Hz

The main influences on the reattachment point/line are *Reynolds-number* Re_h, *expansion ratio* ER, *aspect ratio* AR and *boundary layer thickness* θ^*. One of the first authors describing the quantitative behaviour of the BFSF for varying **Re_h** is Armaly et al. (1983) [4]. They studied the BFSF (ER = 1.94, AR = 18) by measuring the downstream velocity distribution and the mean reattachment length via Laser-Doppler measurements. Assuming the flow to be fully developed and two-dimensional, they observed an on average two dimensional flow only at low ($Re_h < 200$) and high Reynolds numbers ($Re_h > 3000$) downstream of the BFS. In between, the mean flow is strongly three-dimensional. In the laminar regime the reattachment length increases with Re to a maximum of 17h. In the transitional regime the reattachment length decreases down to 6h, and approaches a constant value of 7h in the turbulent regime. The authors postulate increasing turbulent entrainment of the shear layer while convecting above the recirculation region, which results in a decrease of fluid volume in the inner of the recirculation region. Thus, the point of reattachment is shifted closer towards the step. The authors note an influence of the rather high expansion ratio as they observed a second recirculation zone on the top wall. Durst and Tropea (1981) [31] and references herein measured several ***expansion ratios*** for varying Re-numbers. The results are shown in figure 3.5 on the left. The authors claim that when defining the Re-number scales with the step height, all measurements approach the same curve for different expansion ratios, which is not the case for a Re-number defined with momentum thickness upstream of the step. Furthermore, figure 3.5 shows the behaviour of the present test case, which is in good agreement with literature. The Re_h-number of 4440 describes the sate with a minimum of reattachment length. Figure 3.5 on the right shows the reattachment length as a function of ER. At low expansion ratios, the mean reattachment length increases, whereas the gradient decreases beyond a distinct

expansion ratio. Controversially, Ötügen (1991) [94] observed a decrease with increasing expansion ratio. The installed BFSF differs largely from the curve.
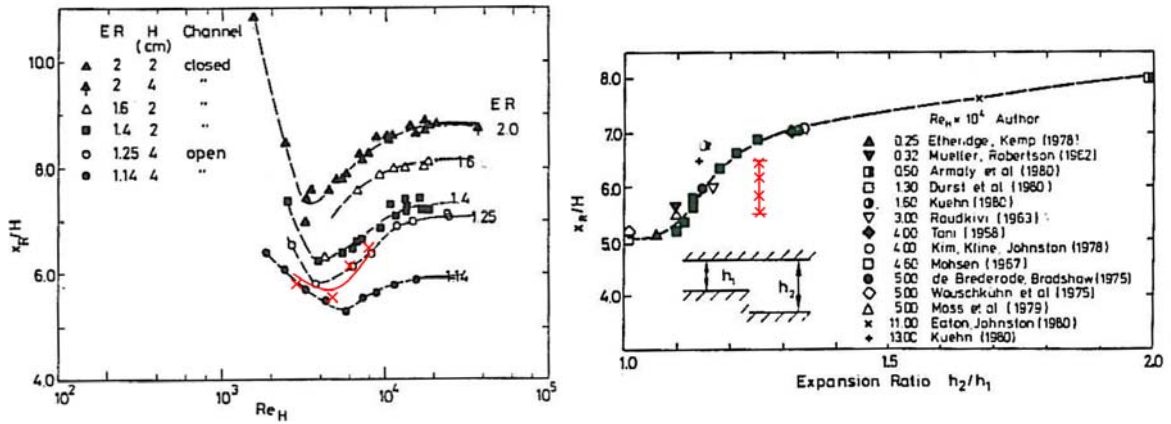
Fig 3.5 (left) Influence of Re-number on mean reattachment length for variable expansion ratios **(right)** influence of expansion ratio on median reattachment length [31]

These deviations are not new in different BFSF geometries. Deviations are already documented for identically experimental conditions of the BFSF by different authors, which are by far beyond the accuracy of the applied measurement techniques as shown in figure 3.6 on the left, especially at high Re-numbers. Motivated by the deviations, the influence of *boundary layer thickness* is studied by Adams and Johnston (1988) [1]. The boundary layer thickness is manipulated using a combination of upstream wall suction to reduce the boundary layer thickness and trips to thicken it. The boundary layer profile is measured by detailed hot-wire measurements. Results are presented in figure 3.6 on the right. The authors generated a parameter space of Re-number and boundary layer thickness and characterized important regions, ranging from laminar separation and reattachment to turbulent separation and reattachment as well as mixings of both regimes. From these results, the authors concluded that there is a strong dependency on initial boundary layer state, especially in the transitional regime, where the re-increase of reattachment length is observed, see figure 3.6 on the left. To the author's point of view, the state of the shear layer (laminar/transitional/turbulent) is responsible for the reattachment length as concluded by others, too. The length required for a shear layer to reach a fully developed turbulent state is much longer than the reattachment length. Thus, the shear layer is not fully developed at reattachment and carries the footprint of the initial conditions. With respect to Adams and Johnston (1988) [1], the present BFSF configuration with $\delta/h=0.116$ and $Re_h=4440$ is in the mixing state of transitional separation and turbulent reattachment.
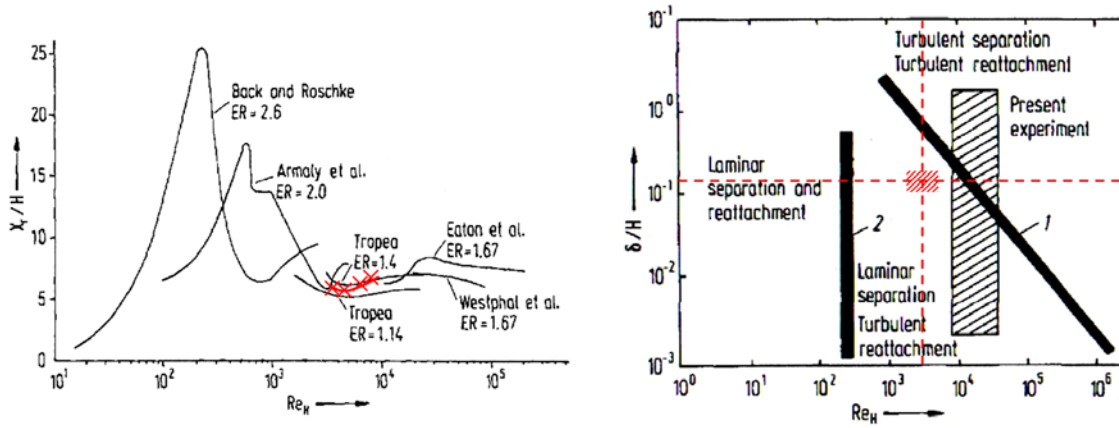
Fig 3.6 (left) Influence of Re-number on mean reattachment length for several experimental investigations. **(right)** The location of transition regions for the BFSF in the parameter space of Re_h and δ/h at ER=1.25 and AR=11 [1]

Most of the investigations regarding the BFSF assume on average two-dimensional flow in the symmetry plane for *aspect ratios* larger than AR>10. Brederode (1972) [16] defined a criterion for the **aspect ratio** AR>10 for assurance. Nevertheless, the width of the channel is not infinitely large since it ends abruptly at the sidewalls. Numerical simulations at rather low Re-numbers showed that the side walls result in the creation of a wall jet directed from wall towards the symmetry plane [146], [13]. Chiang and Sheu (1999) [22] extend the necessary AR to 50 to assure two-dimensionality. The numerical findings are validated by Tylli et al. [138] experimentally via PIV for an AR=20 (ER=2). PIV and stereoscopic PIV measurements showed an increasing intensity of the wall jets with increasing Re at Re<1000 and a decreasing intensity of the wall jets with increasing Re at Re>3000. The present AR of 57 clearly shows sidewall jets as described in literature, see figure 3.7. A cross flow is generated immediately in the vicinity of the step directing from sidewalls to the symmetry plane.
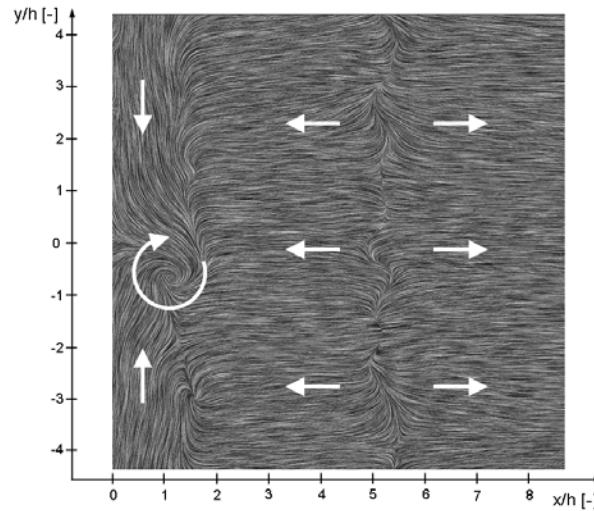
Fig 3.7 Mean flow field in the x-y- plane visualized via Line Integral Convolution. The mean reattachment line is at roughly x/h=5.2 Sidewall jets are apparent in the range 0<x/h<1. The white arrows indicate flow direction.

3.3 Dynamical Flow Features

Beside the analysis of the mean flow field via pointwise measurement techniques, unsteady flow features are apparent in the transitional and turbulent regime. In principal, there are five large scale effects: a) shear layer roll up, b) vortex growing and merging, c) flapping of the shear layer, d) fluctuating position of the reattachment line and e) fluctuating recirculation region. It is obvious that each unsteady feature influences the other and vice versa. Thus, the understanding of the physical character and behaviour of the dynamical process needs the extraction of each feature simultaneously. Furthermore, to resolve the dynamics of the unsteady features, the whole field needs to be measured successively with a high temporal resolution. These conditions are not achievable with conventional pointwise measurement techniques. More sophisticated experiments were carried out using PIV or surface pressure measurement via microphone arrays. The main advantage of PIV is the possibility to combine topological analysis with quantitative velocity measurements giving hope to extract coherent flow structures [116]. Footprints of coherent structures are measured by surface pressure measurements, if the probes are arranged in a planar set-up [53]. Furthermore, sophisticated combinations of pointwise and surface pressure measurements allow the estimation of the volumetric velocity field [51] under certain restrictions and assumptions, e.g. Taylor's frozen hypothesis. Numerical simulations with sufficient temporal and spatial resolution are nowadays limited to Re_h = 3000 [118]. The

authors complain a lack in three-dimensional and time resolved data corresponding to higher Re-numbers.

Shear layer roll up

Following the path of a fluid element started immediately upstream of the step, the first fluctuation appears as the shear layer rolls up and generates discrete vortices being shed into downstream direction, see figure 3.8. Troutt et al. (1984) [137] measured the shear layer via multiple hot-wire technique. Their results indicate a spanwise vortical structure similar to that of a free mixing layer, named as rollers in the following. Similarities to a free mixing layer and the corresponding rollers are also observed by other authors [71], [118], [116]. Scarano et al (1999) [116] performed instantaneous, planar PIV measurements in the pointwise symmetry plane with a high spatial resolution ($Re_h = 5000$). They applied a pattern recognition technique to detect large scale coherent structures appearing downstream of the BFS flow in the shear layer. The vortical structures in the symmetry plane of the turbulent shear layer were sized between 0.12h and 0.44h. Up to x/h=3.5, small vortices (< 0.22h) in the shear layer show a quasi-linear growth resulting in high kinetic energy budgets. From linear instability analysis it is widely accepted that this characteristic formation is the consequence of Kelvin-Helmholtz instability. The authors support the hypothesis of early 3D breakdown of these primary rollers. It is commonly accepted from measured velocity fluctuation in this region that the shedding frequency downstream of the step is in the order of $St_h \approx 2 \cdot 10^{-1}$ [87].

Shear layer development

Further downstream is the region of shear layer development and convection of rollers within the shear layer. Trout et al. (1984) [137] showed an increase of the shear layer thickness with increasing distance from the step. The authors postulate that the growth of the shear layer is strongly connected to vortex pairing mechanisms as omnipresent in free mixing layers. The convection velocity of the spanwise vortical structure is estimated to $0.6U_0$ [54]. Snapshots of vortex pairing are qualitatively observed via LIF measurements by Kostas et al. (2002) [69]. Nevertheless, the sampling frequency is too low for resolving pairing events. Furthermore, the authors performed detailed instantaneous 2D-PIV measurements in several x-y and x-z planes downstream of the BFS ($Re_h = 4660$). Beside the calculation of vorticity, Reynolds stress and turbulent kinetic energy production, Proper Orthogonal Decomposition (POD) has been performed trying to extract high energetic

flow structures. Vortex trains and pairing are observed in the separated shear layer increasing the turbulent stresses and turbulent kinetic energy production. The Reynolds stress peaks were associated with vortex pairing and vortex growth in the shear layer. The largest amount of turbulent kinetic energy was located at regions of small but intense vortices. The POD showed mostly uniform vortical structures near the step and increasingly irregular structures downstream of the step. The authors suggest an increase of three dimensional turbulent vortex interactions with increasing distance from the step. Delcayre and Lesieur (1997) [27] observed Λ-vortices resulting from three-dimensional distortions of the rollers. Hudy et al. (2006) [51] studied the temporal evolution of coherent structures via surface pressure measurements (Re_h=8000). They synchronized the time resolved surface pressure measurements with 2D PIV measurements at 10 Hz. A large scale coherent structure was found developing at half of reattachment length inside the recirculation region. The structure grows in size to about the step height and then sheds and accelerates downstream. This temporal growth of the flow structure is compared with the development of the vortex structures in the wake of a bluff body (wake mode – temporal growth, shear layer mode – spatial growth).
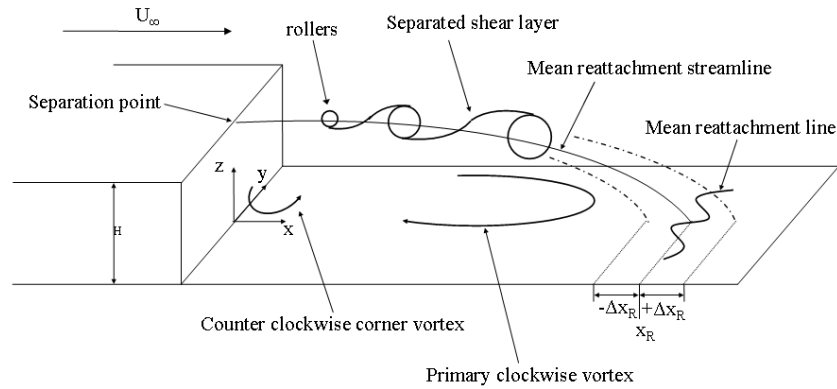
Fig 3.8 Principal sketch of the unsteady flow phenomena

Shear layer reattachment

Next highly fluctuating and dynamical process is the shear layer impinging. The impinging of the separated shear layer on the wall generates positive streamwise velocities downstream of reattachment and negative streamwise velocities upstream of reattachment. Instantaneous measurements show a fluctuation of the reattachment point of roughly Δx_R=2h in the transitional and turbulent regime. Huang and Fiedler (1997) [50] measured the fluctuation of the reattachment length via PIV to f_R = 0.4 Hz corresponding to St_h=0.04 (ER = 1.25, AR = 2.5, Re_h = 4300). This is close to the results obtained by the direct

numerical simulation performed by Le et al. (1997) [71], which shows a quasi-periodic fluctuation of St_h=0.06. Furthermore, DNS show a sawtooth pattern of the temporal reattachment location [71], [118]. Starting from a short reattachment length, the reattachment point moves downstream in a continuous way. Suddenly, the reattachment point breaks up in two parts, indicating shrinkage of the recirculation region and shedding of a part of the recirculation region. This is confirmed by Lee et al. (2002) [54] via pressure measurements. Furthermore, the reattachment position varies also in spanwise direction. This is shown in the DNS by Le et al. (1997) [71] and confirmed by Jovic and Driver (1995) [59]. Nevertheless, the authors used a rather low AR of 4, probably having a large influence of the side walls on reattachment position. In Beaudoin et al. (2004) [11], an approximately side wall independent wave length is measured for AR=15 at a rather low Re_h=300. The independent wave length is positioned near the streamwise symmetry plane indicating the decreased influence of the sidewalls. To the authors point of view there is a lack of results showing the spanwise structure of the reattachment line.

Recirculation region

As three dimensional coherent vortex structures in the separated shear layer and in the recirculation region seem to influence the behaviour of the unsteady flow, Lee at al. (2002) [55] studied the large scale vortical structures of the BFS flow three-dimensional via extensive coupled pressure-velocity measurements. The conditionally averaged measurements showed "hairpin-like" coherent vortex pairs in the recirculation area with length scales from 2.5h to 4h. They indicated the growing of the vortices moving downstream. Recent results indicate that hairpin like structures are generated at shear layer impinging. Schröder et al. (2011) [127] study a manipulated BFSF with laminar separation via tomographic PIV. The authors show the generation of hairpin like structures in both flow directions with respect to the reattachment line, when the generated rollers impinge on the wall. Highest negative velocities appear in the region 3<x/h<4.

Step corner and recovery region

The unsteady behaviour of the BFS flow in the vicinity of the step corner has been investigated by Spazzini et al. [9] via skin friction measurements and flow visualisation. They observed a cyclic process of growing and successive breakdown of the secondary corner eddy. As the region of the step corner is of lower interest in the present study, the reader is referred to Spazzini et al. [9] and references herein for more detailed information.

Downstream of reattachment is the recovery region, where the shear layer redevelops to a usual turbulent boundary layer [69]. Organizations of vortex packets are found comparable to that observed in the turbulent boundary layer measurements by [2], [27].

Global unsteadiness

Beside the locally fluctuating features described above, a global unsteadiness of low frequency exists in the BFSF. Driver et al. (1987) [28] among others measured the power spectrum of velocity fluctuations near the reattachment line with LDV. The streamlines in the conditionally averaged mean flow show a global change in flow pattern. The corresponding frequency has been estimated to be one order of magnitude lower than the shedding frequency [133]. The origin of this unsteadiness is controversial. Different proposals are described in literature ranging from flapping of the shear layer to vortex breakdown at reattachment.

In [32], Eaton and Johnston (1980) suggest that the low frequency fluctuation corresponds to the flapping of the shear layer. The flapping of the shear layer is caused by an oscillating volume of recirculating flow. They suggest that the unsteady recirculation volume is a result of imbalance between shear layer entrainment from the recirculation volume and injection of fluid near reattachment. The imbalance occurs, when the spanwise rollers suffer a rapid breakdown. The consequence of rapid breakdown is a decrease of entrainment rate and thus a growing of the recirculation volume. Due to the short term breakdown, the entrainment rate decreases and the recirculation volume grows. Similar to Eaton and Johnston (1980) [32], the dynamical behaviour of the shear layer is made responsible for the low frequency flapping in Driver et al. (1987) [28]. Differences are found in the disorder of the shear layer that alters the rate of reverse flow. It is understood that a vortical structure with a locally higher convection velocity than the neighbours can "escape" the recirculation region. The reduction of reverse flow mass results in collapse of the separation bubble. Schäfer et al. (2009) [118] link quasi-periodic rollers with the fluctuation of the recirculation region. The rollers carry reverse flow mass from the recirculation region while convecting downstream and passing the reattachment location. The passing of the rollers is followed by a sudden shrinkage of recirculating region. The observations are based on numerical flow visualization and quantitative study of the temporal reattachment location. In contrast to other authors, who see the shear layer mode as basic motion for fluctuation, Hudy et al. [51] suggest a scenario, where the dynamics are driven by the wake mode nature of separated flows. The proposal is concluded via

combined surface pressure and planar PIV measurements. The authors observe a temporal growth of a large scale structure located in the recirculation region at half the reattachment location. At distinct size, the structure is transported downstream carrying reverse flow.

The starting flow behind a backward facing step is studied by Brücker (1999) [18] in a volumetric manner via 3D Scanning PIV. Generation of large primary vortices are observed. In addition, a secondary vortex is generated within the corner which displaces the primary vortex and tilts-up the flow between both vortices. This "burst" can partly affect the main flow up to the center. To this moment, the behaviour of the position of the reattachment point changes from a square-root function to a linear function with time.

To summarize, most of the unsteady frequencies and resulting proposals are based on measured velocity fluctuations in a single point or instantaneous, but not time-resolved, planar or volumetric velocity maps. Up to now, temporal and spatial resolution has only been achieved by numerical simulations, see Le et al (1997) [71] or Schäfer et al. (2009) [118] at rather low Re.

4 Results and Discussion

The investigation of the BFSF is discussed with respect to the categorization shown in figure 4.1. The categorization is close to Rinioe et al. [109] in a slightly changed manner. Region I is positioned immediately downstream of the edge centred at y/h=1, where shear layer roll up and vortex shedding appears. The Kelvin-Helmholtz instabilities amplify while convecting in region II. Here, shear layer development and vortex convection/interaction is observed. Due to the amplification of the instabilities and the imposed pressure gradient, the shear layer finally impinges downstream on the wall. Region III is characterized by a highly fluctuating and three-dimensional state generating intense velocities in up- and downstream direction. The interface between recirculation region (IV) and shear layer (I, II) is characterized by a large turbulent entrainment. Region V contains the flow in the vicinity of the corner. The recovery region (VI) is positioned downstream of reattachment. Here, the separated boundary layer redevelops.
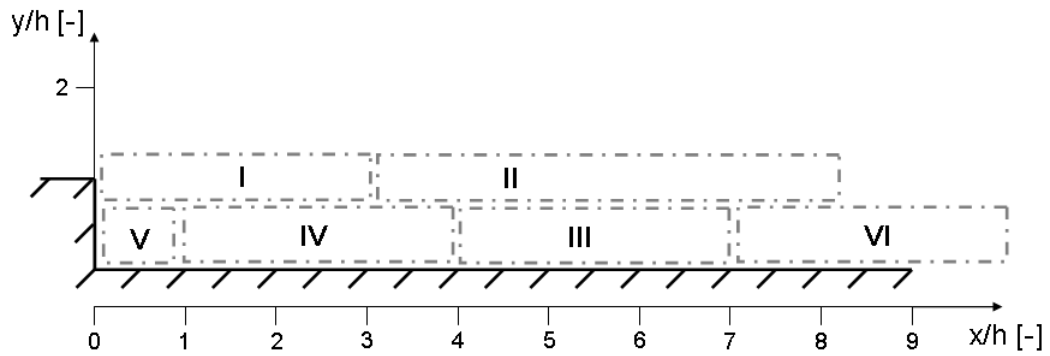
Fig 4.1 Categorization in regions: I: shear layer roll up; 0<x/h<3, 0.7<y/h<1.5; II: vortex convection, 3<x/h<8, 0.5<y/h<1.5; III: reattachment zone, 4<x/h< 7, 0<y/h<0.7; IV: recirculation zone 1<x/h<4, 0<y/h<0.7; V: sidewall jets and corner eddy, 0<x/h<1, 0<y/h<0.7; VI: recovery zone 7<x/h<9, 0<y/h<0.7

4.1 Region I: Shear Layer Roll Up

The sudden geometrical expansion forces the boundary layer on the bottom wall to separate at the step edge. The separated boundary layer is influenced by high shear gradients $\delta u / \delta z$ immediately downstream of the step. In region I, the properties of the separated shear layer are similar to that of a free mixing layer. Differences are found in the state of the velocity profile of the low speed side as shown in figure 4.2. The velocity ratio in the BFS-geometry is negative and rather high. Furthermore, the lower region is

dominated by unsteady events resulting in temporal and spatially differing velocity profiles.
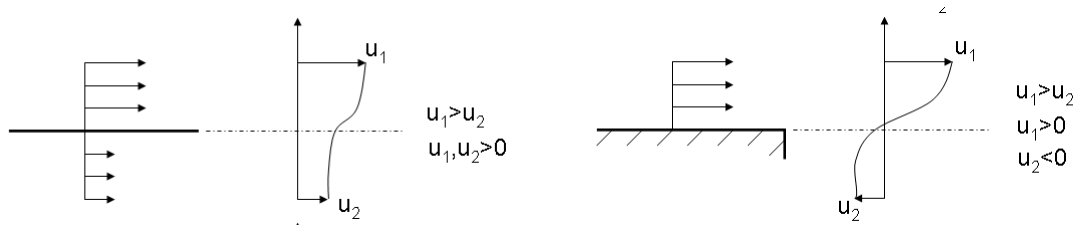
Fig 4.2 Comparison of mixing layer generated at a flat plate **(left)** and a shear layer generated at a backward facing step **(right)**

The transition from laminar state into turbulent state in case of a mixing layer behind a splitter plate is studied by Meiburg et al. (1988) via a periodically perturbed laminar flow along the span [84]. Stunning flow visualization is presented by the authors showing the skeleton of the shear layer as a wavy structure with cells. Figure 4.3 on the left shows the case if perturbations on upper and lower side are out of phase and the figure on the right shows the in phase configuration. The in phase mode leads to nearly regular distributed rollers, which are amplified in downstream direction. The rollers are connected via streamwise vortex tubes generating three-dimensionality. The authors indicate a strong influence of magnitudes in perturbation and consequently a strong influence of the instantaneous velocity ratio on the state of the shear layer.
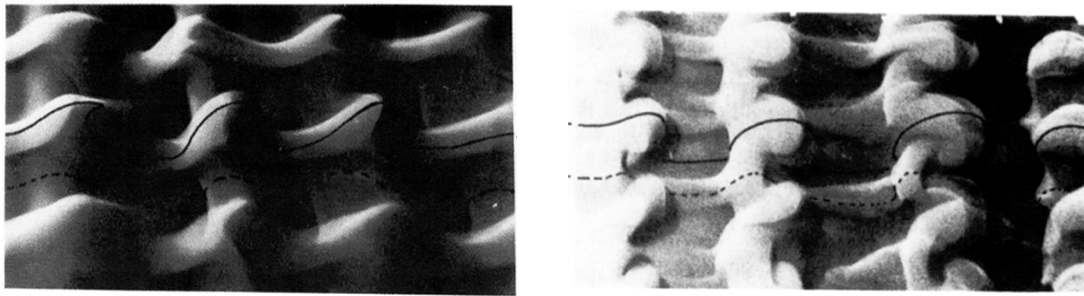
Fig 4.3 Flow visualization of a free mixing layer generated downstream of a splitter plate via periodic perturbations: **(left) i**n phase perturbation on upper and lower side; **(right)** out of phase perturbations on upper and lower side [84]

In the present BFSF, the perturbations are natural without periodicity, depending on the one hand on the initial state of the inlet flow and on the other hand on the unsteady perturbations generated in the recirculation region. Figure 4.4 shows exemplarily LIF visualizations of region I. The boundary layer separates at the step edge and vortex

shedding begins downstream of the step. Three different states of the shear layer roll up are shown, in the following damped state, regular state and amplified state. The states are categorized by visual inspection. The damped state is characterized by a long distance between vortex roll up and step edge. In the regular and amplified state, the roll up of the shear layer already appears at roughly x/h=1. The KH-type instability leads to growing of the vortices while convecting downstream. The streamwise wave length of the rollers is defined by the distance between the rollers. With increasing distance from the step, the wave length increases. The amplification of the rollers size with increasing distance from the step is rather moderate in the regular state, while high in the amplified state. The amplified state is characterized by loss of coherent structures within three step heights downstream of the step. However, the spatial structure of the rollers is not clear from the visualization. Here, the analysis of the volumetric velocity field gives a further inside into the spatial structure of the shear layer and allows a look at the reasons forcing the different states.
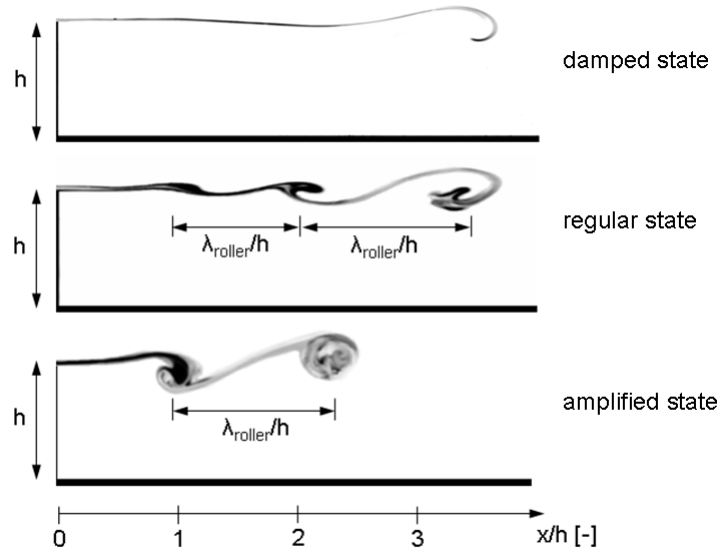
Fig 4.4 Post processed LIF visualization of shear layer formation in region I (0<x/h<3.5)

Shear layer extraction

The extraction of shear layers is a crucial part in the analysis of coherent structures as stated by Schafhitzel et al. (2010) [120]. Shear layers are formed long before a vortex is born. This is especially true in the case of the BFSF as the rollers are built due to the shear layer as shown in figure 4.4. Thus, the quantification of the shear layer is essential to extract and visualize shear layers. However, compared to vortex detection criteria, there are only few approaches for identifying shear layers. One approach is the inverted *Q-criterion* (Q<0), see equation 4.5, delivering regions of high shear stress, as the Euclidean

of the rate-of-strain dominates. Haimes and Kenwright (1999) [39] suggest the calculation of a scalar value for identifying regions of high shear. They propose an eigenvalue analysis of the deviatoric rate-of-strain tensor S'. From continuum mechanics it is known that

$$S' = S - \frac{1}{3} \cdot I \cdot trace(S). \qquad (4.1)$$

S' is symmetric and positive delivering three real eigenvalues $\lambda_{S'i}$. The Galilean invariant and objective criteria for a shear layer Cr_{shear} is then defined by:

$$Cr_{shear} = \sqrt{\frac{(\lambda_{S'1} - \lambda_{S'2})^2 + (\lambda_{S'1} - \lambda_{S'3})^2 + (\lambda_{S'2} - \lambda_{S'3})^2}{6}} > 0 \qquad (4.2)$$

High values of Cr_{shear} define regions of high shear. Based on this criterion, Schafhitzel et al. (2010) [120] introduce 2D shear sheets for the presentation of volumetric shear layers. These sheets are defined as 2D height ridges of the criterion Cr_{shear}. Shear sheets represent the skeleton of shear layers, analogous to vortex center lines in the case of vortices. In this thesis, a simplified approach is used in region I, which identifies the shear layer by the analysis of the spatial derivative δu/δz. This is possible due to the geometrical simplicity of the backward facing step as the shear layer is primarily dominated by shear resulting from streamwise velocity gradients perpendicular to the bottom wall, see figure 4.5 on the left. Thus, the center line of the shear layer is defined in approximation by the local maximum of δu/δz for each x- and y-position.

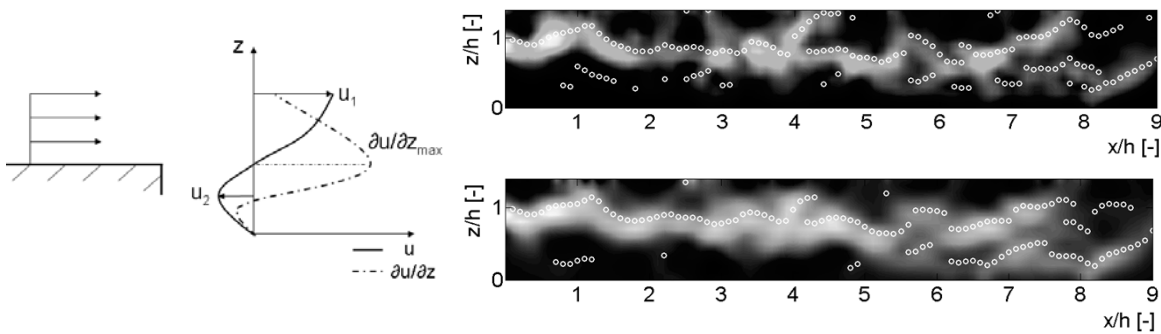**Fig 4.5 (left)** Definition of du/dz$_{max}$-criterion; **(right)** Comparison of Cr-criterion **(upper)** and du/dz$_{max}$-criterion **(lower)**. The plot shows the symmetry plane at y/h=0 and is colour coded by intensity of the single criteria. White means a high intensity and black a low intensity. White dots represent extracted local maxima of the criteria showing the shape of the shear layer.

Figure 4.5 on the right shows the comparison of both criteria for an instantaneous flow situation in the streamwise symmetry plane. Both criteria deliver similar results, especially in region I. Here, both criteria identify the shear layer as a wavy line. With increasing distance from the step (x/h>4), the single shear layer line is increasingly distorted. Furthermore, regions of high shear layers are generated due to the shear layer impinging on the wall.

The spatial connection of the single data points into a surface for geometrical representation of the shear layer is performed by a nearest neighbour and intensity criterion. For that purpose, a representative point is chosen as initial guess. The initial guess for the position of the shear layer in region I is $X/h = (0,y,1)^{T}$. The mean and an instantaneous shear surfaces are shown in figure 4.6. The shear layer is formed over the whole span ranging from z/h≈1 at the step to z/h=0.8 at roughly x/h=6. Below the main shear layer, a second region of high shear is formed located in the recovery region. In contrast, figure 4.6 on the right shows the instantaneous shear layer in the range 0<x/h<4. The shear layer is represented by a wavy structure with heights and ridges. The deviation of the single instantaneous shear planes from the mean is described by superposition of a translational shift and a position dependent wave function. The wavy deviation will be interpreted as perturbations of the shear layer.
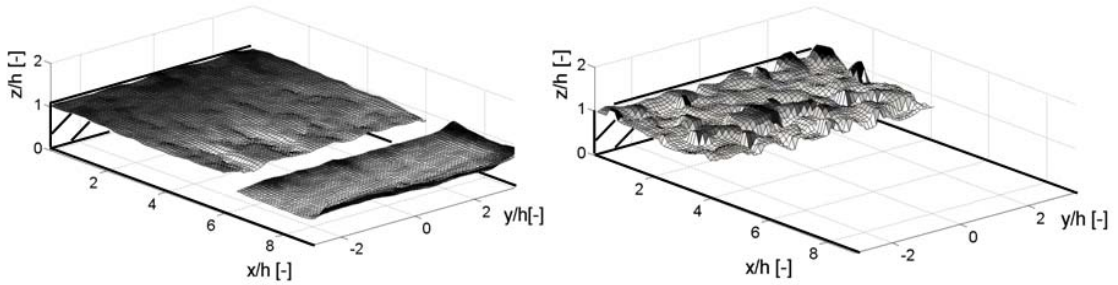
Fig 4.6 Extracted shear surfaces; (**left**) temporal averaged within 2s in the range 0<x/h<9 (**right**) temporal averaged within 3 ms in the range 0<x/h<4

Shear layer thickness

Starting from the shear layer center line, a positive and negative shear layer thickness δ_{+} and δ_{-} is defined by the positive and negative momentum thickness. Main parameters are shown in figure 4.7 on the right. The local maxima of velocities in positive and negative direction are chosen for normalization. The sum of positive and negative thickness is the total thickness δ, respectively δ/h. As stated by Ho and Huerre (1984) [47] the shear layer thickness as well as the growth rate $\partial\delta/\partial x$ is influenced by the velocity ratio of upper to

lower velocity. Here, the splitting of shear layer thickness in upper and lower thickness allows a statement about influences from the upper and lower velocity profile on the shear layer state.

Figure 4.7 on the left shows the pointwise and temporally averaged shear layer thickness as a function of streamwise distance. Several areas are extractable, where a change in shear layer state happens. In the range $0<x/h<1$, the shear layer thickness slightly decreases having a minimum at $x/h=1$. The event is dominated by the change of the momentum thickness in the lower part. Thus, the reason forcing the thinning must lie in region V. At roughly the maximum of the shear strength, the beginning of vortex roll up is observed. From $x/h=1$ up to $x/h=3$ the shear layer performs an approximately linear growth as previously reported by e.g. Troutt et al. (1984) [137], whereas the upper thickness grows faster. Between $3<x/h<4$ the shear layer thickness forms a plateau, which is characteristic for free mixing layers [47]. Here, vortex merging events are observed in free shear layers. It should be noted, that the plateau is forced by the lower boundary layer thickness indicating an influence from region IV. At roughly $x/h=5$ the shear layer interacts with the bottom wall resulting in decrease of shear layer thickness with increasing distance from reattachment.
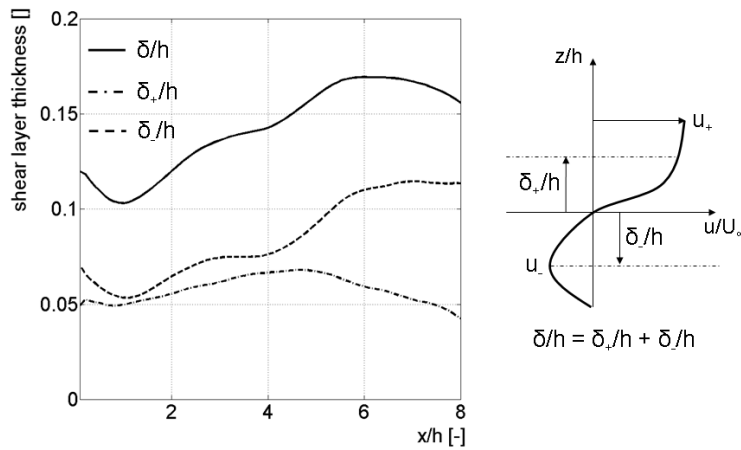
Fig 4.7 Shear layer thickness; **(left)** spatially and temporally averaged shear layer thickness (normalized total thickness δ/h, normalized negative thickness δ-/h, normalized positive thickness δ+/h) **(right)** sketch of important parameters

Shear layer structure

Beside the shear layer thickness and strength, other characteristics are necessary to describe the structure of the instantaneous shear layer. Here, the wave lengths of the perturbations on the shear layer are calculated as shown in figure 4.8 on the left. The figure

shows the magnification of a part of the shear surface immediately downstream of the step. The calculation of local maxima and minima in z-direction delivers positions of height and ridges on the surface. The distance between local maxima and minima is chosen as half the wave length λ_x and λ_y. Furthermore, the amplitude of the perturbation is extracted in the single directions. The probability density function (PDF) of the measured wave lengths in region I is shown in figure 4.8 on the right. The most probable wave lengths in x-direction is $\lambda_x/h = 1.1$ and in y-direction $\lambda_y/h = 1.2$. Furthermore, the PDF is slightly skewed to larger wave lengths. A rather wide range of wave lengths is observed indicating several roll up configurations as shown in figure 4.4.
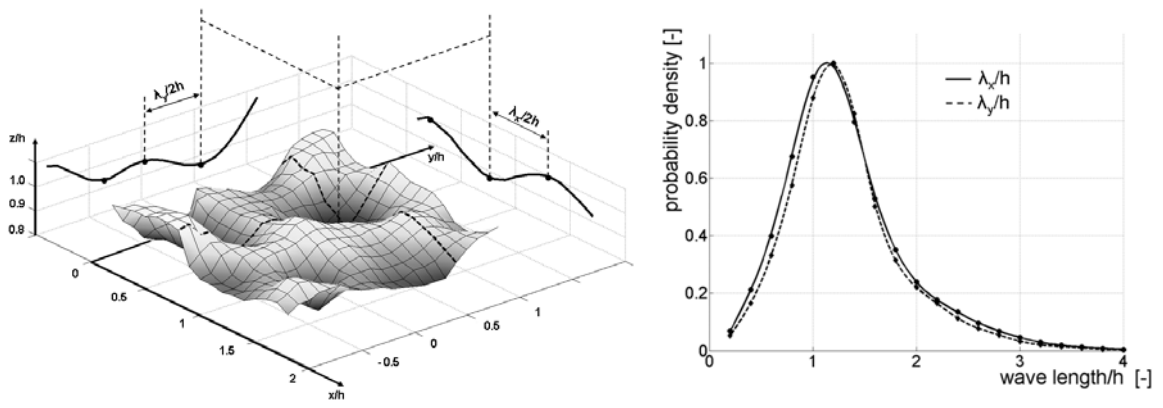
Fig 4.8 (left) Definition of characteristic wave length of the shear layer; **(right)** Probability density function (PDF) of the wave length in x- and y-direction of perturbations on the shear surface.

The shear layer properties in region I as a function of distance is shown in figure 4.9 for a time period of $\Delta t * U_{bulk}/h = 100$ ($\Delta t = 2s$). The figure shows the mean values of the properties calculated in four sections ($0 \leq x/h < 1.0$, $1 \leq x/h < 2$, $2 \leq x/h < 3$, $3 \leq x/h < 4$). The values of the wave lengths λ_x/h and λ_y/h are represented by the maximum of the PDF. The amplitudes A_x/h and A_y/h are given as mean values. The ratio is defined by A_i/λ_i. For reasons of better visibility in the plot, the amplitude and the ratio is multiplied by 10. Figure 4.9 on the left shows the streamwise properties as a function of streamwise distance. The wave length of the perturbations increases only slightly from 1.2h to roughly 1.4h in between $0 < x/h < 3$. In contrast, the amplitude of the perturbations increases about roughly 300% from 0.05h to 0.14h in between $0 < x/h < 3$.

Figure 4.9 on the right shows the spanwise properties of the shear layer as a function of streamwise distance. The wave length slightly decreases up to x/h=3. Here, the wave length in x-and y-direction is nearly identical. This is also true for the amplification and the ratio. In the range $0 < x/h < 2$, perturbations in x- and y-direction converge to a common

value. The streamwise perturbations are amplified and the spanwise perturbations are damped. In the range 2<x/h<4 the rate of amplification is identical for both directions.
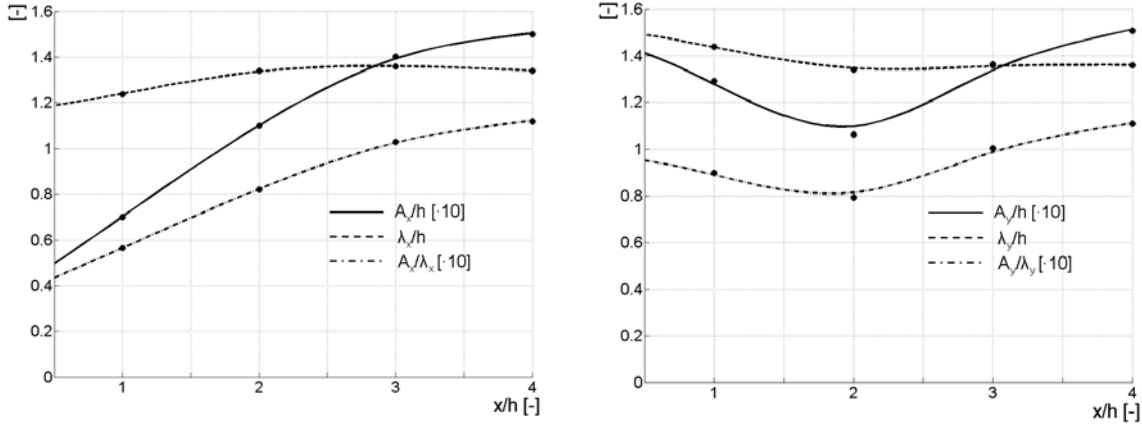
Fig 4.9 **(left)** Shear layer properties in x-direction for region I; **(right)** Shear layer properties in y-direction for region I; solid line: amplitude, dashed line: wave length, dash-dot line: ration of amplitude and wavelength; for plotting, the amplitude and the ration are multiplied by 10

Shear layer convection

The temporal resolution of the volumetric measurements allows a look at the development of single shear layer perturbations. Figure 4.10 on the left shows the projection of the shear layer height on a plane surface for two instants in time separated by 8 ms ($\Delta t U_{bulk}/h=0.4$). The convection of the perturbations is clearly visible. The streamwise frequency of the perturbations is measured by pointwise analysis of the instantaneous shear layer position in z-direction. An exemplarily time signal at (x/h=2.5, y/h=0) and (x/h=3, y/h=0) is shown in figure 4.10 on the right. The displacement Δx_p of the large scale perturbations in streamwise direction is indicated. The mean convection velocity in streamwise direction is calculated via cross correlation to $0.6U_{bulk}$. This convection velocity of the perturbations is in the same range as the roller velocity estimated by e.g. Schäfer et al. [118]. The authors observed regularly distributed rollers convecting downstream. Nevertheless, in the present study the convection velocity of the instantaneous perturbations varies largely as a function of time. As shown in figure 4.10 on the right, the velocities of the perturbations vary in the range $\pm 0.2U_{bulk}$, thus making the estimation of a clear frequency inaccurate. A trend is observed showing that the frequency of fluctuations is slightly increasing in the range 1<x/h<3. The increase of the frequency indicates an acceleration of perturbations in streamwise direction.
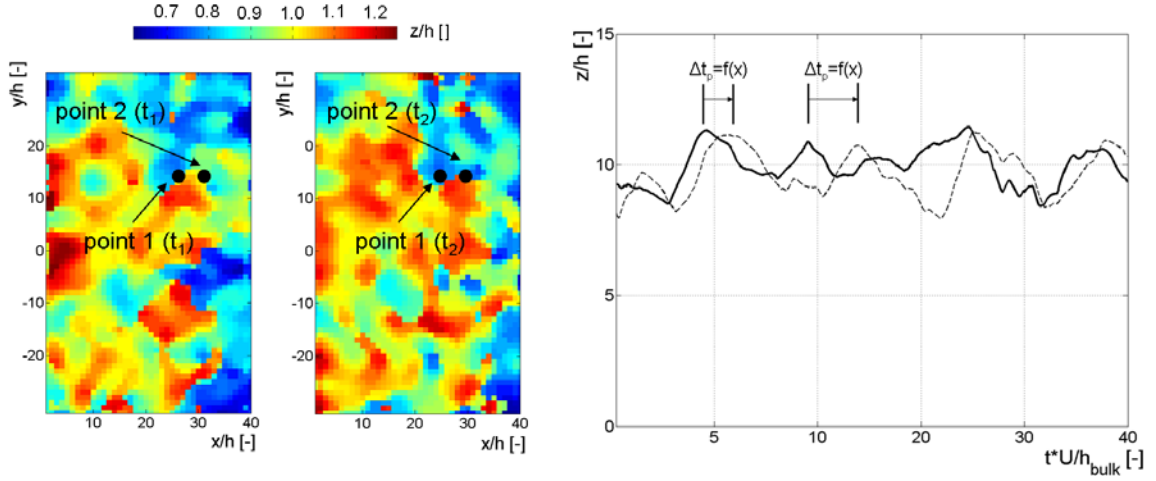
Fig 4.10 (left) contour plot of instantaneous shear layer height in region I; the separation time is 8 ms (t*=0.4); **(right)** time plot of shear layer height; solid line: point 1, dashed line: point 2

The previous analysis extracted main spatial and temporal properties of the shear layer in region I. The shear layer is quantified in terms of position, thickness, strength, wave lengths and amplitudes. The results showed a wavy structure, which is identically amplified in x- and y-direction beyond a distinct point positioned around x/h=2. Furthermore, the analysis determined the convection of disturbances in downstream direction with a transport velocity of roughly $0.6U_0 \pm 0.2U_0$.

Vortex extraction

In the following, the neighbourhood of the shear surface is analyzed. This is a detection of vortical structures in stream- and spanwise direction. Basic principle of multiple vortex criteria is the velocity gradient matrix or the Jacobian of the velocity field. In the Eulerian sense, the Jacobian is defined by applying the gradient operator on the velocity field, see equation 2.15.

Most famous detection criteria are the Q-criterion, the Δ-criterion, the λ_2-criterion and the swirling strength criterion. For a detailed review of these criteria, the reader is referred to Chakraborty et al. (2005) [20]. Common in all detection criteria is the calculation of a scalar field, where large values mean high intensity.

The *Q-criterion* is introduced by Hunt et al. (1988) [52]. The detection criterion is based on the local analysis of the velocity gradient tensor delivering a Galilean invariant criterion for extracting vortical regions. For incompressible flows the Q-criterion is defined as:

$$Q = \frac{1}{2}\left(\|\Omega\|^2 - \|S\|^2\right) > 0 \qquad (4.3)$$

A vortex region is identified, if the Euclidean norm of the rate of rotation tensor is larger than the Euclidean norm of the rate of strain tensor.

The *Δ-criterion*, introduced by Chong et al. (1990) [23], uses the analysis of the discriminate of the characteristic polynomial from equation (2.18).

$$\Delta = \left(\frac{1}{2}R\right)^2 + \left(\frac{1}{3}Q\right)^3 > 0 \qquad (4.4)$$

If $\Delta > 0$, the Jacobian has complex eigenvalues. Topological theory says that if the Jacobian in a point has a pair of complex eigenvalues, the streamline pattern in the neighbourhood of this point is spiralling.

The *λ_2-criterion*, introduced by Jeong and Hussain (1995) [57], uses the pressure minimum criterion in the center of a vortex derived from the two-dimensional Navier Stokes equation under adiabatique assumption. A local pressure minimum exists, if the intermediate eigenvalue

$$\lambda_2\left(S^2 + \Omega^2\right) < 0. \qquad (4.5)$$

The *swirling strength criterion* λ_{ci} is proposed by Zhou et al. (1999) [153]. The criterion is an extension of the Δ-criterion by analysing the imaginary part of the eigenvalues resulting in a quantity for the swirling strength and the local plane of swirling.

Figure 4.11 shows the application of the mentioned criteria to an arbitrarily chosen instantaneous, three-dimensional velocity field of the BFSF. For that purpose, the original 90x65x15 grid (filled with scalar values of the criteria) is sub-sampled on a finer grid about the factor 10 via moving spline interpolation. The figure shows the streamwise symmetry plane. The images are normalized by the maximum value of the single criteria. At first, it should be noted, that all detection criteria deliver similar results. Nevertheless, a difference is found in the contrast of the single criteria. Here, contrast means the strength of a local peak in comparison to its neighbourhood. For that reason, the λ_{ci}-criterion (3rd from the top) is chosen for vortex center estimation. In the range 0<x/h<3 organized vortex roll up is detected by the criteria. Increasingly unorganized vortical structures are apparent with

increasingly streamwise distance from the step as observed by several authors, see e.g Kostas et al. (2002) [69], Scarano et al. (1999) [116] validating the present three-dimensional calculation of the implemented criteria.
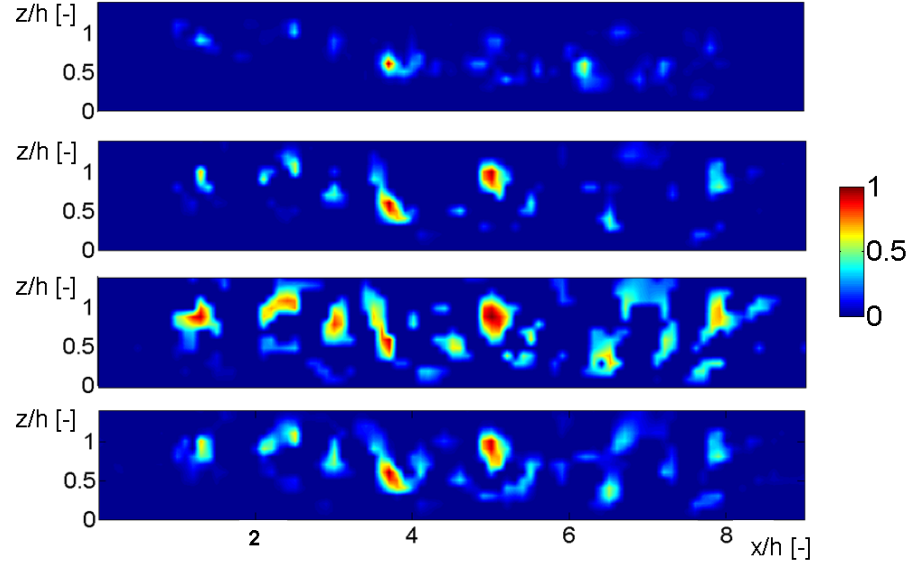
Fig 4.11 Comparison of vortex detection criteria in streamwise symmetry plane; **(top to bottom)** Δ-criterion, Q-criterion, λ_{ci}-criterion, λ_2-criterion

The three-dimensional center $(x/h, y/h, z/h)^T$ of the vortices in the single planes is estimated in the following manner. The spanwise position (y/h) is defined by the analyzed plane in y-direction. The height (z/h) and streamwise position (x/h) is estimated via the analysis of the swirling strength value and following analysis of the velocity vector field. For that purpose, each plane coded by the swirling strength criterion is analyzed for local maxima, which are used for a first guess in the vortex center estimation. The exact position results from the w-velocity profile in the vicinity of the local maxima. A characteristic of the developing rollers is that the main axis of rotation is in spanwise direction and that the direction of rotation is clockwise. The condition for a clockwise rotation is $w_1 > w_2$ as shown schematically in figure 4.12 on the left. Furthermore, the figure shows important properties describing a roller. The vortex diameter D_{vortex} is defined as the spatial distance between local velocity maxima and minima. The center of the vortex is then defined at half the diameter. Furthermore, the velocity at the center position describes the convection velocity of the vortex. A characteristic instantaneous velocity signal from region I in the vicinity of a detected vortex is shown in figure 4.12 on the right. The characteristic velocity signal clearly describes a rotating vortex.
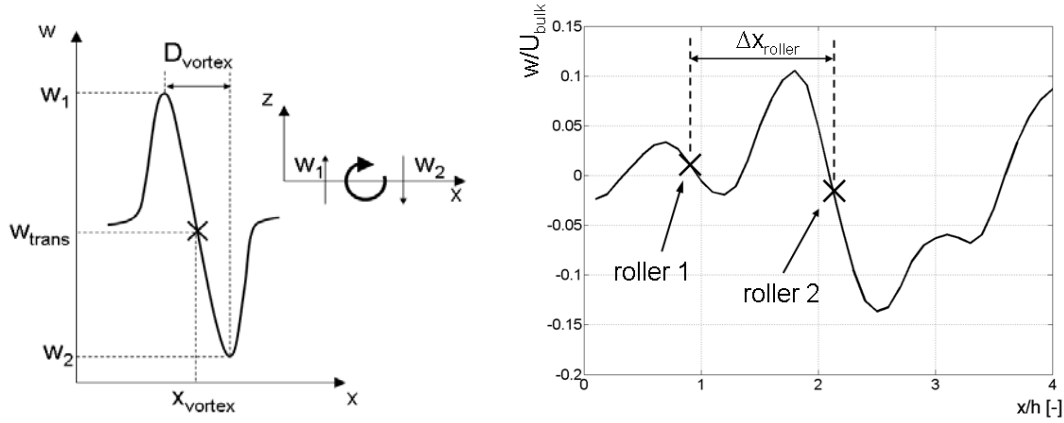
Fig 4.12 (left) Characteristics of a roller and **(right)** v-velocity profile along x/h positioned in the center of detected vortices estimated by the swirling strength criterion; vortices have streamwise displacement Δx$_{roller}$

The spatial connection of vortex centers to a vortex center line is performed via plane-wise connection of local maxima following the definition that the vortex center line is the connection of plane-wise local maxima with similar properties. Beside the spatial position, properties are e.g. vortex diameter, rotational velocity or rotational direction. The principal is shown in figure 4.13 on the left. The spanwise displacement of the planes is 0.1h. The connection of center positions follows quality criteria similar to PTV [66]. Starting with a vortex center in plane$_y$, the next position is searched in plane$_{y+1}$. In a first step, the nearest neighbour is chosen. If ambiguities arise, the vortex diameter is chosen for quality criteria. Two reconstructed vortex lines at an arbitrarily chosen instant in time are shown in figure 4.13 on the right. Two corresponding planes colour coded with the swirling strength criterion are included for orientation. It should be noted, that the chosen vortex lines are rather long (≈ 4h) and all other detected lines are removed. The raw dataset after vortex line detection is full of short vortex lines, which may be other vortices or artefacts as the vortex line detection is rather sensitive. This is obvious, as the center line results from local maxima of data, which is derived from the gradient of the velocity field. Thus, there are many operations, where uncertainties are introduced or amplified. Thus, for further investigation a threshold of 0.5h is chosen for the length of a vortex line trying to exclude noise (or maybe other vortices). Vortex lines with less than the threshold are removed from the dataset. The threshold is chosen to be slightly lower than half the expected wave length (see figure 4.8). The last step is the spatial smoothing of vortex lines via moving spline interpolation.

A first interpretation can directly be drawn from figure 4.13 on the right. The vortex lines are not characterized by straight lines as valid in a laminar flow, but by a wavy structure

similar to that of the investigated shear layer (see figure 4.8). Furthermore, the first roll up happens at varying x-positions in y-direction generating three-dimensionality immediately downstream of the step.
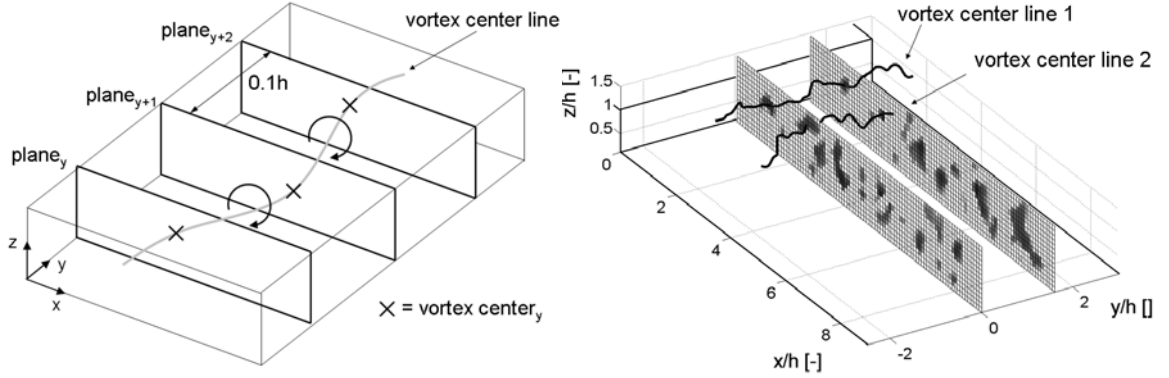
Fig 4.13 (left) Conceptional reconstruction of a three-dimensional vortex tube (roller) **(right)** Reconstructed vortex center lines. Vortex line in the range 0<x/h<4. Streamwise planes are colour coded by swirling strength

Roller Structure

The further investigation of the rollers is performed similar to that of the shear layer. The classification is performed in terms of wave length, amplitude and convection velocity. Important definitions regarding the spatial structure of the vortex center line are shown in figure 4.14 on the left. The vortex center line is shown in an isometric view. Furthermore, the 3D center line is projected into the xy-, xz-, and yz-plane. For further analysis, the 2D lines are smoothed using a rather high smoothing parameter (dashed, red line). This is necessary to exclude small scale distortions on the line for extracting only large scale length scales higher than 0.5h. Nevertheless, relevant parameters can be estimated from the smoothed line. As the vortex center line of the rollers is oriented in y-direction, a wave length in x- and z-direction is calculated. The corresponding amplitudes for a guess of the strength of distortion are calculated as shown in figure 4.14 on the left. The probability density functions of the wave lengths λ_{y-x} , λ_{y-z} of the rollers in region I are shown in figure 4.14 on the right. In comparison to the PDF of the wave lengths of the shear layer, the measured values show a large scatter. A Gauß-fit is chosen to estimate the most probably wave lengths resulting in $\lambda_{y-x}/h=0.75$ and $\lambda_{y-z}/h=0.85$. Furthermore, the PDFs show that larger wave lengths are more probable in z-direction than in x-direction showing an asymmetry in the single directions. Compared to the wave lengths of the shear layer (see figure 4.8), the most probable wave lengths of the rollers are slightly lower than that of the shear layer.
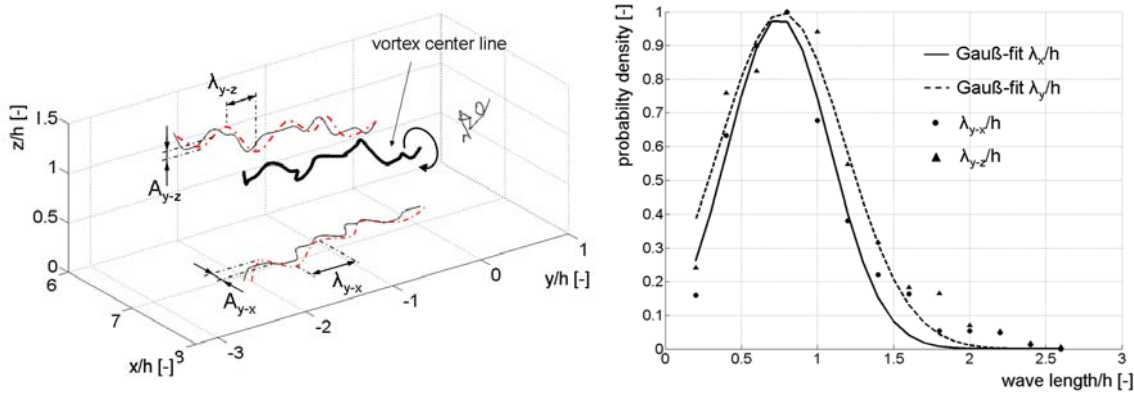
Fig 4.14 (left) Definitions for classification of vortex center line in the range 0<x/h<4; solid black line: 3D vortex center line, dotted lines: projection of 3D line into single planes, red dotted: smoothed 2D vortex center line **(right)** probability density function of single wave lengths of the roller in y-direction. Black dots: measured points, black lines: Gauß-fit

The wave lengths and amplitudes as a function of streamwise distance are shown in figure 4.15 for a temporal average of $\Delta t^*=100$ ($\Delta t =2s$). The figures are generated by mean values of the properties calculated in ten sections (starting positions: x/h=0.75, section length: 0.5h, step width: 0.5h) and following moving cubic spline interpolation.

Region I ($0\leq x/h\leq 3.5$) is characterized by increasing wave lengths and amplitudes. Immediately after vortex roll up (x/h≈1) the roller already describes a wavy line. Here, wave lengths in x- and z-direction are in the same range. In contrast, the amplitude in x-direction is larger than the amplitude in z-direction. With increasing downstream distance, the wave lengths in both directions similarly increase to about the step height. In case of the amplitudes a difference is observed. The amplitude in x-direction is largely amplified up to x/h≈3.5 being about 20 % of the corresponding wave length. The amplitude in y-direction increases only uo to x/h≈2 being nearly constant with further downstream distance up to x/h≈3.
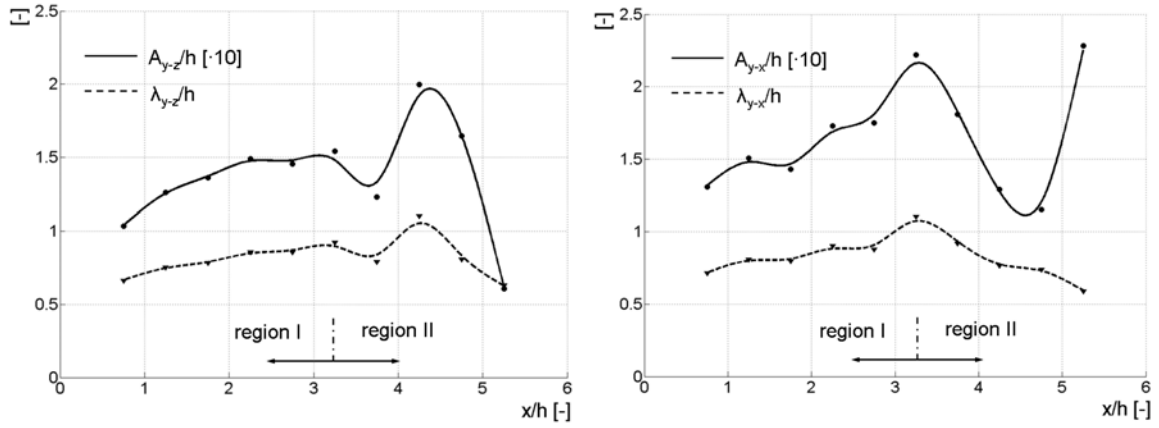
Fig 4.15 (left) Vortex center line properties in yz-plane as a function of x-direction for 0.5≤x/h≤5.5; **(right)** Vortex center line properties in yx-plane as a function of x-direction for 0.5≤x/h≤5.5; solid line: amplitude, dashed line: wave length; for plotting, the amplitude is multiplied by 10

The following conclusion is drawn and sketched schematically in figure 4.16.: the roller is distorted immediately after genesis. The wave lengths of the rollers are similar in both directions, whereas the amplitude in x-direction is larger. With increasing downstream distance, the wave lengths in both directions increase, thus showing that the properties of the wave lengths are similar in both direction. A large difference is found in the amplitudes in the single directions. Immediately after birth, the amplitude in x-direction is larger than that in z-direction. This discrepancy grows further with downstream distance. The physical interpretation is that the streamwise vortex loops of the rollers are stretched (increasing amplitude) in streamwise direction due to the main flow in streamwise direction. The vertically aligned vortex loops (amplitude in z-direction) is bounded by the separation bubble resulting in a constant amplitude of the vortex loops in z-direction in the range 2<x/h<3.
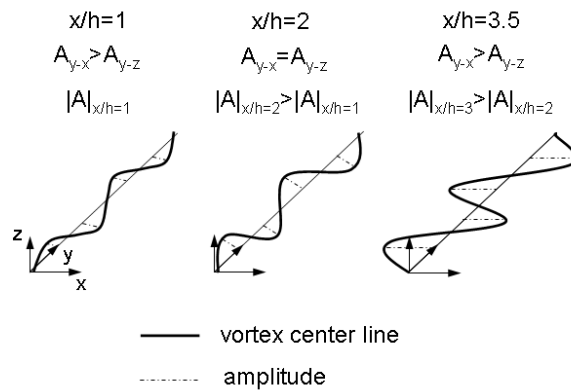
Fig 4.16 Model of change of spatial structure of vortex center line as a function of streamwise distance, deducted from the results presented in figure 4.15

Roller Orientation

In course of the analysis, a dominant feature of roll up is observed: inclined vortex formation. Figure 4.17 on the left schematically shows observed configurations in the top view. All following descriptions are with respect to the orientation of the step edge. Thus, the configuration top left describes parallel roll up, the middle and bottom left configuration inclined roll up, top and middle right convex and concave roll up. The configuration bottom right is omnipresent. It describes multiple piecewise roll up, where the single pieces vary largely from single to several step heights. In the following, we will focus on linear configurations, i.e. parallel and inclined vortex roll up. For that purpose, the figure on the right defines the inclination angle of the rollers. The figure shows the projection of three independent vortex lines in different colours. The dashed lines show the approximated orientation of the rollers resulting in the inclination angle α with respect to the step. The calculation of the inclination angle is performed via a linear least squares fit. Vortex lines with lengths below 2h are excluded from the calculation. This is for the reduction of erroneous calculated angles as short vortex lines are sensitive to inaccurately calculated positions in x-direction.
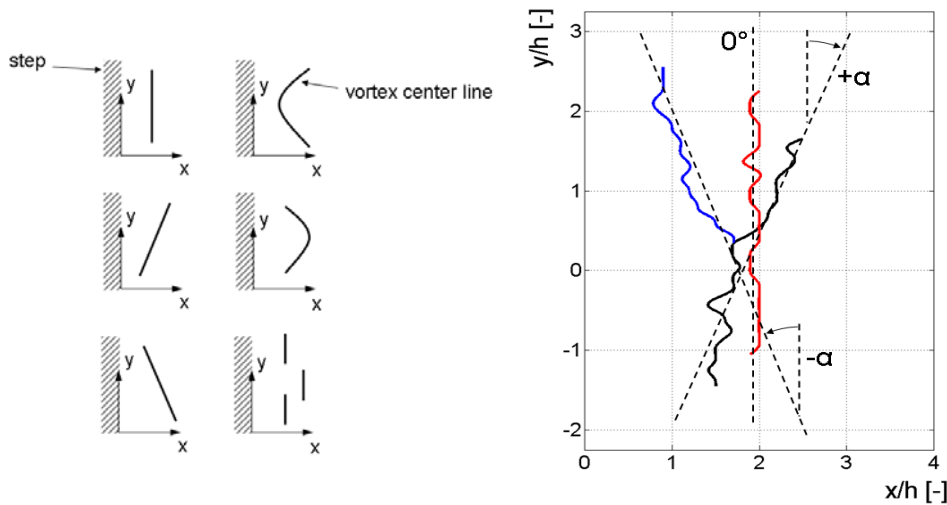
Fig 4.17 (left) Definition of roll up configurations: left top: parallel roll up, middle/bottom left: inclined roll up, top/middle right: convex/concave roll up, bottom right: piecewise roll up **(right)** Definition of inclination angle: blue: negative inclination, red: zero inclination, black: positive inclination

The PDF of the inclination angle is shown in figure 4.18. The figure shows the measured points for a time sequence of Δt* = 100 (Δt = 2s). The curve describes a Gaussian fit, showing that the gradient of the Gaussian function fits pretty well, but not the maximum peak. The distribution is centred on 0° being the most probable inclination angle. Nevertheless, inclination angles of ± 20° are observed with a probability of 25%. The PDF

indicates the necessity of spatial analysis for the understanding and interpretation of the BFSF, which was not covered by former measurement techniques (pointwise or planar).
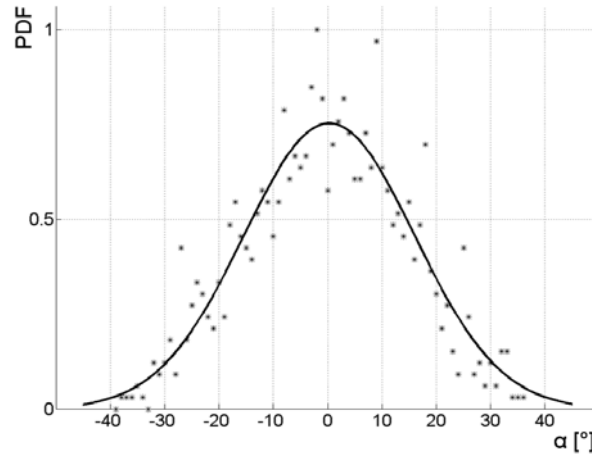
Fig 4.18 Probability density function of the inclination angle of the rollers; dots: measured points, black line: Gaussian fit

Roller convection

The convection of the rollers in downstream direction is shown in figure 4.19 via two instants in time separated by normalized time $\Delta t^*=1.41$. The black lines represent instant 1 and the gray lines instant two. Two rollers are captured by the vortex criteria at roughly $x_1(t_1)/h=1$ and $x_2(t_1)/h =2.2$. Furthermore, missing pieces of vortex lines are shown in figure 4.19 on the right making the analysis rather difficult as a choice is necessary, if missing pieces result from inaccurate data or from fluid-mechanical events influencing the vortex line.

Nevertheless, the convection of the rollers is clearly visible. The rollers travelled a variable distance with respect to the streamwise and spanwise direction. A mean convection velocity averaged over the width is calculated for the present configuration to $v(x_1)/U_\infty=0.28$ and $v(x_2) /U_\infty=0.42$ showing the acceleration of the rollers in downstream direction. This is validated by detected rollers at about x/h=4 having even larger convection velocities of $0.56U_\infty$. The vortex line at $x_1(t_1)/h=1$ describes an approximately parallel roll up of a wavy shear layer. At time instant 2, the vortex line seems to have stayed at the same position at about y/h=0 while travelling in downstream direction for y/h<0. Thus, the vortex line describes the development of a parallel to an inclined roller.
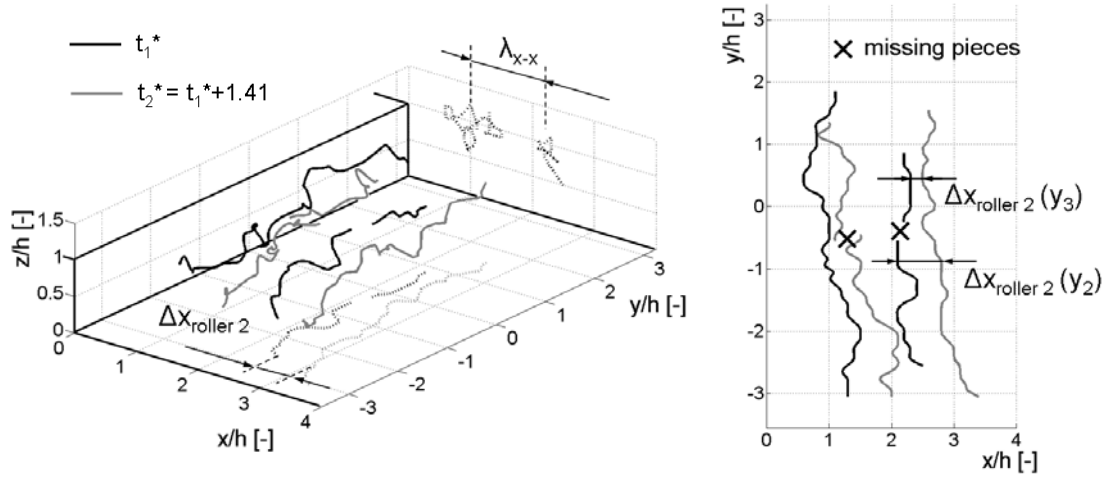
Fig 4.19 (left) Isometric view of vortex line convection; black line: t1*, gray line: t2*, solid line: 3D line, dotted line: 2D projections of 3D vortex center lines. **(right)** top view of the situation left

The shedding frequency of the rollers is calculated via an FFT of the w-velocity signal at a constant (x/h =1.2, y/h=0, z/h=1.1). The w-velocity signal is chosen as the characteristic property of the vortex roll up (see figure 4.12). The position is chosen to be in the region of interest, where vortex roll up occurs. In total, a period of $t^* = 600$ ($t = 12s$) of the time resolved measurements is analyzed. Figure 4.20 shows the FFT of the signal. The peak in the FFT is at 11.4 Hz, which corresponds to a Strouhal number for vortex shedding of St_{VS}=0.24 based on the step height. Beside Metais et al. [87], several authors calculated a Strouhal number of roughly 0.2, which is in good agreement with the results obtained here.
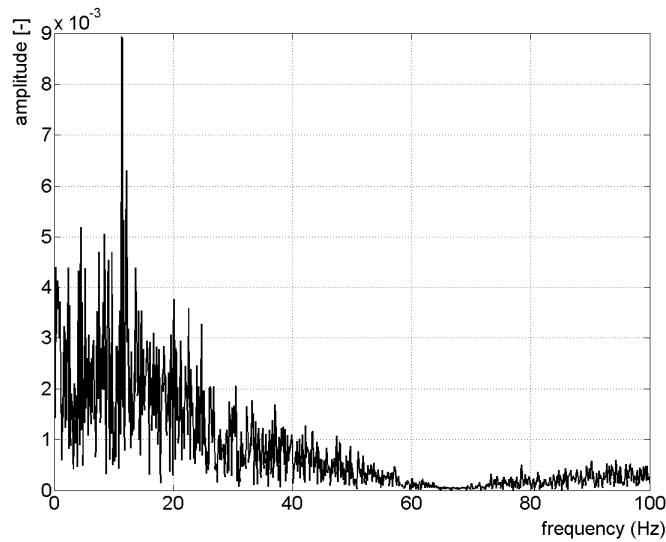
Figure 4.20 Fast Fourier Transformation (FFT) of w-velocity signal at (x/h =1.2, y/h=0, z/h=1.1) to extract the vortex shedding frequency

Shear layer structure vs. roller structure

Detected shear layer and detected rollers are shown simultaneously in figure 4.21 for one instant in time. Immediately downstream of the step, the shear layer describes a wavy structure. Vortex roll up happens due to high shear gradients at roughly x/h=1. The vortex line is already distorted. The second vortex line describes a convected roller. By visual inspection it is obvious that distorted vortex lines are primarily connected to the distorted shear surface. The vortex lines follow heights and ridges of the shear surface.

With respect to the statement that vortices are born, where high shear is apparent as stated by Schafhitzel et al. (2010) [120], this thesis proposes that the distorted vortex line is the results of the wavy shear surface immediately downstream of the step. The common opinion about the principal process regarding the vortex roll up is that the roll up occurs along a linear line [129]. The condition for such a regular roll up is a smooth and straight shear surface. This is probably true in the laminar separation regime (see figure 3.6 on the right), but not in the transitional to turbulent separation regime. As shown in figure 4.9 the shear layer has a wavy structure immediately downstream of the step. Thus, as the rollers develop due to high shear, it is rather natural that the spatial structure of the roll up is a distorted line.
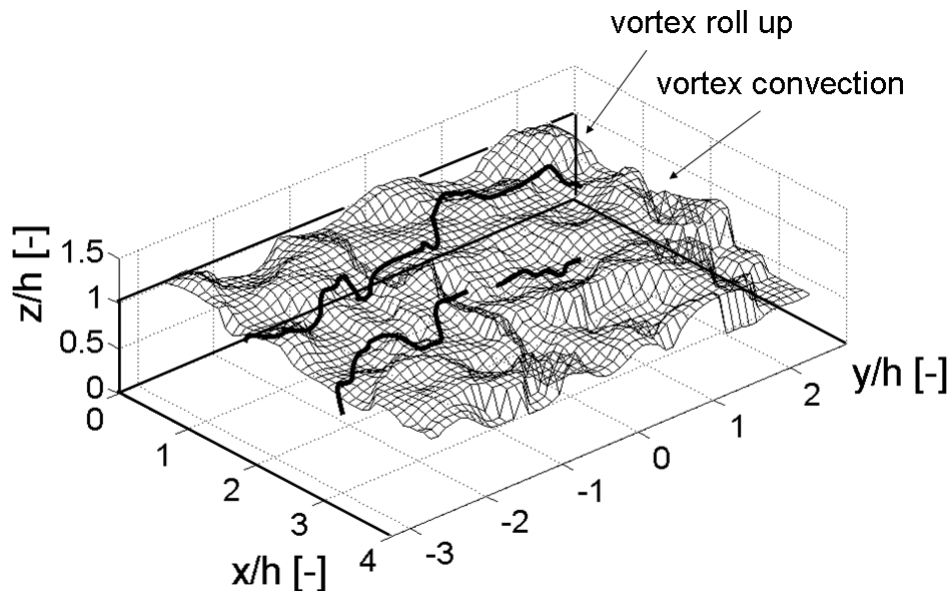
Fig 4.21 Interaction of shear layer (surface) and vortex center line (black line) in the range 0<x/h<4

The physical reason for the waviness of the shear layer is not yet clear. Two possible explanations can be given: The waviness may be generated due to the unsteady flow below the shear surface in the vicinity of the step (region V) and/or the waviness may result from perturbations originated in the boundary layer upstream of the step. As shown later, the

intensity of the recirculation flow in region V has only velocities of 5% of the free stream velocity. Thus, higher influence is expected from the turbulent boundary layer, which is convected in free stream direction. Furthermore, the initial state of the boundary layer is stated in literature as a main influence on the characteristic behaviour of the BFSF (see figure 3.6) supporting the hypothesis that the waviness in y-direction results from the initial state of the boundary layer. An analysis of spanwise planes shows secondary flow structures as investigated by Scarano et al. (2001) [112]. The authors connected these secondary vortices with the appearance of Λ-vortices resulting from the turbulent inflow. Further investigations about the separation of coherent structures from the upstream boundary layer are necessary.

4.2 Region II: Vortex Convection

Region II (3<x/h<9) is characterized by a highly unsteady flow regime full of local stagnation points and complex vortex dynamics. The flow evolution is shown in figure 4.22 via LIF for a period $t^* \approx 9.4$. The red dotted line represents the tracking of one exemplary roller. The sequence shows an "undisturbed" development of a roller without large external perturbations. In terms of the categorization shown in figure 4.4, the flow is damped at the beginning of the sequence and becomes regular at the end of the sequence. The shear layer roll up happens in the range 0<x/h<3 (t_0). Later in the sequence, the roller starts to develop and is transported in downstream direction. At t_5 the roller builds a large scale structure positioned around x/h=4. Here, the roller starts to interact with the bottom wall resulting in a breakdown of the regular structure within about three time steps (t_5-t_8). The breakdown is finally documented by the loss of concentrated rhodamin. Sudden loss of concentration is due to increased turbulent mixing as omnipresent in structure breakdown. The spatial hull of the roller is still observable at t_{10}. The analysis of the time resolved measurements showed that the rollers have lost most of their rotational energy at t_{10}.

Roller development

In region II, the distortions of the vortex lines (in the following loops) are highly amplified as extractable from figure 4.15. The principal three-dimensional structure of the rollers is shown in figure 4.23 via a schematic vortex center line for varying streamwise positions. The basic of the following description is found in figure 4.15. Immediately after vortex roll up the vortex center line is slightly distorted due to the wavy shear layer. With
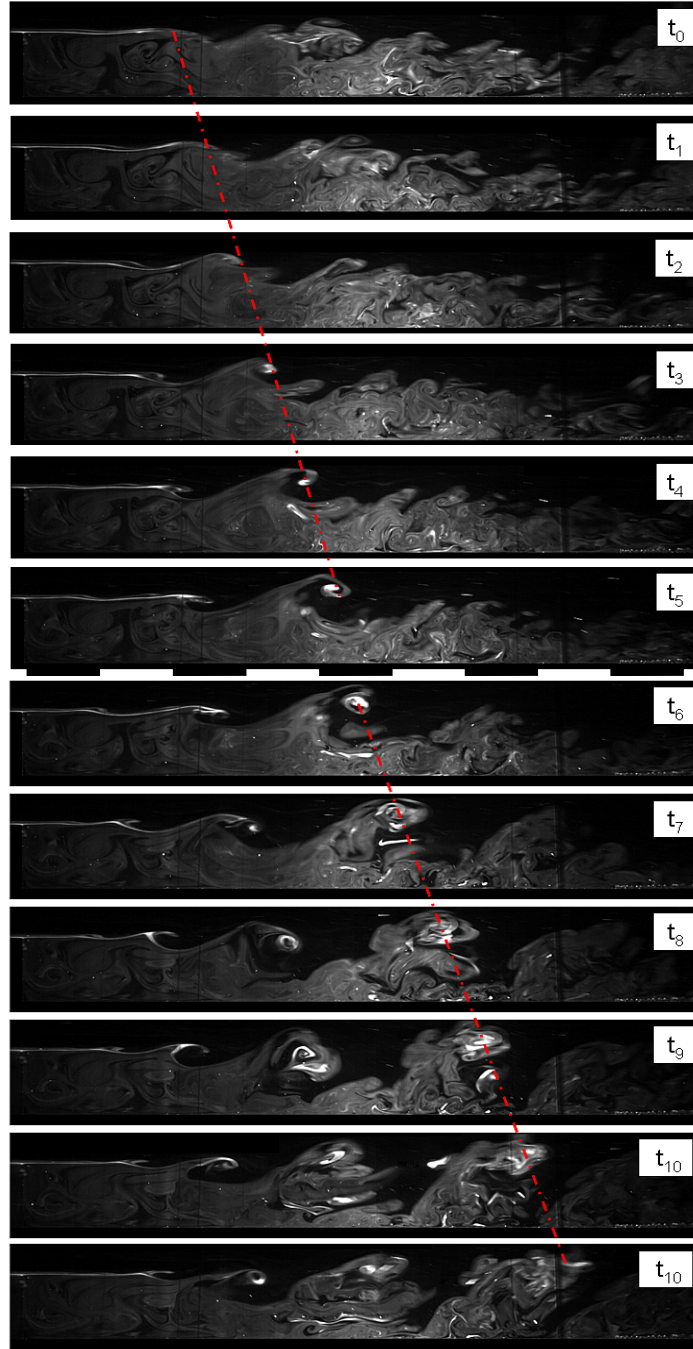
Fig 4.22 Development of rollers without external disturbances; separation time: $\Delta t=20$ ms ($\Delta t^*=0.94$); total length of sequence: $t\approx200$ms ($\Delta t^*\approx9.4$)

increasing distance, the vortex loops are stretched in downstream direction resulting in roughly 30% higher amplitudes of the vortex loops in x-direction compared to the z-direction at x/h=3.5. This is concluded to be the result of the primary streamwise directed shear velocities. In the range 4<x/h<5, the vortex center line performs a rapid deformation to a structure, where the vortex loops are primarily oriented in z-direction ($A_{y-z} \approx 1.5A_{y-x}$). The vertical alignment of the vortex loops again vanishes in the range 5<x/h<6. Here the rollers start to interact with the bottom wall. Thus, the vertical aligned vortex loops are again re-oriented in horizontal direction forced by the presence of the bottom wall.
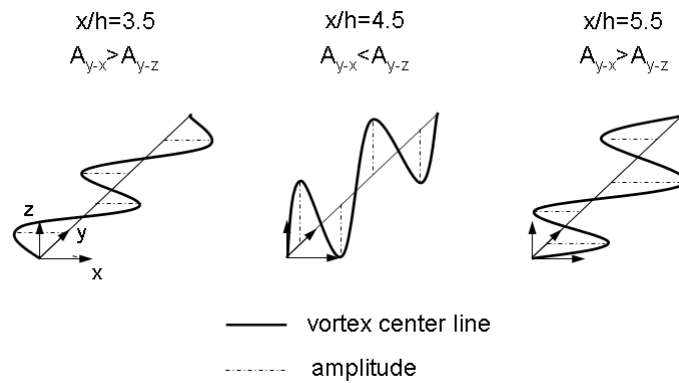
Fig 4.23 Model of change of spatial structure of vortex center line as a function of streamwise distance, deducted from the results presented in figure 4.15

Influences on roller development

Several mechanisms might explain the re-orientation of the dominant vortex loops of the rollers: roller pairing or merging events (a), roller induction effects (b) and/or interactions with recirculation region (c).

a) In literature, the range 3<x/h<6 is closely connected to complex vortex pairing events as observed in free mixing layers [131]. As already discussed, the plateau and following increase in shear layer thickness (figure 4.7) between 3<x/h<6 is comparable to that of a free mixing layer [47]. The development of coherent structures in a turbulent mixing layer is observed by Roshko (1976) [111]. A picture is drawn, where neighboured (in streamwise direction) rollers in the fully developed shear layer start to rotate around each other and merge into a single but larger vortex. The vortex pairing/merging events result in large thickening of the boundary layer thickness. As discussed earlier, the shear layer in the present BFSF is not fully developed. This was concluded with respect to the required length for a shear layer to reach a fully developed state [1]. Vortex pairing events as described in [111] are not observed. Nevertheless, as the distance between the rollers is

in the range $\Delta x/h=1$ +/-0.5 (see figure 4.19), there might be a distinct interaction between neighboured rollers.

b) Muller et al (1982) [90] connect complex merging events with respect to the Biot Savart law as shown in figure 4.24. The curved vortex tube generates three-dimensionality by inducing velocities on itself resulting in distortions of the vortex line. Furthermore, a vortex loop bent in upstream direction is affected by induced velocities of downstream directed loops of a successive roller in such a way that the upstream vortex loop is transported in vertical direction. It should be noted that this scenario has been drawn via flow visualization experiments.
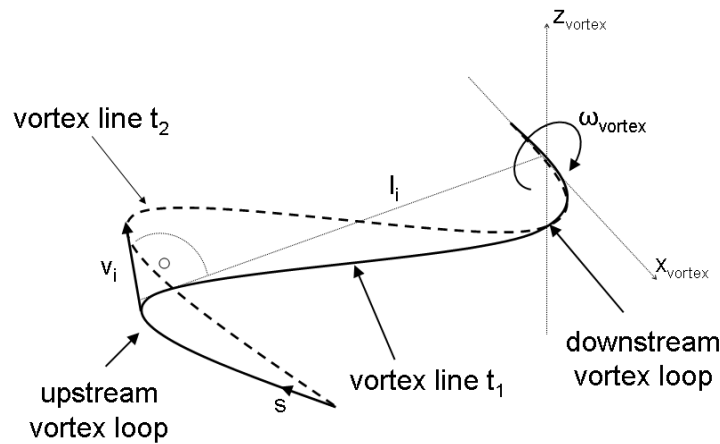
Fig 4.24 Biot-Savart law applied to a curved vortex line; solid line: original vortex center line, dashed line: distorted vortex center line due to induced velocity v_i by vorticity ω_{vortex} at position s along the vortex center line.

c) Small scale turbulent zones resulting from impingement are made responsible for turbulence in the recirculation flow by Pronchick (1983) [102]. These zones influence the oncoming rollers and lead to structural roller breakdown events in the range $3<x/h<6$. A typical scenario of large scale coherent structures in the recirculation area influencing oncoming rollers is shown in figure 4.25. The figure shows the vector plot of the symmetry plane from the PIV measurements. The vectors have uniform length to focus on the direction of the flow. The magnification shows a vortex interaction scene resulting in a vertical perturbation originating from the recirculation region. The convection direction of roller 1 is in downstream direction. Roller 2 generates upstream directed velocity resulting in a local saddle point marked by a cross-style marker. In this point three-dimensionality is generated resulting in vortex center line distortions and consequently in instabilities.

From the own results it is concluded that vertical perturbations from the recirculation zone are the primary mechanism leading to a change of orientation of the vortex loops from

horizontal to vertical orientation. This is for two reasons: a) If the Biot Savart law had a dominant influence, the re-orientation should be a continuous process and should also be observable at positions in upstream direction. b) An indicator for the influence of the recirculation area is observed by the development of the lower shear layer thickness (figure 4.7). In fact, chapter 4.4 will show that the vortex loops generate vortices, which are transported into the recirculation area and interact with the oncoming rollers. Thus, it can be concluded that roller breakdown doesn't happen naturally due to long term instability, but due to short term perturbations. With respect to figure 4.7, the perturbations influencing the shear layer development originate from the recirculation area. This is concluded due to the increasing lower shear layer thickness in the range 4<x/h<6.
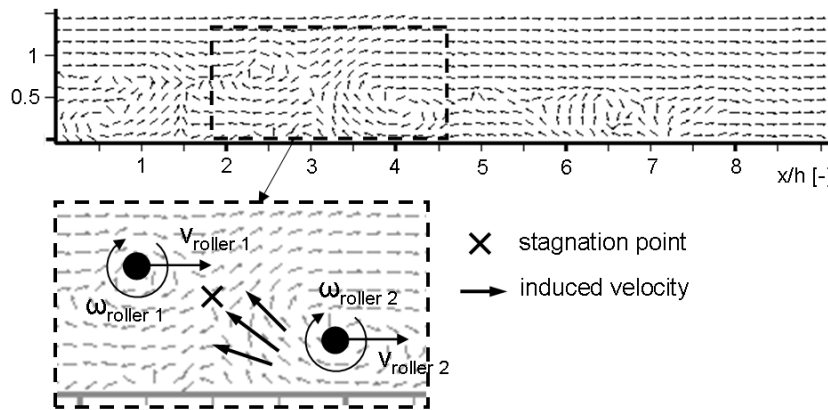
Fig 4.25 (top) Instantaneous vector field in the symmetry plane; vectors have constant length to indicate flow direction. **(bottom)** Zoom into of short term perturbation. Scenario is sketched for clarity.

4.3 Region III: Reattachment

The spatial expansion as well as the temporal behaviour of the integral length scale reattachment line is in the focus of this chapter. Open questions are discussed as: what is the spatial structure of the reattachment line, what is the reason for the spatial structure and what causes the fluctuation of the reattachment line? First, the reattachment position in terms of time resolved planar measurements is discussed and compared with literature. Next, the spatial structure of the reattachment line will be pointed out showing that the planar investigation is not sufficient for the analysis of the reattachment location and for the interpretation what forces the fluctuations of the reattachment line. At the end, the interaction of shear layer rollers with the reattachment line is investigated. This is possible for the first time due to the volumetric measurement technique.

Reattachment: Characteristics of xz-plane, y/h=0

As discussed earlier, measurements of the BFSF were primary performed in streamwise symmetry planes or via wall pressure measurements. Here, a sawtooth pattern in the temporal progress of the reattachment position is observed. This is that the reattachment length constantly grows in size and suddenly shrinks as discussed in chapter 3.

The analysis of the time resolved measurements showed that the definition of the reattachment point described in figure 3.4 is not sufficient for the description of the dynamic behaviour of the reattachment point. Figure 4.26 shows a normalized instantaneous velocity profile in the streamwise symmetry plane (y/h=0) at z/h=0.1. There are two recirculation regions, a regular one and a separated one. Thus, two reattachment points are introduced. The one defined by the regular recirculation region x_{r11} and the one defined by the separated recirculation region x_{r12}.
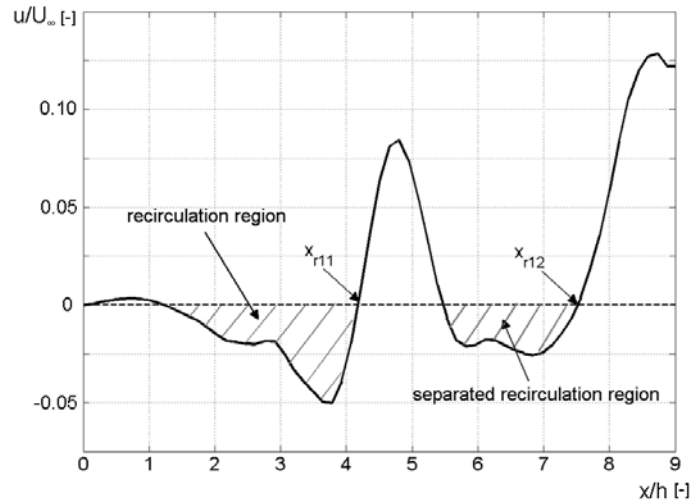
Fig 4.26 Definition of recirculation region and separated recirculation region of the instantaneous flow field

The calculated reattachment length of the reattachment points x_{r11} (black line) and x_{r12} (red line) obtained by the time resolved planar PIV measurements is shown in figure 4.27 for a period of Δt=6s (Δt^*=282). Furthermore, exemplary vector fields colour coded with streamwise velocities are shown describing characteristic scenarios. The negative streamwise velocity is blanked. Thus, white areas represent recirculating flow.

The progress of the regular reattachment point shows a quasi-periodic characteristic. The point constantly moves downstream and suddenly breaks up in two parts. A quasi periodic frequency is obtained by counting the events resulting in 4 events/s. This corresponds to $St_{re,2D}$=0.09. The reattachment point of the separated recirculation region differs slightly from the regular one. At positions, where x_{r11} suddenly jumps upstream, x_{r12} constantly

moves further downstream followed by a sudden jump back to the streamwise position of x_{r11}. The evolution of both reattachment points indicates the cyclic release of parts of the recirculation region in downstream direction. A classification of the separated regions is performed via the distance between x_{r11} and x_{r12}. For that purpose, large gray shaded areas represent large scale separation of low frequency and small gray shaded areas represent small scale separation of high frequency. Snapshot a) shows the visual representation of the flow field for large scale separations. It is characterized by separation of large recirculation region ranging up to several step heights. Snapshot b) shows the scenario, where the recirculation region is continuous. Here, both reattachment points are overlapping. Snapshot c) shows the characteristic situation of small scale separation. Here, small parts with backflow are (<1h) separated from the recirculation region.
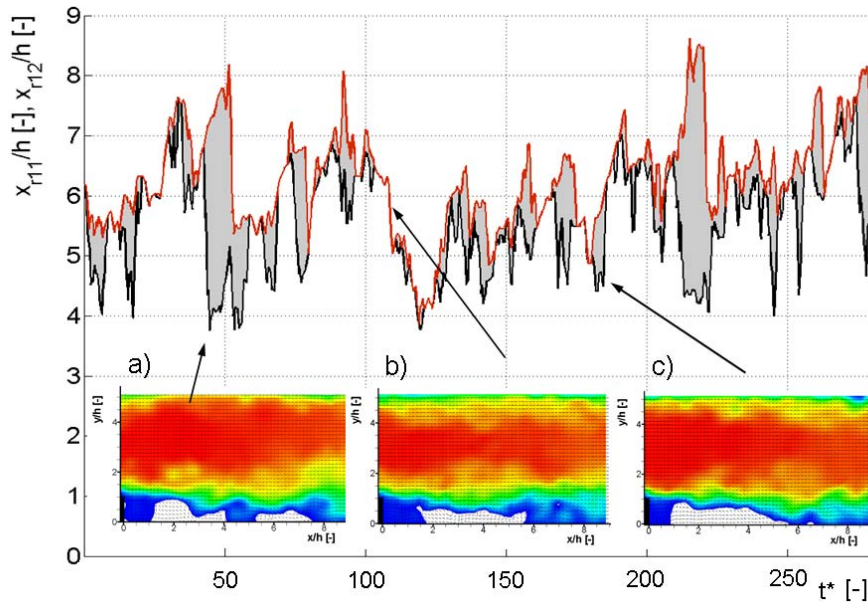
Fig 4.27 Regular reattachment point x_{r11} (black line) and separated reattachment point x_{r12} (red line) as a function of normalized time t*. Vector fields are colour coded with streamwise velocity. Negative streamwise velocities are blanked. a) large scale separation of recirculation region b) continuous recirculation region c) small scale separation of recirculation region

The corresponding characteristic sawtooth pattern is highlighted in figure 4.28 by red lines. The figure shows a time sequence of $\Delta t^*=100$ of the regular reattachment point. The figure on the left shows the reattachment point obtained by the PIV measurements and the figure on the right shows the results obtained by 3D Scanning PTV. Both figures show the reattachment point x_{r11} in the symmetry plane as a function of time. The reattachment point is characterized by a constant motion in downstream direction and a sudden jump back validating that both techniques are sufficient to resolve the temporal behaviour of the

fluctuating reattachment point. Nevertheless, it should be noted that small zones of recirculating flow downstream of reattachment with extensions less than 0.1h cannot be captured by the measurements (see chapter 2).
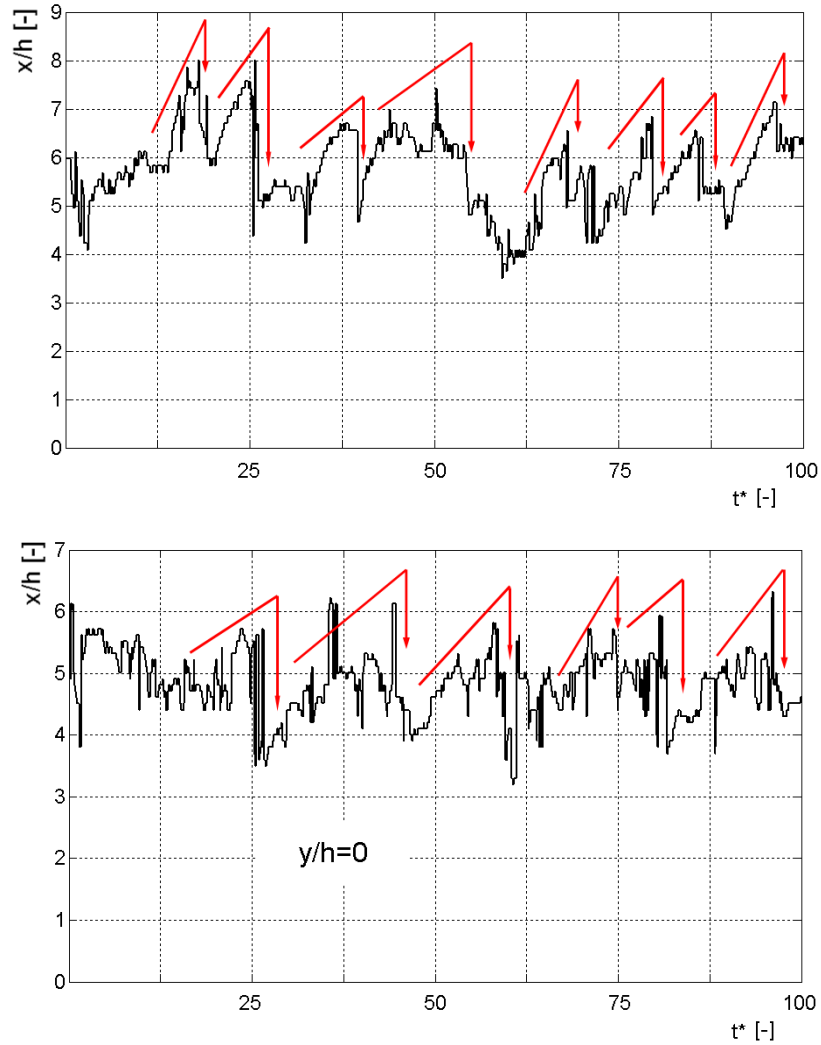
Fig 4.28 Reattachment point as a function of time. **(top)** Time Resolved PIV measurements **(bottom)** 3D Scanning PTV; the red line highlights the sawtooth pattern.

In the following we will focus on the first large scale separation between t*=40 and t*=60. This sequence shows a significant scenario, where zone of recirculation flow is released from the regular recirculation area. Figure 4.29 on the top shows the magnification of the region of interest from figure 4.27. Ten positions are marked numbered from t_1 to t_{10}. The corresponding representations in terms of the vector field are shown below. The vector fields are colour coded by streamwise velocity. Areas of backflow are blanked. Furthermore, sectional streamlines are plotted for visualisation. The sectional streamlines are calculated following a Runge-Kutta scheme.
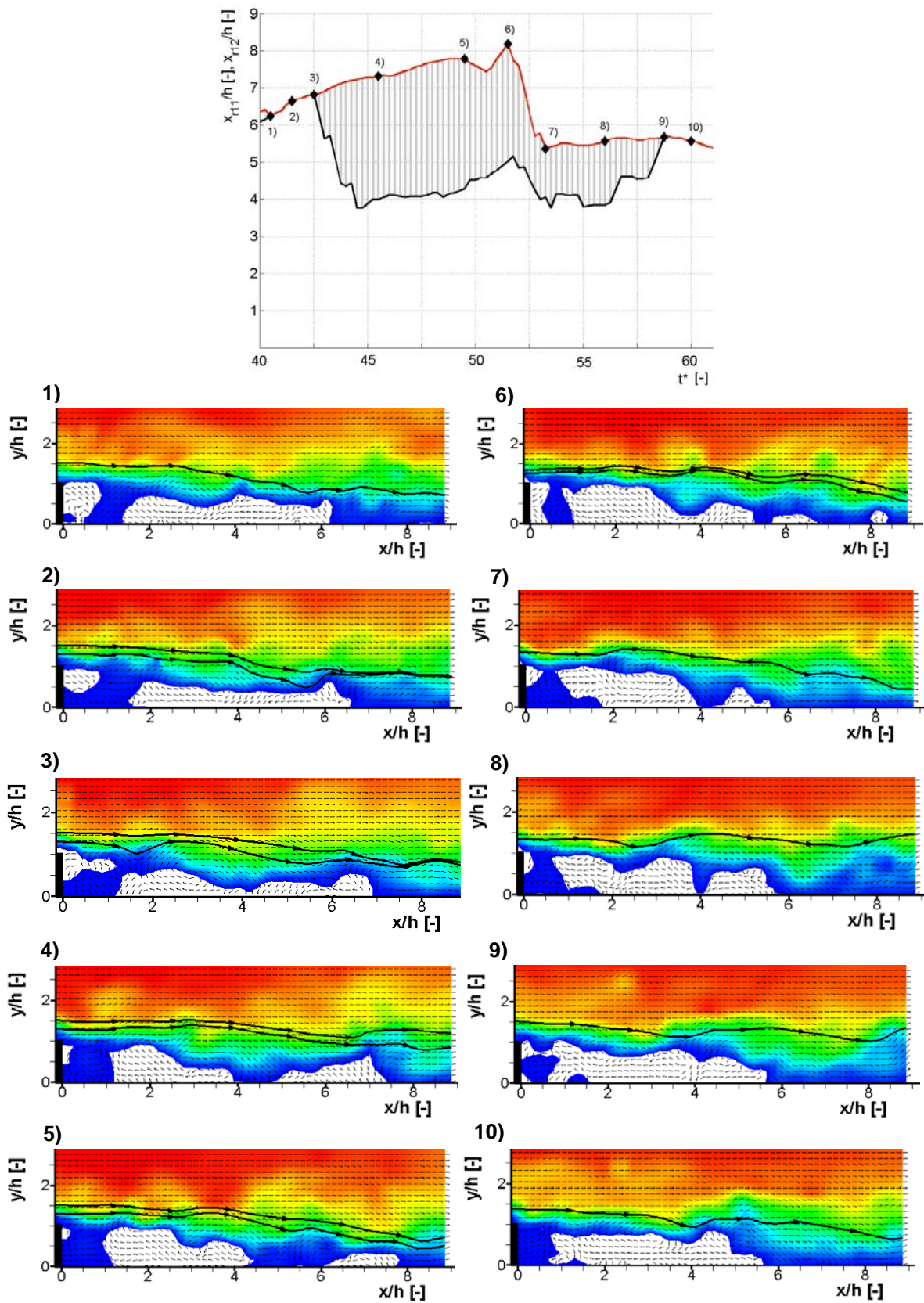
Figure 4.29 Large scale break in (mechanism 1) lengthening of recirculation region (1-3), separation of large scale recirculation region (3), downstream movement of separated recirculation region (4-5), cut in of separated recirculation region (6) and connection with main recirculation region (7-10)

The underlying vector field topology allows a qualitative detection of dominant vortical structures. Nevertheless, the early deformations of the rollers makes a vortex based analysis via planar measurements difficult as the main axis of rotation is not aligned normal to the measurement plane.

At time step t_1 the recirculation area is continuous. Both reattachment points are at the same position. Several vortices are located along the layer between forward and backward flow, whereas the aft part of the recirculation region is fixed by a vortical structure. Between t_1 and t_3 is constant growing in length of the recirculation region. This goes within the convection of the roller train in downstream direction. Connected with the lengthening is a narrowing of the recirculation region in z-direction. The reason for the lengthening is in the large oncoming vertical structure positioned about x/h=3, which generates negative velocities in z-direction resulting in a separation of the recirculation area in two parts. In t_5 and t_6 the released region moves downstream with the aft vortex. While moving downstream, the negative velocities dissipate resulting in a reduction of the size of the separated recirculation region. Furthermore, the release of the aft region forces a flapping of the streamline (t_3-t_6). In t_6 a second small separated region appears at x/h=6. This is believed to be the result of three-dimensionality as will be shown later. From t_6) to t_7) the negative velocities in the separated regions are diminished, which is simultaneous to the jump of x_{r12}. The convective velocity of the rollers downstream of reattachment has become larger than the induced negative velocities of the rollers. While convecting out of the image plane, the rollers influence the streamline pattern resulting in a large scale flapping (t_7-t_9). Furthermore, sequence t_7 to $t_9$ shows merging of recirculation regions. In t_7 the recirculation region starts to split. Nevertheless, the region doesn't shed downstream, but again connects with the regular recirculation. Again, the outer boundary of the recirculation region is fixed by a vortical structure.

From the time resolved PIV measurements, the following statements are concluded: The sawtooth pattern of the reattachment point is clearly linked to the interaction of the rollers with the wall while moving downstream. Rollers build the outer boundary of the recirculation area. Thus, while a roller is transported in downstream direction, the reattachment point moves in downstream direction, too. Backflow regions below the rollers are generated by convecting rollers. The negative velocities of the released regions are exhausted within a few step heights. The quasi-periodic release of the aft part of the separation region downstream follows St_{re}=0.09.

Limits of the planar PIV measurements are reached near the reattachment region. On the one hand zones of recirculation suddenly appear downstream of reattachment and on the other hand vortical patterns appear and disappear while convecting in downstream direction. This is thought of to be the result of the three-dimensionality.

Reattachment: Characteristics of xy-plane, z/h=0.1

The three-dimensionality about reattachment is getting clear by the investigation of the reattachment line. For that purpose, figure 4.29 shows a comparison of two instantaneous results obtained by the planar PIV measurements. The figure shows results of measurements in P5 (see figure 2.1) visualized via a vector plot and colour coding by streamwise velocity. Negative velocities in streamwise direction are blanked, thus highlighting recirculating flow. Two characteristic states are shown. The left figure describes the reattachment line as an organized structure of "fingers" (finger configuration) and the right figure describes the reattachment line as an approximately linear line (line configuration). The fingers have a spacing ranging from 1h to 2h in spanwise directions and length scales of 2h in streamwise direction. The streamwise velocities of the fingers successively change from forward flow to backward flow in spanwise direction. Beside the reattachment line, regions of backflow are observed downstream of reattachment.
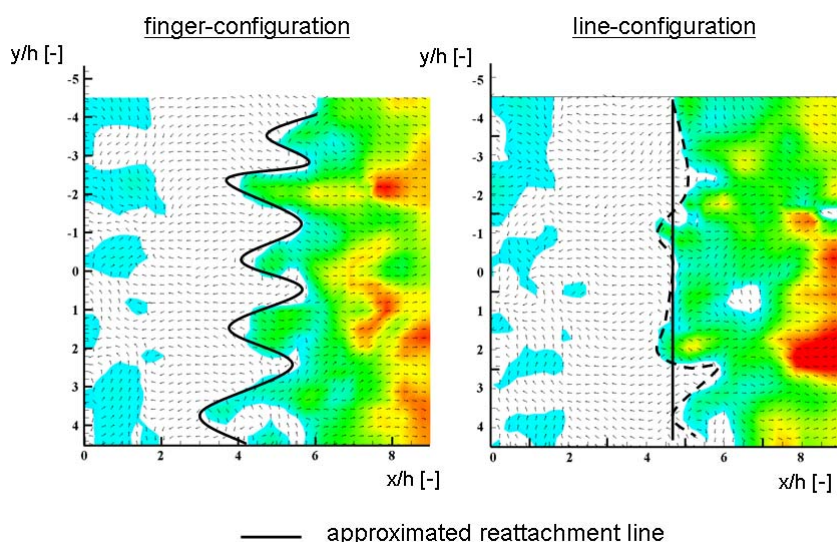
Fig 4.30 Normalized planar streamwise velocity field at z/h=0.1 obtained via Planar PIV (backflow is blanked; **(left)** finger configuration **(right)** line configuration

The characterization of the fingers in terms of dominant shape is rather difficult as there is no dominant structure, which holds for several time steps. This is more a continuous process. Due to the fingers, the reattachment length varies largely up to 3h in spanwise

direction. Thus, we define a mean reattachment line $x_{r11,mean}$ as the linear fit of the single reattachment points in spanwise direction as shown in figure 4.31 on the left. From here, the root mean square value (RMS) $\Delta x_{r11,mean}$ is defined. Thus, high values of $\Delta x_{r11,mean}$ indicate a finger configuration and low values of $\Delta x_{r11,mean}$ indicate an approximately linear configuration. The normalized values as a function of normalized time is shown in figure 4.31 on the right. The progress of the mean reattachment position (solid line) is described by a continuous increase and continuous decrease in time. The sawtooth pattern (continuous growing and sudden jump back) observed in the planar measurements is not replicated here (see figure 4.27). The reattachment location varies about 10% in time.
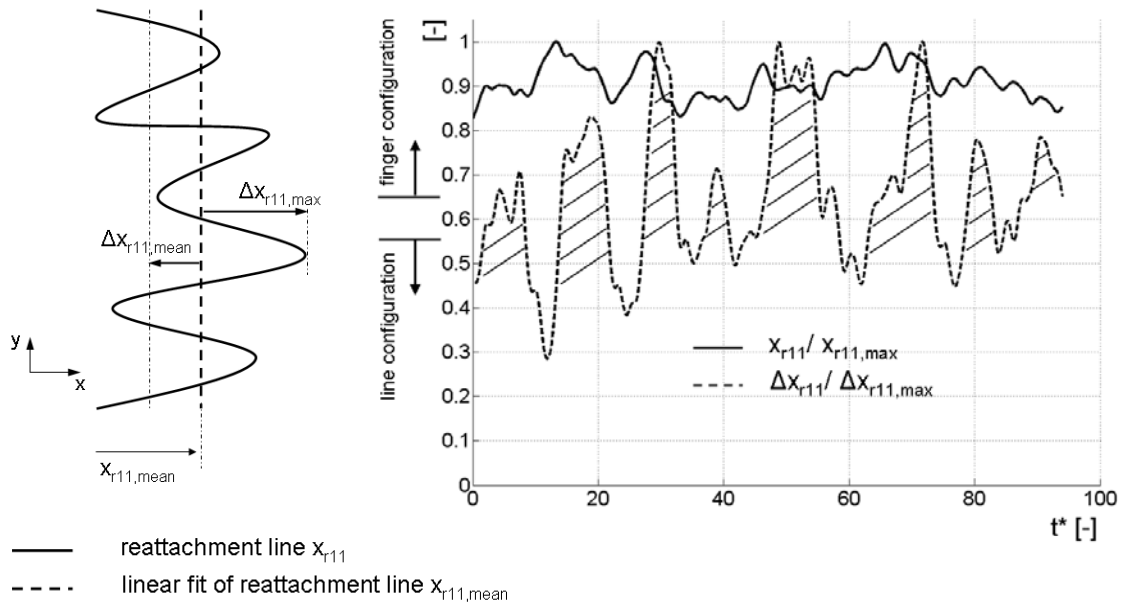
Fig 4.31 (left) Mean reattachment over the span and definitions of important parameters for detection of line and finger configuration. **(right)** Temporal signal of mean values over the span defined on the left

The comparison of the mean reattachment position with the RMS value shows a clear linkage of both. At low values of the amplitudes (line configuration), the reattachment position moves in downstream direction resulting in lengthening of the recirculation region. At a certain reattachment length, the finger configuration starts to become dominant resulting in a stop of lengthening and a subsequent shrinking of the reattachment length. The transfer from line configuration into finger configuration is rather sharp and clearly visible in figure 4.31 on the right. A quasi periodic frequency is estimated to 4 Hz ($St_{fingers}=0.09$) by counting the total amount of single finger configurations in certain time intervals. $St_{fingers}$ is similar to $St_{re,2D}$, (corresponding St-number obtained by the planar time resolved measurements) from where the conclusion is drawn that the observed frequency

of the sawtooth pattern is linked to the presence of the finger configuration. The reason for the finger configuration is searched in the presence of the convecting rollers. Nevertheless, the St-number of vortex shedding ($St_{shedding}$=0.2) is approximately twice the number of the finger configuration.
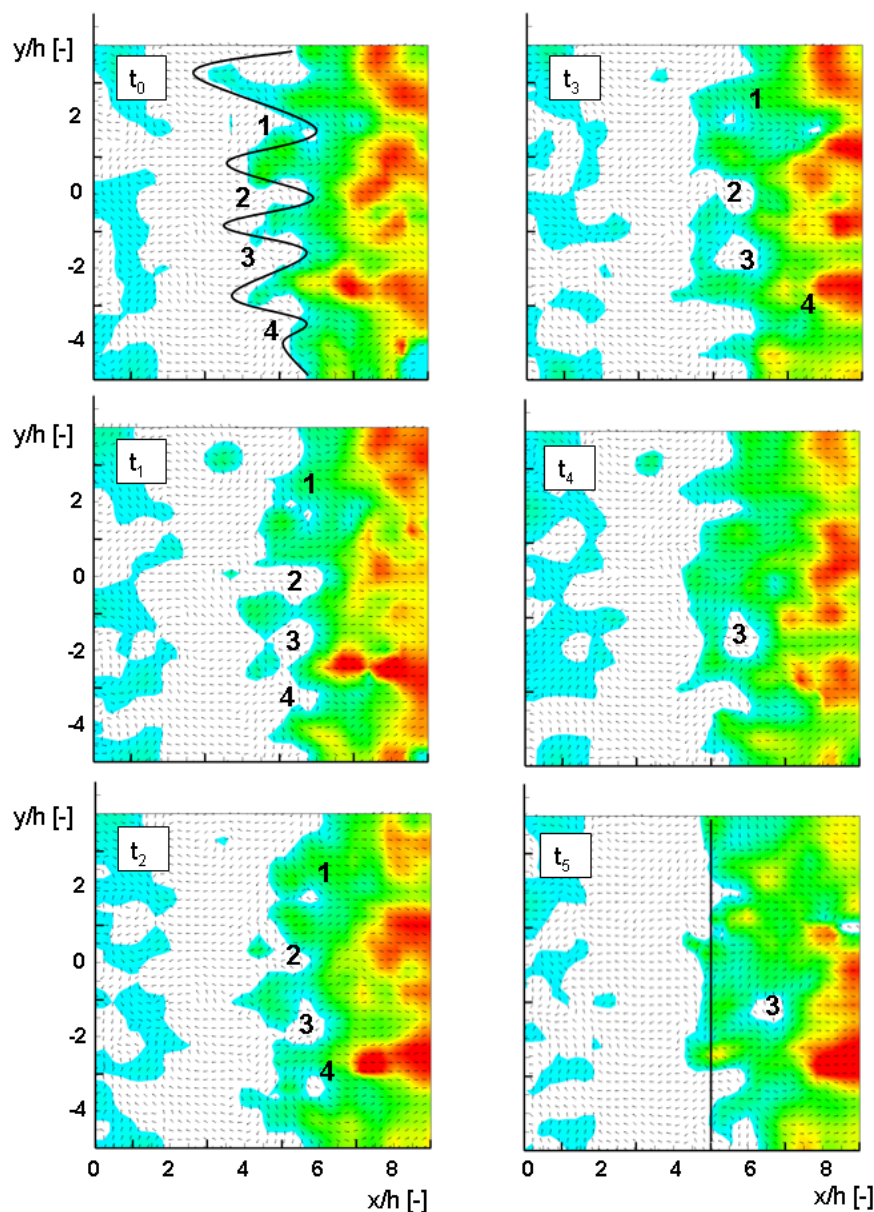
Fig 4.32 Time resolved visualization of formation of small zones of recirculating flow due to merging of fingers

The time resolved measurements show a continuous process from finger configuration into line configuration and vice versa. An exemplarily time resolved sequence is shown in figure 4.32. The figure is colour coded with streamwise velocity and backflow is blanked. A finger configuration is given at t_0. The qualitative reattachment line is sketched black highlighting the finger configuration. The single fingers are numbered 1 to 4. In the following, we will focus on finger 3. Once the fingers are generated, they immediately start

to deform at the single endings. In course of the deformation, the fingers incline with respect to the main orientation in stream wise direction and lengthen and shorten showing the instability of the finger configuration (t_2). If the fingers have a certain degree of deformation, the fingers start to merge (t_3). Due to the merging at the ending of the fingers, small zones of recirculation are engulfed by positive flow (finger 3 at t_4). Once the zone of recirculating flow is separated from the main recirculation region, the small zones are transported in downstream direction. At the end (t_5), the reattachment line is described by an approximately line configuration.

Reattachment: volumetric characterization

In the following, the volumetric measurements are used to investigate the interaction of oncoming rollers and reattachment line. The volumetric expansion of the fingers is shown for one instant in time in figure 4.33 via isosurface of the zero-velocity. The corresponding time step in figure 4.31 is about t*=18. The height of the fingers ranges up to 0.5h. Beside the main fingers, separated zones of recirculation flow are observed with similar heights. The approximated reattachment line is sketched as a black line for visualization. The rollers in the range of reattachment are represented by vortex center lines (red). The vortices are positioned around the single fingers with the main axis of rotation in spanwise direction. The vortex lines are superimposed by long scale wave lengths (1h-3h) and small scale wave lengths(<1h). The small scale wave lengths (also observed in figure 4.15) are hypothesized to be the result of vortex center line instability and are interpreted as perturbations only locally influencing the vortex center line. The large sale wave lengths describe dominant vortex loops of the rollers. The visual inspection shows that the vertically aligned vortex loops are primary positioned over the single fingers, thus engulfing the recirculation fingers.
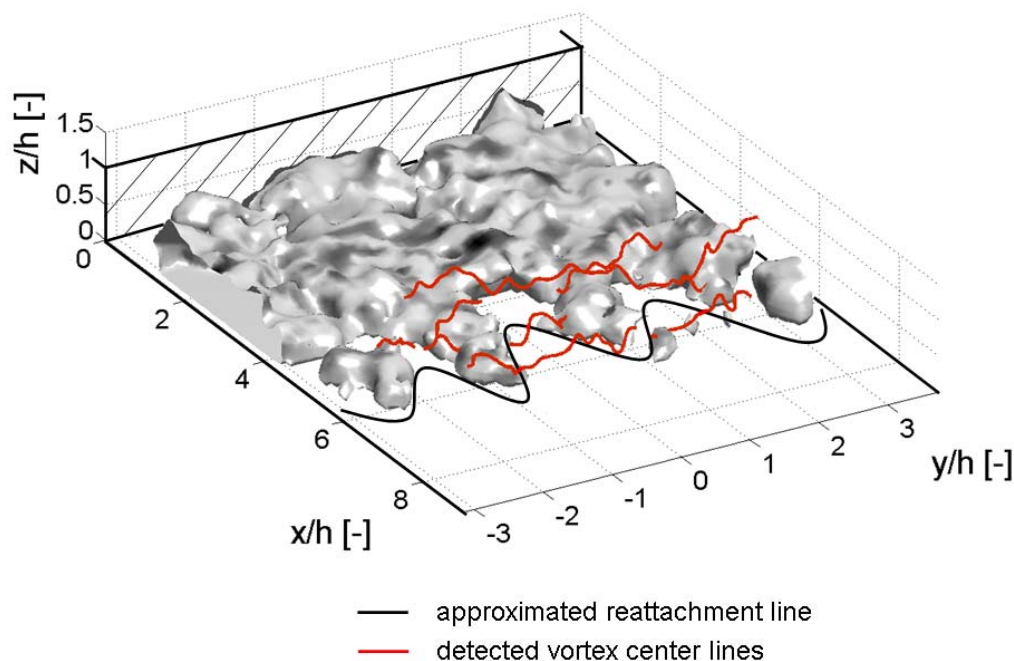
Fig 4.33 Zero-velocity surface showing the heights of the fingers and the connection with rollers

Furthermore, figure 4.33 allows the extraction of another characteristic. Along one single finger at least two in streamwise direction successive rollers are positioned. The reason is in the spatial dimensions of the fingers. The length of the fingers ranges up to 3h in streamwise direction. The rollers have an approximately spatial spacing of 1.2h (see figure 4.18). Thus, two roller formations fit along a finger in streamwise direction. The comparison of rollers belonging to a common finger showed that the large scale wave length is valid for a number of successive rollers indicating a global perturbation.

From here, the following hypothesis is drawn trying to explain the reason for the finger shape of the reattachment line. A schematic description is shown in figure 4.34. A characteristic finger is engulfed by a roller travelling above the finger. Thus, due to the vertically aligned vortex loop, the roller has different distances from the bottom wall in spanwise direction. The figure on the bottom shows three exemplary xz-slices through and beside the finger. From here it is clear that the part of the roller having larger distance from the wall (y_0) will generate more backflow than that part having smaller distance from the wall (y_-, y_+). This local imbalance causes the generation of the characteristic finger configuration.
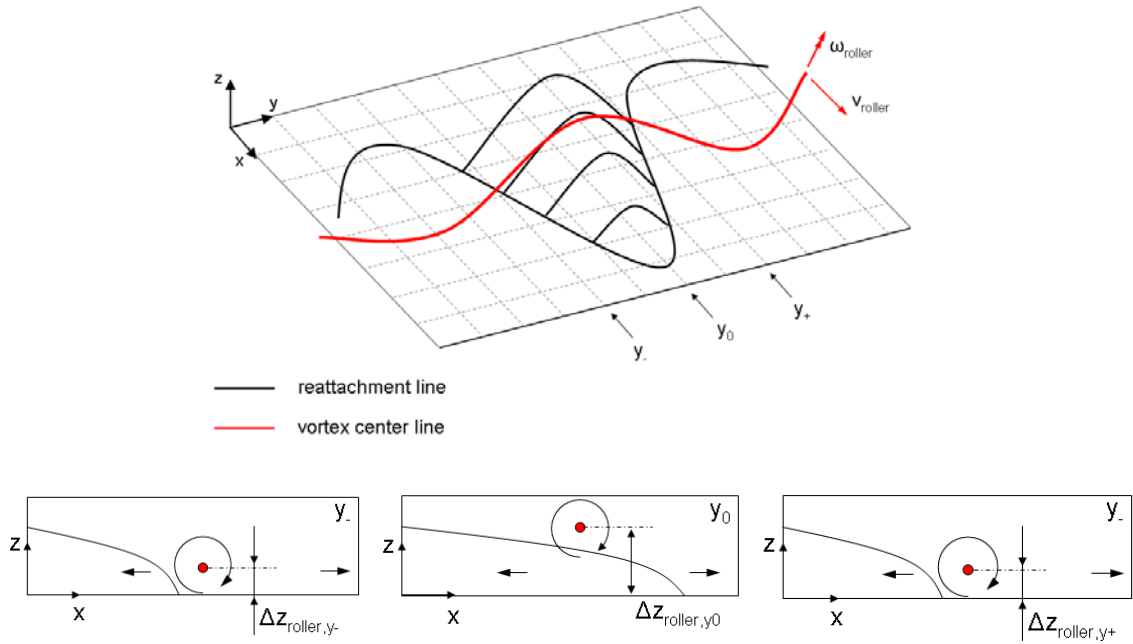
Fig 4.34 Schematic of the generation of fingers; **(top)** isometric view of finger configuration and corresponding roller; (bottom) slices through and beside the finger showing variable distances of roller center from bottom wall

The investigation around reattachment validated the influence of the oncoming rollers on the reattachment position as stated by several authors [54][50][118]. The present test case identified a "finger configuration" around reattachment with $St_{finger}=0.09$. The fingers of recirculating flow are the result of deformed rollers with large length scales. The investigation showed that the fingers are hulled in by the vortex center line. Varying distances of the vortex center lines from the bottom wall result in different amounts of induced backflow. Furthermore, we identify at least two vortices to be part of a finger. Thus, the reason for the halving of the Strouhal number from vortex shedding to reattachment line fluctuation is assumed to be the result of the finger configuration, where two roller lines belong to the formation of one finger. Furthermore, we observe small zones of recirculation downstream of reattachment. These zones are found to be the result of finger merging as shown in figure 4.32.

4.4 Region IV: Recirculation Region

The recirculation region is located upstream of reattachment and below the shear layer. The outer boundary of the region is defined by the zero-velocity iso-surface as shown in figure 4.33. The inner of the recirculation region cannot be classified as a "dead water" region as stated by several authors, e.g. Simpson (1989) [131]. Largest backflow velocities are measured in the range 3<x/h<4 to about 20% of the bulk velocity. Nevertheless, the zone of recirculation gained less attention.

An exemplary LIF visualization for one instantaneous snapshot is shown in figure 4.35. A large scale vortical structure is positioned in the inner of the recirculation region at roughly x/h=2.5. The vortical structure induces vertically directed velocities and thus interacts with the shear layer. The perturbation results in a triggering of the shear layer in the range of the vortical structure. The time resolved LIF visualization as well as previous investigations show a strong interaction between the recirculation region and the shear layer, as already discussed in chapter 4.2. Thus, the aim of this chapter is the extraction of dominant structures inside the recirculation region influencing the developing shear layer.
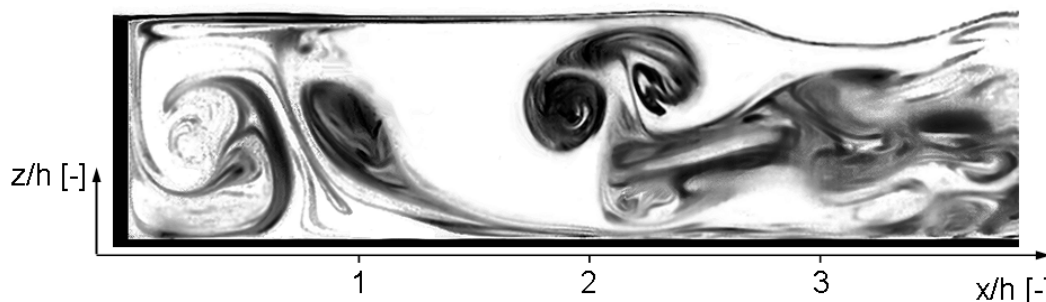
Fig 4.35 LIF visualization showing a mushroom-like vortical structure in the inner of the recirculation region, directed vertically and moving away from the wall, thus disturbing the free shear layer.

Detection of vortical structures

The measurement inside the recirculation region is rather difficult. The flow is highly three-dimensional and unsteady with a large amount of spatial and temporal length scales. Nevertheless, previous investigations observed vortical structures inside the recirculation region. Hairpin-like vortex structures with length scales from 2.5h to 4h in streamwise direction are observed in a conditional averaging of pressure-velocity joint measurements by Lee et al. (2004) [55]. Schröder et al. (2011) visualized hairpins like vortices in a manipulated BFSF via Tomo PIV [127]. The roller formation is triggered via external acoustic excitation. While the rollers impinge on the wall, hairpin like vortices are generated in both flow directions. Characteristic of hairpin like vortical structures is the

lift-up effect and the corresponding large wall normal velocities at the front of the head and between the legs, thus defining a possible detection criterion. Furthermore, the structures are usually found in vicinity of reattachment, thus the region of interest is located, too. Figure 4.36 shows the zero velocity iso surface and the +0.12w iso surface of an instantaneous velocity field in the region of interest at t*=27 (figure 4.31). Four coherent areas of upward directed velocities (blobs) are positioned about reattachment in a certain arrangement. First of all, all blobs are ranging out of the recirculation region, thus interacting with the shear layer and the oncoming rollers. Blob a) and b) are positioned upstream of reattachment and c) and d) are positioned downstream of reattachment. Furthermore, the blobs are aligned in streamwise direction showing a linkage between blobs and fingers.
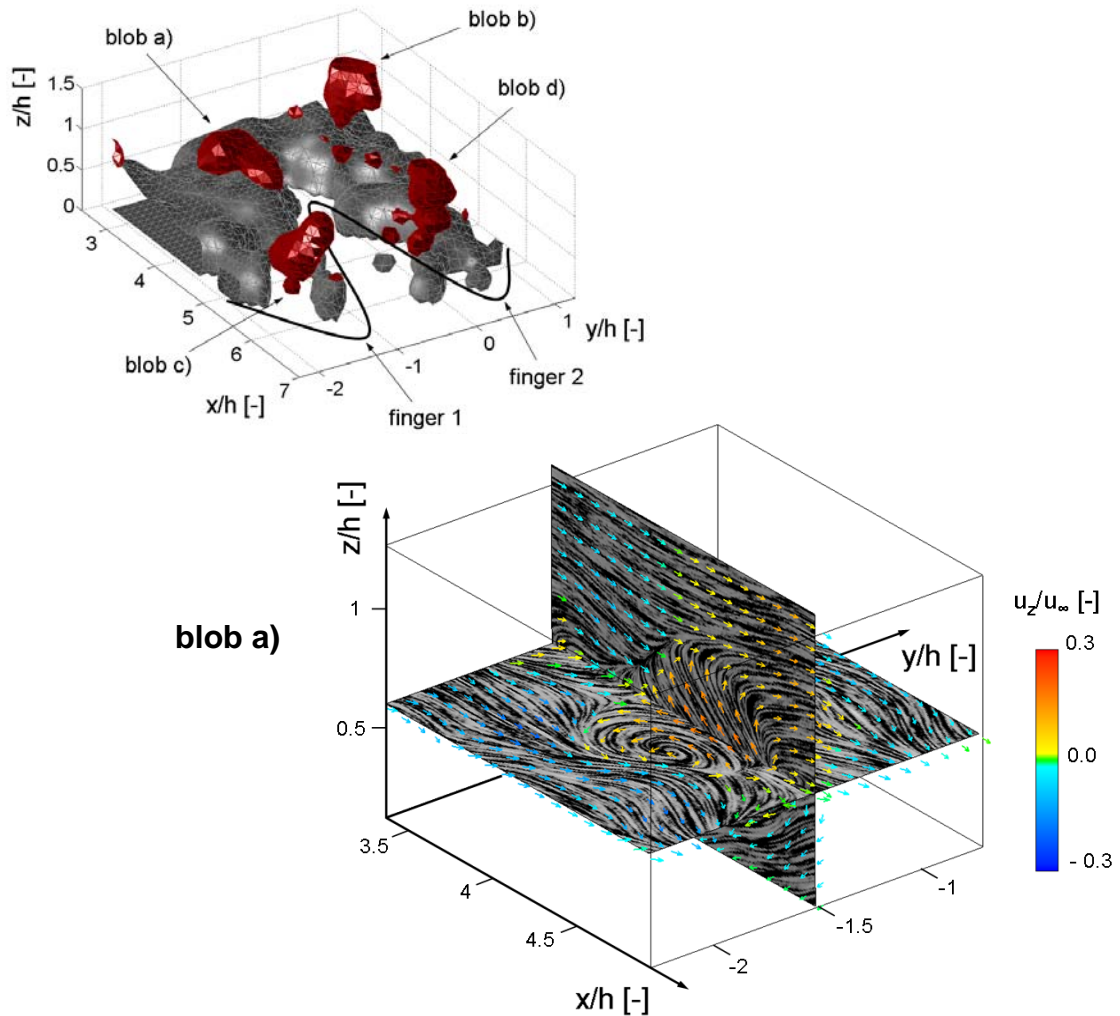
Fig 4.36 Instantaneous visualization of region of interest positioned about reattachment at t*=27 from figure 4.31 **(top)** gray: iso-surface of zero velocity, red: iso-surface of w/U∞=0.12; black line: approximated reattachment line **(bottom)** Blob a) visualized via Line Integral Convolution (LIC) on slices through the hairpin like vortical structure. LIC is superimposed by in plane velocity vectors colour coded by normalized z-velocity

The visualization of the hairpin like structure positioned at (x/h, y/h) = (4, -1.5) is shown in figure 4.36 on the right. The visualization is performed via Line Integral Convolution (LIC) on slices through the volume of interest. The integration length for LIC is chosen by qualitative inspection to t*=0.75. The LIC visualization is superimposed by in plane velocity vectors colour coded by normalized z-velocity. The stagnation point as well as the influence of the surrounding fluid on the hairpin like structure is visible. The downstream convecting fluid above the recirculation region collides with the upward directed velocities of the hairpin like structure. The structure has an approximately inclination angle of 45° at t*=27. Following its evolution in time, we can see from the measurements a change of inclination from initially 30° to finally 90° and a following sweeping away with downstream convecting outer fluid. The lifetime is approximated by the study of single events to t*≈10 depending on the strength of the structure. A breakup is defined here as the loss of upward induced velocity. Further investigations are necessary to study the lifecycle and breakup of these structures in a statistically meaningful manner.

Mechanism of hairpin vortex generation

A basic feature of the travelling rollers is the generation of backflow while travelling with the shear layer in downstream direction. The amount of backflow is dependent on the strength of the roller, the convection velocity of the rollers and on the distance between roller and wall. From the present measurements, it is known that the structure of the rollers in the region of reattachment is described by a wavy line with main orientation in spanwise direction (perturbation). The wavy vortex center line is defined by differing distances from the wall in spanwise direction. Thus, differing velocity profiles are generated along the span forming the characteristic backflow fingers. Due to the generated backflow in the fingers, a hairpin like vortex is generated pointing with its head against the mean flow direction, see figure 4.36.

A proposal for the generation of a hairpin like structure in case of the BFSF is shown in figure 4.37. The roller passes the bottom wall with the convection velocity u_{roller} at t_0. Negative velocities are induced between the roller and the bottom wall due to the circulation around the vortex center line. As the rollers are spatially finite and pass by successively, the temporal behaviour of the backflow is interpreted as sudden bursts with locally higher negative velocity than the surrounding fluid (t_1). Here, similarities can be seen in a jet flow. The injection of fluid with large velocities into a low speed region results in a stagnation point at the front of the jet and in high shear gradients at its border.

In case of the BFSF, the lower boundary of the jet is defined by the wall. In vicinity of the stagnation point the fluid feels a negative change of velocity in streamwise direction. This results in positive change of velocity in y- and z-direction with respect to continuity. Thus, fluid is deflected in positive and negative y-direction, as well as into positive z-direction. The redirection of fluid as well as the shear gradients at the jet boundary generates pairs of vortical structures in the x-y planes generating the legs of the hairpin vortex. The developed hairpin like vortical structure is shown at t_2. The legs of the hairpin vortex are inclined against the bottom wall. Due to the orientation of the vortex loop, down-wash velocities are induced between the legs of the structure, while up-wash velocities occur in front of the head. A comparison can be drawn to hairpin vortices in a turbulent boundary. Here, the inclination angle is typically about 45° and followed by natural break up. In case of the BFSF, the lifetime seems to be shorter due to rapid vortex interaction and thus heavy manipulation of the hairpin like structure. Beside the large scale hairpin like vortical structure, several small scale structures are observed, ranging from arbitrary oriented shear vortices to secondary counter rotating vortical structures as observed in e.g. vortex ring impingement. Chapter 4.6 will focus on the influence of the observed hairpin structure onto the oncoming rollers and the resulting shape of reattachment.
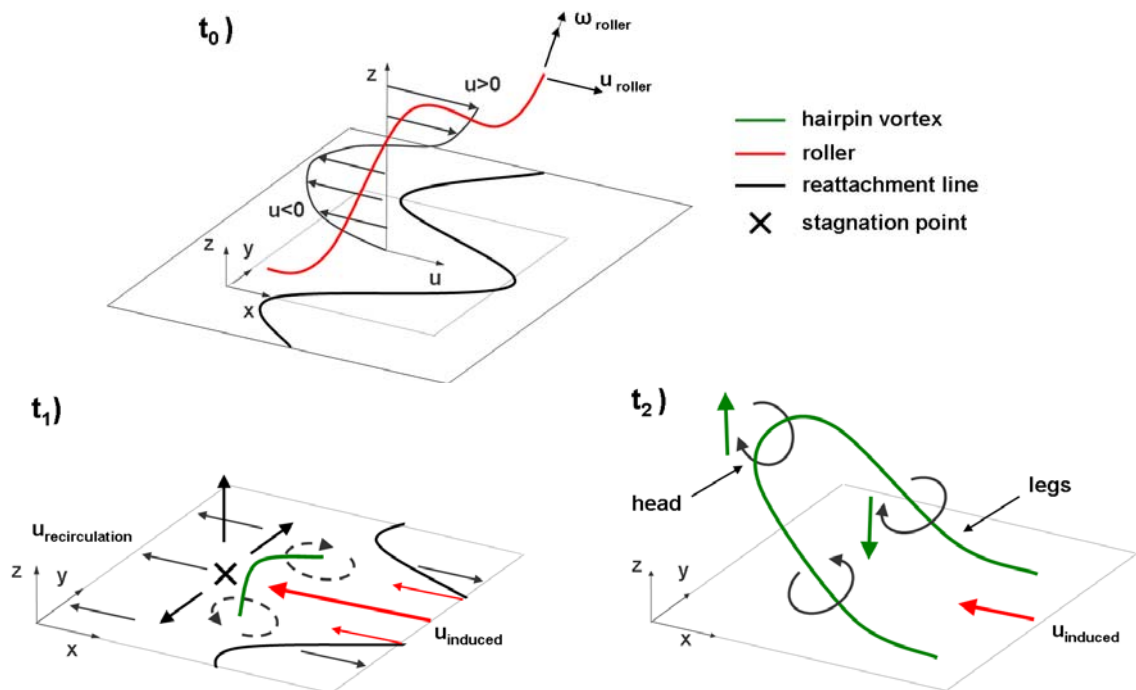
Fig 4.37 Schematic proposal for generation of hairpin vortices in case of the BFSF (mechanism: jet in a cross flow): t_0: roller-wall interaction and corresponding velocity profile (gray), dash dotted black line: reattachment line, t_1: gray: corresponding velocity field in xy-plane, black: dominant velocity directions, x: stagnation point, dashed black line: developing hairpin vortex; t_2: black line: vortex center line of hairpin like vortex structure, black: induced velocity

4.5 Region V and VI: Step Corner and Recovery Zone

The analysis of region V and VI is beyond the scope of the present research as of lower importance for the dominant characteristics at reattachment. A brief overview will be given for completeness highlighting characteristic events in the single regions.

Region VI is positioned downstream of reattachment and is called recovery region. This is for the redevelopment of the separated boundary layer into a turbulent boundary layer. The redevelopment of the boundary layer is visible in figure 4.6 on the left by the median shear sheet in this area. Coherent areas of recirculating flow are observed travelling with the impinged rollers in downstream direction. Furthermore, hairpin like structures are observed downstream of reattachment (see figure 4.36).

Region V is positioned in the vicinity of the step corner and is characterized by a low speed, but fluctuating state. Side wall jets are observed in literature and herein, too. Although, the present test case has a large AR, the influence of the side wall jets is not negligible as shown in figure 3.7. Characteristic of region V is the differing boundary condition in comparison with the other regions. Upstream and bottom boundaries are solid walls. The spanwise boundary of the measurement volume in region V is defined by the side wall jets, the upper boundary by the separated shear layer and the downstream boundary by backflow. Thus, multiple stagnation points are observed. Figure 4.38 shows a schematic scenario in the vicinity of the step corner. Due to the sidewall jets a stagnation point is formed upstream of x/h=1, which induces velocities in streamwise and vertical direction. The collision of the streamwise induced velocity with the backflow generates a second stagnation point downstream of x/h=1 again inducing upward directed velocities.
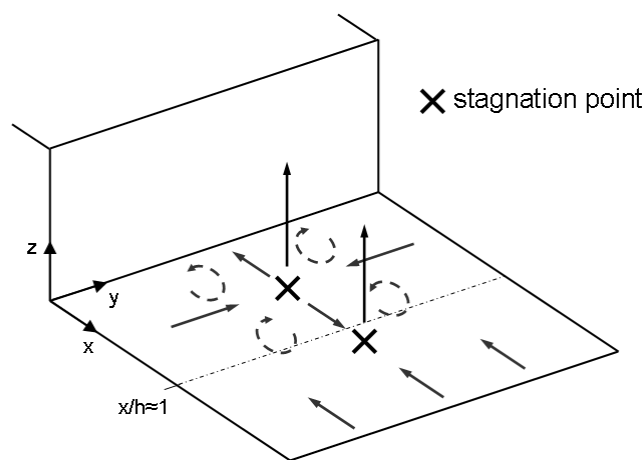
Fig 4.38 Schematic flow situation in vicinity of the step corner; gray: in plane velocity vectors immediately upon the wall; black: resulting upward directed velocity due to stagnation points

The influence of the side wall jets on the developing shear layer is not clarified by the present investigation. The influence of the upward directed velocities and generated vortices due to the stagnation points need more investigation. Similar influences as in case of the generated bursts are expected.

4.6 Roller - Hairpin Vortex Interaction

The influence of the hairpin like structure on the oncoming rollers is shown in figure 4.39 schematically. At approximately x/h =1 the separated boundary layer rolls up with a spanwise wave perturbation of the axis of rotation in wall-normal direction. Let's assume that at the same time a hairpin like structure is generated at a distinct distance downstream of the roller. The structure should be regarded to be spatially stable for a certain time span of Δt^*=10-20 (gray). While travelling in the direction of the hairpin like structure, the roller starts to deform in the xy-plane. The hairpin like structure acts like a local bump.

Locally, the roller tumbles over the bump. In between 3<x/h<4, the vortex loops are therefore locally in the outer region of the shear layer at larger streamwise velocities. Compared to the neighbouring downside directed loops, the locally upside directed rollers reattach later on the bottom wall, generating the finger shape reattachment. Thus, vortex stretching and tilting due to the hairpin structure is the cause of the characteristic 'finger shape' near the wall between 5<x/h<6. It should be noted that the orientation of the vortex loop axes is always a mixture of horizontal and vertical components. Nevertheless, the events are dominated in the pre-described states.
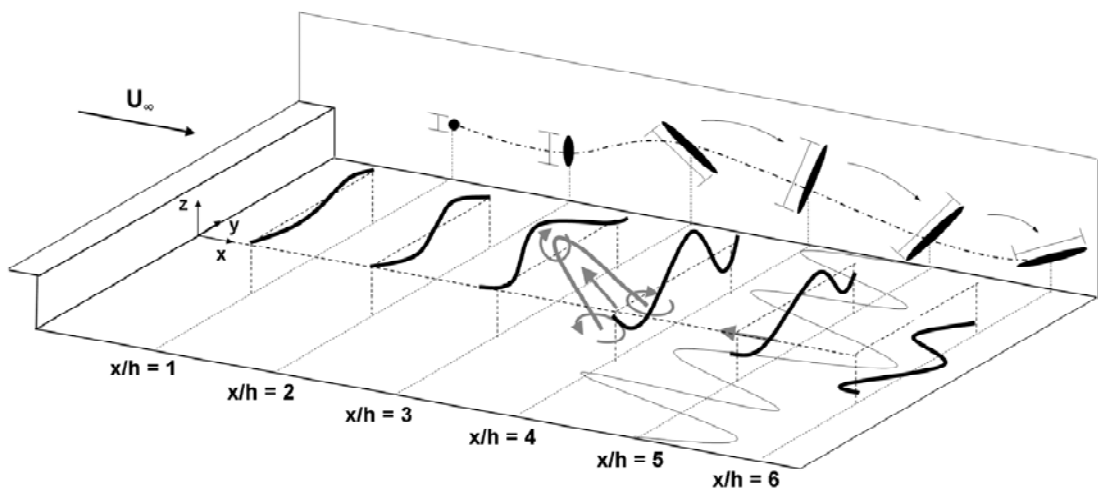
Fig 4.39 Schematic of roller-hairpin interaction; black: roller convecting in downstream direction ($t_0 - t_4$); gray: hairpin like vortical structure (frozen for the observed time sequence)

Figure 4.40 shows an exemplary interaction of a hairpin like structure on an oncoming roller and the resulting reattachment line. The event is described in between t*=22 and t*=30 from figure 4.31 on the right. One identical roller visualized via the vortex center line is tracked for the sequence while influenced by the structure (t_0*≈22, t_1*≈24 t_2*≈26, t_3*≈28, t_4*≈30). The hairpin like structure is visualized via the isosurface of $0.12w/U_\infty$ at t*≈27. Furthermore, a slice at z/h=0.1 is colour coded with backward (blue) and forward (white) flow direction identifying the reattachment position at t_4. It should be mentioned that three-dimensional visualization is rather difficult on a two-dimensional image. In an interactive session, the process described in figure 4.39 is clearly visible in figure 4.40. Nevertheless, the chosen perspective shows the deformation of the roller in vertical direction from t_1 to t_3 while passing over the upward directed velocity. From t_3 to t_4 the vertical aligned vortex loop is reoriented to an inclination angle of roughly 30° with respect to the bottom wall. In between t_2 and t_4 the distance between vortex and bottom wall is rather large and consequently results in a locally large amount of backflow generating the backflow finger.
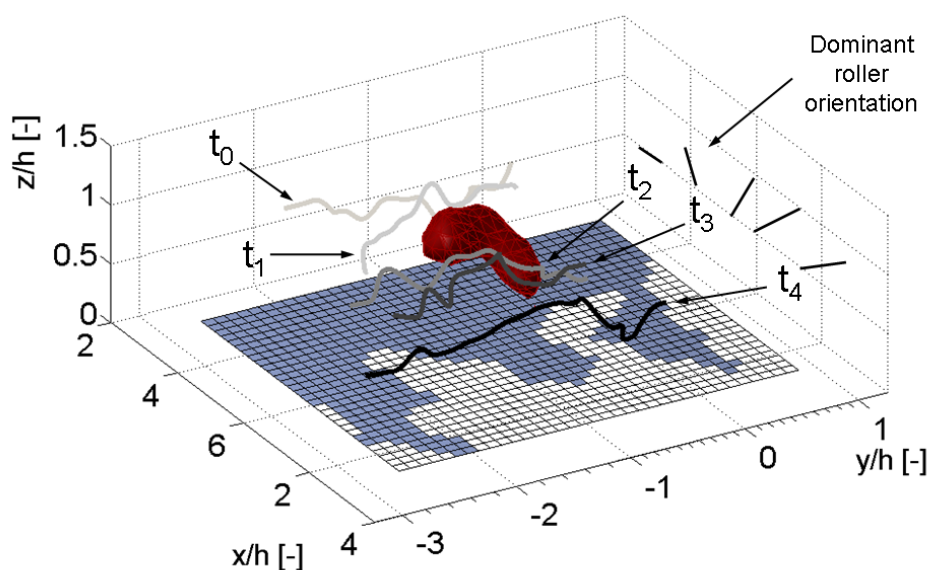
Fig 4.40 Instantaneous visualization of region of interest positioned about reattachment: rollers are visualized via vortex center line (t_0≈22, t_1≈24 t_2≈26, t_3≈28, t_4≈30); red: iso-surface of w/U_∞=0.12; slice at z/h=0.1 shows reattachment line (blue: backward flow, white: forward flow)

This chapter focussed on the influence of large scale vortical structures in the inner of the recirculation region (hairpin vortices) on the oncoming rollers. The investigation showed mechanism, where rollers induce a large amount of backflow inside the backflow fingers. These backflow jets result in stagnation points in the inner of the recirculation region. Due

to the stagnation point, a hairpin like vortical structure is generated, which induces wall-normal velocities ranging out of the recirculation region (bursts). The interaction of these bursts with the oncoming roller results in a deformation of the roller. Due to the larger distance of the deformed vortex loop, a larger amount of backflow at a somehow later instant in time is generated. Furthermore, the deformed roller is made responsible for the shape of reattachment.

5 Conclusion and Outlook

The thesis studies the dynamical and volumetric behaviour of the Backward Facing Step Flow. The first part of the thesis (chapter 2) focuses on the selection and implementation of a sufficient measurement technique for the identification and characterization of volumetric coherent flow structures in case of the present BFSF configuration. A detailed literature review regarding volumetric measurement techniques is given. The development and implementation of the measurement technique of choice "3D Scanning PTV" and its optimizations for measuring the present BFSF configuration are highlighted. This chapter summarizes the results of development and shows limits of the implemented technique. An outlook of further optimizations and future trends regarding volumetric velocimetry measurement techniques is given. The second part of this thesis (chapter 3 and 4) studies the BFSF in a volumetric as well as in a temporal manner. The volumetric measurements give deeper insight into three-dimensional shape of coherent structures of the BFSF, i.e. shear layer, roller, hairpin like structure and recirculation region. Complex interactions of the single coherent structures are highlighted. This chapter summarizes main results, develops a feedback mechanism and gives an outlook of future work as the new knowledge results in new questions.

5.1 Conclusion

Measurement Technique

The experimental study of the BFSF in the turbulent regime is performed via 2D2C time resolved Particle Image Velocimetry, 2D time resolved Laser Induced Fluorescence and 3D Scanning Particle Tracking Velocimetry.

The planar PIV technique is primary applied to study the categorization of the test case in terms of literature and to calculate accurate inlet flow conditions. It should be noted that the implementation and the processing of the two-dimensional raw data into velocity fields is automated in an efficiently manner with high quality by commercial software. The analysis of time resolved data used for the investigation of unsteady phenomena is still not without complications. Data processing, data storage as well as data visualization is critical due to the large amount of data. One time resolved series of the PIV arrangement results in 8 GB raw data producing 2 GB velocity field information. The storage as well as an

automated quality check is a challenging step. Commercial software still fails under these strict conditions.

The planar LIF measurements give great inside into the appearance and dynamical behaviour of coherent structures in the BFSF. Furthermore, the visualization acts as initial guess for the description and detection of flow structures in the three-dimensional data set. In some cases, the flow visualization already gives much information for the physical understanding of the complex processes.

In the present test case, 3D Scanning PTV is selected to be the volumetric measurement technique of choice. The selection is done with respect to a detailed literature review, experimental testing, available hardware and tested flow configuration:

In course of the thesis, pointwise as well as volumetric particle reconstruction is implemented and tested for the analysis in a Lagrangian sense, termed classical PTV and tomographic PTV. For that purpose, a simplified volumetric reconstruction technique is developed using the advantages of telecentric imaging. At least a doubling of the spatial resolution is achievable in tomo PTV compared to classical PTV. Nevertheless, drawbacks are the need for the detection of ghost particles and the large processing overhead. Here, processing on a GPU is not implemented up to now. Thus, the applied reconstruction technique is pointwise reconstruction with respect to the analysis of in total 80GB raw image data.

Lagrangian particle tracking is selected for the calculation of the velocity field. This is for several reasons. A high particle density (as necessary in Eulerian approaches) is critical in the present experimental set-up. Thus, a technique capable of lower particle densities is favoured. Furthermore, a highly fluctuating flow state is apparent in the inner of the recirculation region making a mean translational velocity estimation using correlation based techniques in distinct interrogation areas rather difficult.

The scanning illumination is used for increasing the quality of the particle images as well as for the simplification in the three-dimensional reconstruction. Thus, the scanning illumination increases the number particle density about the factor of applied light sheets. This is for two reasons: The number of projected particle images is reduced due to the slicing of the volume and the search area along the epipolar line is reduced with respect to the thickness of the light sheet.

Advantages of telecentric imaging in terms of image quality and simplification of the pointwise reconstruction are highlighted. Telecentric imaging is characterized by a large depth of field, a constant magnification, high accuracy and negligible distortions. In total,

fifteen steps in calculation of the stereo triangulation are saved due to telecentric imaging, speeding up the pointwise reconstruction.

An estimation of accuracy of the pointwise reconstruction is performed two-fold: On the one hand, calculated three-dimensional marker positions in physical space are compared with the known values, resulting in a mean deviation of 0.014 mm ($\approx$ 0.15 pix). On the other hand, deviation in the three-dimensional positions due to erroneously calculated 2D positions of particles are considered. Here, a theoretical position uncertainty of roughly 0.007 mm is calculated.

The implemented tracking algorithm is a hybrid PIV/PTV 4-frame method. *Hybrid PIV/PTV* means that the first guess in which direction a particle has moved is estimated via cross correlation in an interrogation area. *4-frame* means that if a particle has been tracked for several time steps, the next position is estimated via the kinematic history of the particle. The method is applied on the two-dimensional image plane. Homologous particles for three-dimensional point reconstruction are searched via epipolar line intersection and quality check in object space. For that purpose, the 3D reconstruction is performed trajectory wise in a spatio-temporal manner.

In total, a number of 13 experimental realizations of the BFSF have been recorded with 3D Scanning PTV. Each of the Lagrangian velocity fields contains the same measurement volume (90x60x15 mm³) and a measurement period of 2s in physical time at a recording rate of 1000 fps.

A mean number vector density is calculated to about 42 vectors/cm³. Nevertheless, it should be noted that there is a distinct decrease in number vector density from LS1 to LS4. This is due to difficulties in seeding close to the channel wall. A larger amount of injected particles is transported in downstream direction than is caught by the recirculation region. The difficulty in tracking is about e=1.25 (see figure 2.15). The yield (number of 2D centroid positions/number of three-dimensional vectors) is estimated via the median number of linked particles with respect to the center camera to 58%. Each Lagrangian velocity field is interpolated onto an Eulerian velocity field (grid spacing: 1mm) via inverse distance interpolation. Here, difficulties in non constant seeding are observed. The local number particle density defines the size of the local spatial structure to be measured.

Backward Facing Step Flow

The measurements of the BFSF include three major parts, the inlet flow conditions (chapter 3), the categorization of the present configuration with respect to the large amount of available data in literature (chapter 3) and the volumetric investigation of coherent flow structures (chapter 4). The investigation of volumetric and unsteady properties of the BFSF is focussing on characteristic regions, namely the region of shear layer formation (region I), the region of shear layer development (region II), the region of shear layer impinging (region III) and the region of recirculation (region IV). The analysis of the single regions showed a distinct crosstalk, where the single regions are interacting with each other. The identification of coherent structures focussed on shear layer extraction in region I and large scale vortex detection in region I, II, III and IV. The influence of the region in vicinity of the step corner and of the region of recovery (region V and VI) are assumed to be negligible for shear layer reattachment.

Inlet Flow Conditions

The inlet flow conditions are calculated via planar PIV measurements upstream of the expansion. The installed backward facing step of height h=10mm is characterized by a wedge 6h long and a following plateau of 6h resulting in a contraction from 5h in height to 4h in height. Thus, the expansion ration is ER=1.25. The wedge triggers the boundary layer thickness resulting in a thickening of the boundary layer. The velocity profile is validated to be fully developed again at x/h=-2. The wall shear velocity is calculated via the conventional Clauser chart method to $u_\tau = (\tau_W/\rho)^{1/2} = 25mm/s = 0.05 \cdot U_{bulk}$. The sublayer scaled velocity profile indicates a turbulent flow state prior of separation. The Re-number defined with the step height is $Re_h = 4440$, the momentum thickness prior to separation is $\theta^* = 0.114$ and the turbulence intensity is $Tu_x = 8\%$.

Categorization

The categorization of the BFSF is primarily performed with respect to the integral length scale reattachment length. The reattachment length is influenced by the aspect ratio, the expansion ratio, the boundary layer thickness prior to separation, the turbulence intensity and the Reynolds number. The reattachment length is calculated to about 5.65 h +/- 1.5h in the center of the flow channel. The large aspect ratio of AR = 57 minimizes influences from the side wall on the velocity field about the symmetry plane. Nevertheless, side wall jets are observed in vicinity of the step corner. The low expansion ratio minimizes

influences from the top wall on the region of interest. Secondary recirculation areas above the region of interest are not observed in the planar PIV measurement. The Reynolds number indicates a transitional to turbulent state of the separated boundary layer. The parameter space of Re_h and θ^* positioned the present BFSF configuration into the region of laminar to turbulent separation and turbulent reattachment.

Shear layer characteristics

The shear layer is extracted as the surface of maximum shear, identified via a simplified analysis of the wall-normal velocity gradient $\partial u/\partial z$. A comparison is drawn with a more complex approach analysing the deviatoric rate of strain tensor. Both approaches deliver similar results, especially in region I. The surface of maximum shear is characterized by a wavy structure with heights and ridges immediately downstream of the step. The shear layer is divided in an upper and lower shear layer thickness, defined as the momentum thickness above and below the maximum shear. As expected, the temporal and spanwise averaged shear layer thickness increases up to the point of reattachment. The progress of shear layer thickness shows similarities with a free mixing layer indicating complex vortex dynamics in the range $2<x/h<4$. Here, a dominant influence of the lower shear layer thickness is observed indicating an influence from the recirculation region. The shear layer shows a wavy structure in streamwise and spanwise direction. The amplitude and wave length as well as the ratio perform a kind of balancing in between $0<x/h<2$, while both increase identically in stream- and spanwise direction beyond a distinct point positioned around $x/h=2$. Immediately downstream of the step the amplitude in spanwise direction is roughly 50% larger than that in streamwise direction. Furthermore, the analysis described the convection of perturbations in downstream direction with a convection velocity of roughly $0.6U_0\pm0.2U_0$. In irregular distances large scale perturbations travel along the shear layer showing the transitional flow state.

Roller characteristics

Originating from the shear layer instability, coherent vortical structures are formed with major axis of rotation in spanwise direction. Several Eulerian vortex detection criteria are tested delivering similar results for the detection of the mentioned structure. The swirling strength criterion is chosen due to the highest signal to noise ratio. The 3D profile of the vortex center line is estimated via pointwise connection of local maxima.

Several roll up configurations of the shear layer are identified, i.e. parallel roll up, inclined roll up, convex/concave roll up and piecewise roll up. The most dominant configuration is parallel roll up, but inclined roll ups are observed with inclination angles up to 30° with respect to the step edge. The Strouhal number for vortex formation is calculated to St_{VS}=0.24. The center line of the roller is identified to be wavy immediately after roller genesis generating three-dimensionality immediately downstream of the step. This is postulated to be the result of the roll up of the wavy shear layer. The roller waviness showed distinct specifications depending on the streamwise distance. Thus, the roller performs a stretching in streamwise direction in between 0<x/h<3. At x/h=3, the roller loops are primarily oriented in streamwise direction. Further downstream, the rollers perform a tumbling motion resulting in a re-orientation of the loops in a vertical alignment and following tilting to a somehow streamwise alignment.

Reattachment characteristics

The reattachment line is defined as the intersection of the zero velocity iso-surface with the bottom wall. The volumetric visualizations clearly identified a cyclic change between two states, a finger and a line configuration in the instantaneous reattachment line and vice versa. The non-dimensional frequency is calculated to $St_{fingers}$=0.09. That Strouhal number describes the instantaneous low frequency flapping described in several publications.

The characteristic sawtooth pattern in the temporal progress of reattachment point is found to be the result of a pointwise analysis of reattachment. The sawtooth pattern appears at changes from line to finger configuration. The consideration of all reattachment positions along the span results in a constant decrease and constant increase of reattachment length from line to finger configuration removing the sawtooth pattern. Nevertheless a successive increase and decrease of reattachment length is still observed.

Recirculation characteristics

The analysis of the recirculation region focussed on the extraction of coherent vortex structures generated inside the recirculation region, which influence the oncoming rollers. For that purpose, iso-surfaces of upward directed velocities in vicinity of the streamwise zero-velocity iso-surface are detected. The extraction of the bursts shows a hairpin vortex like shape. The hairpin vortices are generated at the endings of the backflow fingers in upstream and downstream direction. They are concluded to be the result of locally higher backflow velocities induced by the convecting rollers. The unsteady backflow results in the

generation of stagnation points from where the hairpin vortices are born. The lifetime is approximated by the study of single events to t*≈10 depending on the strength of the structure.

Global unsteadiness: line-to-finger configuration

A global unsteadiness with $St_{fingers}$=0.09 is observed, defined by the cyclic change of finger to line configuration and vice versa. Furthermore, a local unsteadiness of shear layer roll up with St_{VS}=0.24 is observed.

This thesis proposes the following scenario for the cyclic change from line to finger configuration. A schematic proposal is shown in figure 5.1. A roller formation is given, which travels in downstream direction. Roller 1 is undisturbed, thus generating an approximately straight reattachment line (t_1). While roller 1 convects in downstream direction, the reattachment length increases (t_2). As the vortex lines are not characterized by straight lines immediately downstream of roll up as valid in a laminar flow, but by a wavy line similar to that of the investigated shear layer, the rollers have varying distances from the bottom wall in spanwise direction. This is roller 2 in figure 5.1 starting to generate the finger configuration of the reattachment line. The roller travels in downstream direction locally inducing larger backflow, thus generating a hairpin like structure inside the recirculation region (t_3). The coherent hairpin structure acts as a kind of bump on the lower wall and forces the oncoming roller (roller 4) to tumble over the bump (t_4). Due to the vortex stretching and tilting in the range of the backflow finger, the characteristic 'finger shape' of reattachment is supported (t_5). Furthermore, the hairpin vortex is dissipated as a result of pairwise vortex interaction. The disturbed roller travels further downstream, while the next oncoming roller (roller 5) is undisturbed and thus generates an approximately line configuration of reattachment (t_5). This process is repeated quasi-periodic with $St_{fingers}$=0.09.

The approximately halving of the frequency from vortex shedding to reattachment line fluctuation is postulated to be the result of the spatial structure of the fingers. The volumetric visualization of rollers and zero velocity iso-surface shows at least two rollers positioned above the backflow fingers. This becomes clear by knowledge that the backflow fingers have an approximated length of 2h to 3h. The streamwise spacing between the rollers is in the range 1h. Thus, the fingers are built by at least two roller formations resulting of at least a halving of the St-number.
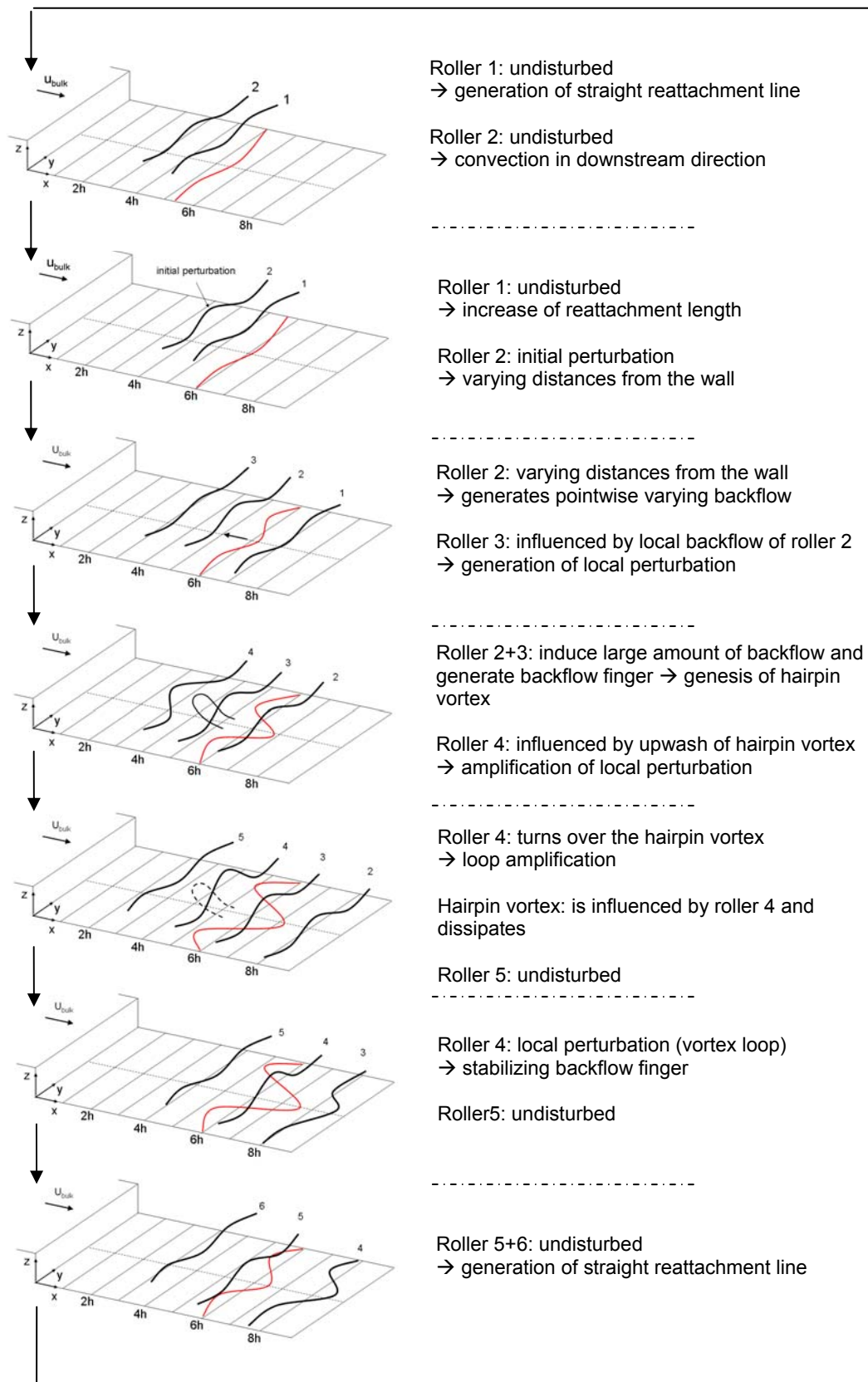
Fig 5.1 Principal sketch of line to finger configuration of reattachment and corresponding rollers; red line: reattachment line; black lines: roller center line, hairpin vortex

The volumetric analysis showed a clear feedback mechanism generating the dynamics of the BFSF. The measurements showed that the consideration of three-dimensionality is mandatory in understanding unsteady flow separation and flow reattachment in detail.

5.2 Outlook

First of all, it should be mentioned that the presentation of a three-dimensional scenario varying in time on a two-dimensional paper is difficult and by no means trivial. Especially the three-dimensional representation of structures varies largely in time and space and makes the visualization from a given perspective subjective. Therefore, some information is only obtainable in an interactive session allowing the change of perspective and zoom in a time varying manner and is presented herein in form of simplified sketches.

Next striking point is the long processing time for the calculation of three-dimensional velocity fields out of image data. Here, GPU implementation is probably the key issue. If the processing for the volumetric reconstruction is getting faster, new approaches (using advantages of volumetric reconstruction) are applicable. A hybrid tomo and classical PTV is conceivable, which combines the advantage of quick processing in classical PTV and higher achievable number particle density in tomo PTV.

The applied volumetric measurement technique is a multi camera approach, where high accuracy calibration is mandatory. Here, single camera approaches outperform the multi camera approaches for a lower number particle density. For that purpose, new trends are recognized in µ-lens systems. Here, a virtual multi camera system is generated by a proper lens combination in front of a single recording sensor. The advantage of a single camera system and the advantage of a multi camera system are combined. Prerequisite is a high spatial resolution of the sensor chip.

The generated volumetric velocity field showed several new aspects regarding a fluid-mechanical interpretation. Nevertheless, this thesis analyzed a small amount of extractable data. The focus is on coherent structures in proximity of the shear layer. The region in the vicinity of the step corner needs more attention as well as the recovery region and vortex pairing events. Further investigations in other directions (statistical analysis, stability analysis or event tracking) are necessary to understand the simplification of the BFSF in terms of flow separation and reattachment.

As there is no possibility for a single person or a single working group to investigate all facets of the flow configuration, the volumetric dataset of an exemplary measurement in

the Lagrangian and Eulerian frame can be downloaded on the homepage of the Institute for Mechanics and Fluid-Dynamics of the University of Freiberg.

The major outcome of the thesis (with respect to fluid mechanics) is the cyclic interchange of the shape of reattachment between line and finger configuration. The volumetric measurements allowed the identification of mechanisms forcing the different configurations. Recent investigations at the Institute for Mechanics and Fluid-Dynamics test the influence of flexible flaps on the suction side of an airfoil. The flaps are positioned in spanwise lines on the suction side of the airfoil at differing downstream positions. Flow separation is forced by pitching and thus a recirculation region is induced. The results show that the motion of flaps varies in a wavy manner in spanwise direction and consequently indicates that the reattachment location varies in spanwise direction, too. Further investigations are planned to measure the flow details on the airfoil with the same method of 3D Scanning PTV developed in this thesis for finding links between the results presented herein and the reattachment characteristics of an airfoil.

Bibliography

[1]   Adams E.W., Johnston J.P. (1988) Effects of separating shear layer on the reattachment flow structure Part 2: Reattachment length and wall shear stress. Experiments in Fluids 6, 493-499

[2]   Adrian R., Meinhart C., Tomkins C. (2002) Vortex organization in the outer region of the turbulent boundary layer, J. Fluid Mech. 422, pp. 1-54

[3]   Agüi J.C., Jimenez J. (1987) On the performance of particle tracking. J.Fluid Mech. 185: 447-468

[4]   Armaly B.F., Durst F., Pereira J.C.F., Schönung B. (1983), Experimental and theoretical investigation of backward facing step flow, Journal of Fluid Mechanics vol. 127 pp. 473-496

[5]   Arroyo M.P., Hinsch K.D. (2008) Recent Developments of PIV towards 3D Measurements. Topics in Applied Physics 112, pp. 127-154

[6]   Atkinson and Soria (2009) An efficient simultaneous reconstruction technique for tomographic particle image velocimetry, Experiments in fluids

[7]   Atkinson C.H. and Soria J. (2007) Algebraic Reconstruction Techniques for Tomographic Particle Image Velocimetry, 16th Australasian Fluid Mechanics Conference

[8]   Awatsuji Y., Fujii A., Kubota T., Matoba O. (2006) Parallel three-step phase-shifting digital holography , Appl. Opt. 45, 2995-3002

[9]   Baek S.J., Lee S.J. (1996) A new two-frame particle tracking algorithm using match probability. Exp. Fluids 23: 261-304

[10]   Barnhardt D.H., Hampp N., Halliwell N.A., Coupland J.M. (2002) Digital holographic velocimetry with bacteriorhodopsin (BR) for real-time recording and numeric reconstruction. 11th Int. Symp. On Applcation of Laser Techniques to Fluid Mechanics

[11]   Beaudoin J.-F., Cadot O., Aider J.-L., Wesfreid J.E. (2004) Three-dimensional flow over a backward-facing step. European Journal of Mechanics B/Fluids 23, 147-155 pp

[12]   Biswas G., Breuer M., Durst F. (2004) Backward-Facing Step Flows for Various Expansion Ratios at Low and Moderate Reynolds Numbers. Transactions of the ASME 126: 362-374

[13]   Biswas G., Breuer M., Durst F. (2004) Backward-Facing Step Flows for Various Expansion Ratios at Low and Moderate Reynolds Numbers. J. Fluids Eng. 126, pp. 362-374

[14]   Biwole P.H., Yan W., Zhang Y., Roux1 J.-J. (2009) A complete 3D particle tracking algorithm and its applications to the indoor airflow study, Meas. Sci. Technol. 20 115403 (13pp)

[15]   Bouhoubeiny E., Druault P. (2009) Note on the POD-based time interpolation from successive PIV images. C.R. Mecanique 337: 776-780

[16]   Brederode V. de, Bradshaw P. (1972) Three dimensional flow in normally two dimensional separation bubbles. I.C. Aero rep. pp 72-91, Imperial College, London

[17]   Brücker Ch. (1996) 3-D scanning-particle-image-velocimetry: Technique and application to a spherical cap wake flow. Appl. Sci. Res. 56, 157-179

[18]   Brücker Ch. (1999) The 3-D Evolution of the starting vortex downstream of a Backward-Facing Step Studied by Sequential High-Speed Scanning PIV. Proc. 8th Int. Conf. on Laser Anemometry, Rome

[19]   Buraga-Lefevre C., Coetemllec S., Lebrun D., Özkul C. (2000) Application of wavelet transform to hologram analysis: Three-dimensional location of particles. Opt. Lasers Eng. 33: 409-421

[20]   Chakraborty O., Balchandar S., Adrian R.J. (2005) On the relationships between local vortex identification schemes. J. Fluid Mech. 535: 189-214

[21]   Champagnat F., Plyer A., G. Le Besnerais, B. Leclaire et Y. Le Sant, "How to calculate dense PIV vector fields at video rate," 8th Int. Symp. On Particle Image Velocimetry, PIV09, Melbourne, Victoria (Australia), August 25-28, 2009.

[22]   Chiang T.P. and Sheu T.W.H. (1999) A numerical revisit of backward-facing step flow problem. Phys. Fluids 11, pp. 862-874

[23]   Chong M.S., Perry A.E., Cantwell B.J. (1990) A general classification of three-dimensional flow fields. Phys. Fluids A2: 765-777

[24]   Clauser F. (1956) The turbulent boundary layer. Adv. Appl Mech 4, pp. 1- 51

[25]   Coetemllec S., Lebrun D., Özkul C. (2002) Application of the two-dimensional fractional-order fourier transformation to particle field digital holography. J. Opt. Soc. Am. A 19: 1537-1546

[26]   Cucitore R., Quadrio M., Baron A. (1999) On the effectiveness and limitations of local criteria for the identification of a vortex. Eur. J. Mech. B/Fluids 18: 261-282

[27]   Delcayre M and Lesieur M. (1997) Topological feature in the reattachment region of a backward-facing step. 1st AFOSR Int.Conf. on DNS and LES, Ruston

[28]   Driver D.M., Seegmiller H.L., Marvin J.G. (1987) Time-dependent behaviour of a reattaching shear layer, AIAA J25, pp. 914-919

[29]   Dryden, Hugh L. Recent advances in the mechanics of boundary layer flow. Advances in Applied Mechanics 1, Academic Press, New York, pp.1-40

[30]   Durault Ph., Guibert Ph., Alizon F. (2005) Use of proper orthogonal decomposition for time interpolation from PIV data. Exp.Fluids 39: 1009-1023

[31]   Durst F. and Tropea C. (1981) Turbulent Backward-Facing Step Flows in two-dimensional ducts and channels. 3rd Symposium on turbulent Shear Flows, Davis CA

[32]   Eaton J.K., Johnston J.P. (1980) Low-frequency unsteadiness of a reattaching turbulent shear layer. In: Proc. 3rd Int. Symp. Turbulent Shear Flow

[33]   Elsinga G.E. (2008) Tomographic Particle Image Velocimetry, Ph.D. Thesis, Department of Aerospace Engineering, Delft University of Technology.

[34]   Elsinga G.E., Scarano F., Wieneke B., van Oudheusden B.W. (2006) Tomographic Particle Image Velocimetry. Exp. Fluids 41: 933-947

[35]   Garcia D. (2010) A fast all-in-one method for automated post-processing of PIV data. Exp. Fluids: DOI 10.1007/s00348-010-0985-y

[36]   Gharib M., Pereira F., Dabiri D., Hove J.R., Modarress D. (2002) Quantitative Flow Visualization: Toward a Comprehensive Flow Diagnostic Tool. Integrative and Comparative Biology vol. 42, issue 5 pp. 964-970

[37]   Gunes H., Rist U. (2007) Spatial resolution enhancement/smoothing of stereo-particle-image-velocimetry data using proper-orthogonal-decomposition-based and Kriging interpolation methods. Phys. of Fluids 19

[38]   Gunes H., Sirisup S., Karniadakis G.E. (2006) Gappy data: To Krig or not to Krig. J. Chem. Phys. 212

[39]   Haimes R., Kenwright D. (1999) On the Velocity Gradient Tensor and Fluid Feature Extraction AIAA 14^t Computational Fluid Dynamics Conference: 3288-3297

[40]   Hain R., Kähler C. J. and Radespiel R. (2009) Principles of a Volumetric Velocity Measurement Technique Based on Optical Aberrations. Notes on Numerical Fluid Mechanics and Multidisciplinary Design 106, Springer Verlag, pp 1-10

[41]   Hain R., Kahler C.J. and Tropea C. (2007) Comparison of CCD, CMOS and intensified cameras. Exp. Fluids 42, 403–411

[42]   Hairer E., Norsett S.P., Wanner G. (1993): Solving Ordinary Differential Equations I, Springer

[43]   Haller G. (2002) Lagrangian coherent structures from approximate velocity data. Physics of Fluids 14(6): 1851-1861

[44]   Haller G. (2005) An objective definition of a vortex. J. Fluid Mech. 525: 1-26

[45]   Herman G. T. and Lent A. (1976) Iterative reconstruction algorithms. Computers in Biology & Medicine 6, Pergamon Press, pp. 273-294

[46]   Hesselink L., Post F., van Wijk. J.J. (1994) Research issues in vector and tensor field visualization. IEEE Computer Graphics and Applications, 14(2)

[47]   Ho C.-M. and Huerre P. (1984) Perturbed Free Shear Layers. Ann. Rev. Fluid Mech. 16, pp. 365-424

[48]   Hoyer K, Holzner M., Lüthi B., Guala M., Liberzon A., Kinzelbach W. (2005) 3D scanning particle tracking velocimetry Exp. Fluids 29: 145-53

[49]   Hoyer K., Holzner M., Lüthi B., Guala M., Liberzon A., Kinzelbach W. (2005) 3D scanning particle tracking Velocimetry, Exp. in Fluids 39, pp. 923- 934

[50]   Huang H.T., Fiedler H. (1997) A DPIV study of a starting flow downstream of a backward-facing step. Experiments in Fluids 23, pp. 395-404

[51]   Hudy L.M., Naguib A., Humphreys W.M. (2006) Stochastic estimation of a separated-flow field using wall-pressure-array measurements, Physics of Fluids vol. 19

[52]   Hunt J.C.R., Wray A.A., Moin P. (1988) Eddies, streams, and convergence zones in turbulent flows. Center of Turbulence Research Report CTR-288: 193-208

[53]   I. Lee, H.J. Sung (2002) Multiple-arrayed pressure measurement for investigation of the unsteady flow structure of a reattaching shear layer, J Fluid Mech 463 pp.377-402

[54]   I. Lee, H.J. Sung (2002) Multiple-arrayed pressure measurement for investigation of the unsteady flow structure of a reattaching shear layer, J Fluid Mech 463 pp.377-402

[55]   I. Lee, S. K. Ahn, H. J. Sung (2004), Three-dimensional coherent structure in a separated and reattaching flow over a backward-facing step, Experiments in Fluids vol. 36 pp. 373-383

[56]   Ishikawa M., Murai Y., Wada A., Iguchi M., Okamoto K., Yamamoto F. (2000) A novel algorithm for particle tracking velocimetry using the velocity gradient tensor. Exp. Fluids 29: 519-531

[57]   Jeong J. and Hussain F. (1995) On the identification of a vortex. J. Fluid Mech. 173: 303-356

[58]   Jiang M., Machiraju R., Thompson D. (2005) Detection and Visualization of Vortices. The Visualization Handbook: 295-309

[59]   Jovic S., Driver D. M. (1995) Reynolds number effects on the skin friction in separated flows behind a backward facing step. Exp. Fluids 18, 464-467

[60]   Kähler J.C. (2004) The significance of coherent flow structures for the turbulent mixing in wall-bounded flows. PHD thesis, Georg-August-Universität zu Göttingen

[61]   Kasagi N., Matsunaga A. (1995) Three-dimensional particle-tracking velocimetry measurements of turbulence statistics and energy budget in a backward-facing step flow. Int. J. Heat and Fluid Flow 16, pp. 477-485

[62]   Kenwright D.N, Henze C., Levit C. (1999) Feature extraction of separation and attachment lines. IEEE Transactions on Visualization and Computer Graphics 5/2: pp. 135-144

[63]   Kenwright D.N. (1998). Automatic detection of open and closed separation and attachment lines. In *Proc. Visualization'98*, pages 151–158

[64]   Kitzhofer J., Brücker C. (2010) Tomographic Particle Tracking Velocimetry using telecentric imaging. Exp. Fluids, 2010, DOI 10.1007/s00348-010-0879-z

[65]   Kitzhofer J., Brücker C., Nonn T. (2011) 3D Visualization as a tool for analyzing volumetric velocity fields, submitted to Experiments in Fluids

[66]   Kitzhofer J., Kirmse C., Brücker C. (2009) High density, Long Term Particle Tracking Velocimetry. Notes on Numerical Fluid Mechanics and Multidisciplinary Design, vol. 106, pp. 125-134

[67]   Kitzhofer J., Westfeld P., Pust O., Nonn T., Maas H.G., Brücker C. (2010) Calculation of 3D Deformation and Rotation rate Tensor from volumetric particle data via 3D Least Squares Matching, submitted to special issue of Proceedings of the 15th International Symposium on Applications of Laser Techniques to Fluid Mechanics, 5-8 July 2010, Lisbon

[68]   Kolár V. (2007) Vortex identification: New requirements and limitations. International Journal of Heat and Fluid Flow 28: 638-652

[69]   Kostas J., Soria J., Chong M.S. (2002) Particle image velocimetry measurements of a backward-facing step flow. Exp. Fluids. 33, pp. 838-853

[70]   Laurentini A., (1994) How many 2D silhouettes does it take to reconstruct a 3D object? Computer Vision and Image Understanding, Vol. 67, Nr. 1, pp 81-87

[71]   Le H., Moin P., Kim J. (1997) Direct numerical simulation of turbulent flow over a backward-facing step. Technical Report TF-58, Stanford Univ, Dept of Mech Eng, Thermosciences Div

[72]   Li M., Kudo H., Hu J., Johnson R.H. (2004) Improved iterative algorithm for sparse object reconstruction and its performance evaluation with micro-ct data. IEEE Transactions on Nuclear Science 51 pp. 659-666

[73]   Liang D.F., Jiang C.B., Li Y.L. (2003) Cellular neural network to detect spurious vectors in PIV data. Exp.Fluids 34: 52-62

[74]   Lobutova E., Resagk C., Rank R., Müller D., Putze T., Maas H.-G. (2007) Investigation of large-scale flow structures in Rayleigh-Bernard convection using 3D particle tracking velocimetry. Symposium Lasermethoden in der Strömungsmesstechnik , Rostock

[75]   Lu J., Fugal J. P., Nordsiek H., Saw E. W., Shaw R. A., Yang W. (2008) Lagrangian particle tracking in three dimensions via single-camera in-line digital holography. New Journal of Physics 10: 24pp

[76]   Lu W., Yin F. (2004) Adaptive algebraic reconstruction technique. Med. Phys. 31 pp. 3222-3230

[77]   Lüthi B.,Tsinoba A., Kinzelbach W. (2005) *Lagrangian measurement of vorticity dynamics in turbulent flow.* J. Fluid Mech. 528: 87-118

[78]   Maas H.G. (1992) Digitale Photogrammetrie in der dreidimensionalen Strömungsmesstechnik, *Ph.D. Thesis*, ETH Zürich

[79]   Maas H.G., Stefanidis A., Grün A. (1994) From pixels to voxels – tracking volume elements in sequences of 3-d digital images. International Archives of Photogrammetry and Remote Sensing 30, 3/2

[80]   Maas HG, Westfeld P, Putze T., Botkjaer N, Kitzhofer J, Brücker C (2009) Photogrammetric techniques in multi-camera tomographic PIV. Proceedings of the 8th International Symposium on Particle Image Velocimetry, Melbourne, Australia

[81]   Malik N.A. and Dracos, T. (1995) Interpolation schemes for three-dimensional velocity fields from scattered data using Taylor expansions. J. Comput. Phys. 119: 231–243.

[82]   Malik, N., Dracos, T., Papantoniou, D., (1993) Particle Tracking in three dimensional turbulent flows - Part II: Particle tracking. Experiments in Fluids Vol. 15, pp. 279-294

[83]   Malkiel E., Sheng J., Katz J., Strickler J. R. (2003) The three-dimensional flow field generated by a feeding calanoid copepod measured using digital holography. J. Exp. Bio. 206: 3657-3666

[84]   Meiburg E., Lasheras J.C., Ashurst Wm. T. (1988) Topology of the vorticity field in three-dimensional shear layers and wakes. Fluid Dynamics Research 3, pp.140-148

[85]   Meng H., Hussain F. (1995) In-line recording and off-axis viewing technique for holographic particle velocimetry. Appl. Opt. 34: 1827–40

[86]   Meng H., Pan G., Pu Y., Woodward S.H. (2004) Holographic particle image velocimetry: From film to digital recording. Meas. Sci. Technol. 15:673-685

[87]   Metais (2001)

[88]   Mordant N., Crawford A.M., Bodenschatz E. (2004) Experimental Lagrangian acceleration probability density function measurement. Physica D 193, pp. 245-251

[89]   Morris S.C. (2010) Shear-Layer Instabilities: Particle Image Velocimetry Measurements and Implications for Acoustics. Annu. Rev. Fluid Mech 2011.43

[90]   Muller A., Gyr A. (1982) Visualization of the mixing layer behind dunes. Proc. Euromech 156

[91]   Nie J.H., and Armaly B.F. (2003) Reattachment of Three-Dimensional Flow Adjacent to Backward-Facing Step. Transactions of the ASME 125: 422-428

[92]   Nonn T. (2010) Application of High Performance Computing on Volumetric Velocimetry Processing. 15th Int. Symp. on Applications of Laser Techniques to Fluid Mechanics Lisbon, Portugal

[93]   Okamoto K., Hassan Y.A., Schmidl W.D. (1995) New tracking algorithm for particle image velocimetry. Exp. Fluids 19: 342.347

[94]   ÖtügenM.V. (1991) Expansion ratio Effects on the Separated Shear Layer and Reattachment Downstream of a Backward Facing Step. Exp-Fluids, 10, pp. 273-280

[95]   Ouelette N.T., Xu H., Bodenschatz E., (2006) A quantitative study of three-dimensional Lagrangian particle tracking algorithms, Experiments in Fluids 40, pp 301-313

[96]   Pagendarm H.-G., Walter B. (1994) Feature Detection from Vector Quantities in a Numerically Simulated Hypersonic Flow Field in Combination with Experimental Flow Visualization. IEEE Computer Society Press: 117-123

[97]   Palero V., Arroyo M. P., Soria J. (2001) Digital in-line holographic PIV for 3D particulate flow diagnostics. Proc. 4th Int. symp. On Particle Image Velocimetry, Göttingen

[98]   Pan G., Meng H. (2003) Digital Holography of particle fields: reconstruction by use of complex amplitude. Appl. Opt. 42: 827, pp33

[99]   Pereira F., Gharib M. (2002) Defocusing digital particle image velocimetry and the three-dimensional characterization of two-phase flows. Meas. Sci. Technol. 13:683-694

[100]   Ponitz Benjamin (2010) Experimentelle Untersuchungen der turbulenten Stufenströmung (Backward Facing Step Flow) in einem Wasserkanal mittels dreidimensionaler optischer Strömungsmesstechnik, Diplomarbeit, TU Freiberg, Germany

[101]   Pothos S., Troolin D., Lai W., Menon R. (2009) V3V – Volumetric three-component velocimetry for 3D flow measurements – main principle, theory and applications. Revista Termotehnica 2/2009

[102]   Pronchick S. (1983) Experimental investigation of the turbulent flow behind a backward facing step. PhD dissertation. Stanford University

[103]   Pu Y., Meng H. (2005) Four-dimensional dynamic flow measurement by holographic particle image velocimetry. Appl. Opt. 44:7697-7708

[104]   Pun C.S., Susanto A., Dabiri D. (2007) Mode-ratio bootstrapping method for PIV outlier correction. Meas. Sci. Technol. 18: 3511-3522

[105]   Putze, T. (2008) Geometrische und stochastische Modelle zur Optimierung der Leistungsfähigkeit des 3D PTV, *Ph.D. Thesis,* Fakultät Forst-, Geo- und Hydro-wissenschaften, Dresden University of Technology

[106]   Raffel M., Gharib M., Ronneberger O., Kompenhans J. (1995) Feasibility study of three-dimensional PIV by correlating images of particles within parallel light sheet planes. Exp Fluids 19:69-77

[107]   Raffel M., Westerweel J., Willert C., Gharib M., Kompenhans J. (1996) Analytical and experimental investigations of dual-plane particle image velocimetry. Opt. Eng. 35: 2067-74

[108]   Raffel M., Willert C., Wereley S., Kompenhans J. (2007) Particle image velocimetry. A practical guide, Springer, Berlin

[109]   Rinioe K., Shirai Y., Sunada Y. (2002) Behavior of separated and Reattaching Flow Formed over a Backward Facing Step. Transactions of the Japan Society for aeronautical and space sciences 45 (147)

[110]   Robinson O., Rockwell D. (1993) Construction of three-dimensional images of flow structure via particle tracking techniques. Exp Fluids 14: 257-270

[111]   Roshko A. (1976) Structure of Turbulent shear flows: A new look, AIAA Jpurnal, vol. 14, no. 10, pp. 1349-1357

[112]   Scarano (2001) vortex pattern BFSF

[113]   Scarano F, Poelma C. (2009) Three-dimensional vorticity patterns of cylinder wakes. Exp. Fluids 47, 69-83

[114]   Scarano F, Riethmuller ML (2000) Advances in iterative multigrid PIV image processing. Exp Fluids 29: 51–S60

[115]   Scarano F. (2002) Iterative image deformation methods in PIV. Meas. Sci. Technol 13

[116]   Scarano F., Benocci C. and Riethmüller L. (1999), Pattern recognition analysis of the turbulent flow past a backward facing step, Physics of Fluids vol. 11, number 12

[117]   Scarano F., Moore P. (2010) An advection model to increase the time-resolution of PIV time-series. Proc. Of 15th Int. Symp. on Applications of Laser Technoques to Fluid Mechanics, Lisbon

[118]   Schäfer F, Breuer M. and Durst F. (2009) The dynamics of the transitional flow over a backward-facing Step, Journal of Fluid Mechanics, vol. 623, pp. 85-119

[119]   Schäfer F., Breuer M., Durst F. (2009) The dynamics of the transitional flow over a backward-facing Stepp. J. Fluid Mech. 623, pp. 85-119

[120]   Schafhitzel T., Baysal K., Vaaraniemi M., Rist U., Weiskopf D. (2010) Visualizing the Evolution and Interaction of Vortices and Shear Layers in Time-Dependent 3D Flow. To appear in IEEE Transaction on Visualization and Computer Graphics

[121]   Schiwietz, T., Westermann, R., GPU-PIV, VMV 2004

[122]   Schnars U., Jüptner P.O. (2002) Digital recording and numerical reconstruction of holograms. Meas. Sci. Technol. 13: 85-101

[123]   Schnars U., Juptner W.P. (1994) Direct recording of holograms by a CCD target and numerical reconstruction. Appl. Opt. 33: 179-81

[124]   Schram C., Rambaud P., Riethmüller M.L. (2004) Wavelet based eddy structure eduction from a backward facing step flow investigated using particle image velocimetry

[125]   Schreer O. (2005) Stereoanalyse und Bildsynthese, Springer, Berlin

[126]   Schröder A. Geisler R., Staack K., Elsinga G.E., Scarano F., Wieneke B., Henning A., Poelma C., Westerweel J. (2010) Eulerian and Lagrangian views of a turbulent boundary layer flow using time-resolved tomographic PIV. Exp. Fluids 50: 1071-1091 pp.

[127]   Schröder A., Schanz D., Heine B., Dierksheide U. (2011) Investigation of transitional flow structures downstream of a backward-facing-step flow by using 2D-2C and high resolution 3D-3C-tomo PIV, submitted to 17. DGLR/STAB-Symp.

[128]   Shepard D. (1968). A two-dimensional interpolation function for irregularly-spaced data. Proceedings of the 1968 ACM National Conference. Pp. 517–524.

[129]   Shih, C., Ho C.-M. (1994) Three-dimensional recirculation flow in a backward facing step

[130]   Shivsai Ajit Dixit and O. N. Ramesh (2009) Determination of skin friction in strong pressure-gradient equilibrium and near-equilibrium turbulent boundary layer, Experiments in Fluids

[131]   Simpson R.L. (1989) Turbulent boundary-layer separation. Ann. Rev. Fluid Mech. 21, pp. 205-239

[132]   Soria J., Atkinson C. (2008) Towards 3C-3D digital holographic fluid velocity vector field measurement – tomographic digital holographic PIV. Meas. Sci. Tecnol. 19: 12pp

[133]   Spazzini P.G., Iuso G., Onorato M., Zurlo N., Di Cicca G.M. (2001) Unsteady behaviour of back-facing step flow, Experiments in Fluids vol. 30 pp. 551-561

[134]   Stuer H., Blaser S. (2000) *Interpolation of Scattered 3D PTV Data to a Regular Grid*. Flow, Turbulence and Combustion 64: 215-232

[135]   Telea A., van Wijk J. (2003) 3D IBFV: Hardware-Accelerated 3D Flow Visualization. IEEE Visualization '03

[136]   Trolinger J. D., Belz R. A., Farmer W. M. (1969) Holographic techniques for the study of dynamic particle fields. Appl. Opt. 8, 957-961

[137]   Troutt T.R., Scheelke B., Norman T.R. (1984) Organized structures in a reattaching separated flow field. J. Fluid Mech. 143, pp. 413-427

[138]   Tylli N., Kaiktsis L., Ineichen B. (2002) Sidewall effects in flow over a backward-facing Stepp: Experiments and numerical simulations. Phys. Fluids 14, pp. 3835-3845

[139]   Venugopal, V., Patterson, C., Shinpaugh, K., Accelerating Particle Image Velocimetry Using Hybrid Architectures, 2009 Symposium on Application Accelerators in High Performance Computing.

[140]   W. Buxton and G.W. Fitzmaurice, "HMD's, Caves, and Chameleon: A Human-Centric Analysis of Interaction in Virtual Space," *Computer Graphics,* vol. 32, no. 4, 1998, pp. 64-68.

[141]   Wee D, Yi T., Anaswamy A., Ghoniem F. (2004) Self-sustained oscillations and vortex shedding in backward-facing step flows: Simulation and linear instability analysis. Physics of Fluids 16 (9), pp. 3361-3373

[142]   Westerweel J., Scarano F. (2005) Universal outlier detection for PIV data. Exp. Fluids 39: 1096-1100

[143]   Westfeld P, Maas HG, Pust O, Kitzhofer J, Brücker C (2010) 3-D Least Squares Matching for Volumetric Velocimetry Data Processing, Proceedings of the 15th International Symposium on Applications of Laser Techniques to Fluid Mechanics, 5-8 July 2010, Lisbon

[144]   Willert C., Stasicki B., Klinner J., Moessner S. (2010) Pulsed operation of high-power light emitting diodes for imaging flow velocimetry. Meas. Sci. Technol. 21: 11pp

[145]   Willert C.E., Gharib M. (1992) Three-dimensional particle imaging with a single camera. Exp. Fluids 12: 353-358

[146]   Williams P.T., Baker A.J. (1997) Numerical simulations of laminar flow over a 3D back-facing step. Int. J. Numer. Methofs Fluid 24, pp. 1159-1183

[147]   Willneff J. (2003) A spatio-temporal matching algorithm for 3D particle tracking velocimetry. ETH Zürich – Dissertation Nr. 15276

[148]   Wolf E., Kähler C.J., Troolin D.R., Kykal C., Lai W (2011) Time-resolved volumetric particle tracking velocimetry of large-scale vortex structures from the reattachment region of a laminar separation bubble to the wake. Exp. In Fluids 50, pp. 977-988

[149]   Wu, J. Z., Gu, J. W. & Wu, J. M. (1987) Steady three-dimensional fluid particle separation from arbitrary smooth surface and formation of free vortex layers. AIAA Paper 87-2348.

[150]   Xu Haitao (2008) Tracking Lagrangian trajectories in position-velocity space. Meas. Sci. Technol. 19: 10pp

[151]   Yamamoto F., Uemura T., Iguchi M., Ohta J., Wada A., Mori K. (1993) §DPTV based on binary image correlations method and ist applications to a mixing flow with a bubbling jet. Computational Methods and Experimental Measurements 6, pp 229-46

[152]   Yuhua Zhu, Tong Zhen, "3D Multi-view Autostereoscopic Display and Its Key Technologie," apcip, vol. 2, pp.31-35, 2009 Asia-Pacific Conference on Information Processing, 2009

[153]   Zhou J., Adrian R.J., Balachandar S., Kendall T.M. (1999) Mechanism for generating coherent packets of hairpin vortices in channel flow. J. Fluid Mech. 387: 353-396